



TECHNISCHE  
UNIVERSITÄT  
WIEN

DISSERTATION

# Simulation of Precipitation in Steel

Ausgeführt zum Zwecke der Erlangung des akademischen Grades eines Doktors  
der technischen Wissenschaften unter der Leitung von

Univ. Prof. Dipl.-Ing. Dr.techn. Ernst Kozeschnik  
E308

Institut für Werkstoffwissenschaft und Werkstofftechnologie

eingereicht an der Technischen Universität Wien  
Fakultät für Maschinenwesen und Betriebswissenschaften

von

Dipl.-Ing. Georg Stechauner

0535207

Polgarstraße 13/C/2

1220 Wien

Wien, am 9.1.2017

Diese Dissertation haben begutachtet:

Prof. Ernst Kozeschnik

Prof. Michel Perez

# Simulation of Precipitation in Steel

Georg Stechauner

Doctoral thesis

Vienna University of Technology,

Faculty for Mechanical and Industrial Engineering

Institute of Materials Science and Technology

January 2017

## Declaration

I declare in lieu of oath, that I wrote this thesis and performed the associated research myself, using only literature cited in this volume.

(Georg Stechauner)

Vienna, January 2017

## **Acknowledgment**

First and foremost, I want to thank my mentor, and friend, Ernst Kozeschnik, for the never ending supply of ideas and the motivation he provided me over the last years. What I have learned from you, goes beyond the academic knowledge, and that's what I am grateful for.

A special thank also goes to Erwin Povoden-Karadeniz, who always had a helping hand. Even though I did not always grasp the full concept of your explanations, especially your excursions into the depths of thermodynamics, your help was always of great importance to me.

The time at university wouldn't have been the same without some colleagues, and friends, like Martin Lückl, Simon Großeiber, Thomas Weisz and Peter Dorfinger. Working and discussing together with them on various topics of their work was helpful in staying on track on my own topic. I have also enjoyed the countless hours that we have spent together on the roads around Vienna.

To all the other colleagues of our work group who are not named here, I will always think back to our fruitful and interesting discussions.

I want to thank Böhler Edelstahl for giving me the opportunity to this project, and especially Ivan Kranjcec-Strahl, for taking care of the whole project administration from the company side.

Lastly, I want to thank the love of my life, Sabrina, and my family, for their trust and their support on all of my ways.

Financial support by the Austrian Federal Government (in particular from Bundesministerium für Verkehr, Innovation und Technologie and Bundesministerium für Wissenschaft, Forschung und Wirtschaft) represented by Österreichische Forschungsförderungsgesellschaft mbH and the Styrian and the Tyrolean Provincial Government, represented by Steirische Wirtschaftsförderungsgesellschaft mbH and Standortagentur Tirol, within the framework of the COMET Funding Programme is gratefully acknowledged.

## Abstract

Consistent and predictive simulations of precipitation and materials properties are a complex task. In this work, the basics behind thermo-kinetic simulations that are based on CALPHAD-type Gibbs energies, a mean-field model for precipitate growth, advanced classical nucleation theory and a predictive model for interface energy calculation are utilized in simulations and discussed in terms of consistency with experimental data. After establishing the theoretical background of these models, this work focuses on the novel approaches that were added to the existing MatCalc framework, in order to simulate the precipitation of Cu in a binary Fe-Cu alloy consistently. These comprise of models for the transition from bcc to 9R to fcc structure, curvature and temperature effects on interfacial energy, particle coalescence as well as a partial thermodynamic reassessment of the Fe-Cu system.

A further impact, when dealing with precipitation kinetics and phase transformations, is the rate at which atoms move through the matrix, hence the rate of atomic diffusion. I analyzed the kinetics of self-diffusion along grain boundaries and dislocations (pipe diffusion) in Al, Fe, and Ni. The suggested values are evaluated between room temperature and melting point, and are aimed at consistency and applicability to the aforementioned thermo-kinetic simulations.

Working with a bottom-to-top mentality, the work moves along from a simple binary system (Fe-Cu) to more complex systems of technical relevance, namely, precipitation hardening steel. By applying the calibrated and published values from the work on binary Fe-Cu to a 15-5 PH steel, Cu-precipitation is modeled consistently to satisfy experimental work of atom probe as well as differential scanning calorimetry. In the end, the results shed new light on the interaction of physical mechanisms and provided new insights into the behavior of phase formation and transformation.

## Kurzfassung

Vorhersagende und widerspruchsfreie Simulationen von Ausscheidungsprozessen und Materialeigenschaften sind eine komplexe Aufgabe der modernen Werkstoffwissenschaft. In dieser Arbeit werden thermo-kinetische Simulationen basierend auf CALPHAD-Gibbs-Energie Datenbanken, einem "Mean-Field" Modell zur Beschreibung des Wachstums, einer Erweiterung der klassischen Nukleationstheorie, sowie einem Modell zur prädiktiven Berechnung der Grenzflächenenergien durchgeführt und mit experimentellen Daten verglichen. Nach einer kurzen Einführung in die theoretischen Grundlagen zu diesen Modellen führt die Arbeit durch die neuartigen Ansätze, welche dem bereits existenten MatCalc Arbeitsprogramm hinzugefügt wurden, um eine widerspruchsfreie Simulation im binären Fe-Cu System zu gewährleisten. Diese neuartigen Modelle umfassen die Transformation der Kristallstruktur von krz über 9R hin zu kfz, die Krümmung und den Temperatureinfluss auf die Grenzflächenenergie, die Partikelkoaleszenz, sowie eine Neubewertung einiger thermodynamischer Grundparameter im Fe-Cu System.

Ein grundlegender Faktor bei der Behandlung von Ausscheidungsvorgängen ist die Mobilität von Atomen in der umgebenden Matrix, kurz, die Diffusion. In dieser Arbeit wurde die Diffusion von Fe, Ni und Al entlang von Pfaden mit hoher Gitterstörung, Korngrenzen und Versetzungslinien, untersucht. Die dabei ermittelten Werte umfassen das gesamte Temperaturspektrum von Raumtemperatur bis hin zur Schmelztemperatur und sind zur Verwendung in thermo-kinetischen Simulationen aufbereitet.

Zur erfolgreichen Durchführung von Simulationen ist es vorteilhaft mit dem simpelsten Arbeitsschritt zu beginnen, und davon ausgehend den Grad der Komplexität zu erhöhen. Diese Mentalität wurde auch in dieser Arbeit umgesetzt. Nachdem das Fe-Cu System verstanden war, sind die daraus entstandenen Erfahrungen im komplexen ausscheidungshärtenden Stahl 15-5 PH angewendet worden. Die Ergebnisse wurden mit Atomsonden und DSC Ergebnissen überprüft. Es wurde nicht nur eine gute Übereinstimmung der Ergebnisse gefunden, sondern auch neue Einblicke in die Prozesse und Mechanismen der Ausscheidungsbildung und Phasenumwandlung gewonnen.

## Preface

This thesis is submitted in compliance with the requirements for the degree of doctor of technical sciences at the Vienna University of Technology. The doctoral work has been carried out at the Faculty of Mechanical and Industrial Engineering, Institute of Materials Science and Technology, Vienna, Austria.

The thesis is divided into two sections. In section A, an introduction to the field of diffusion and thermodynamics is given. Furthermore, the application of both fields to thermo-kinetic simulations and the underlying models are covered.

In section B, the concepts that are discussed in section A are reported in detail in the form of five publications, which are:

1. G. Stechauner, E. Kozeschnik, "Self-Diffusion in Grain Boundaries and Dislocation Pipes in Al, Fe, and Ni and Application to AlN Precipitation in Steel", *J. Mater. Eng. Perform.*, 23 (2014) 1576-1579.
2. G. Stechauner, E. Kozeschnik, "Assessment of substitutional self-diffusion along short-circuit paths in Al, Fe and Ni", *CALPHAD*, 47 (2014) 92-99.
3. G. Stechauner, E. Kozeschnik, "Simulation of Cu precipitation in the Fe-Cu binary system", *Adv. Mater. Res.*, 922 (2014) 728-733.
4. G. Stechauner, E. Kozeschnik, "Thermo-kinetic modeling of Cu precipitation in  $\alpha$ -Fe", *Acta Mater.*, 100 (2015) 135-146.
5. G. Stechauner, S. Primig, E. Kozeschnik, "Early Stages of Cu Precipitation in 15-5 PH Maraging Steel Revisited - Part II: Thermokinetic Simulation", *Steel Res. Int.*, 2016, in print.

Apart from these first author publications, the following papers were published in collaboration with colleagues:

- E. Povoden-Karadeniz, E. Eidenberger, P. Lang, G. Stechauner, H. Leitner, E. Kozeschnik, "Simulation of precipitate evolution in Fe-25Co-15Mo with Si addition based on computational thermodynamics", *J. Alloys Compd.*, 587 (2014) 158-170.
- S. Primig, G. Stechauner, E. Kozeschnik, "Early Stages of Cu Precipitation in 15-5 PH Maraging Steel Revisited – Part I: Experimental Analysis", *Steel Res. Int.*, 2016, in print.

Moreover, the work that was performed throughout the years has been presented at numerous international and national conferences:

- G. Stechauner, "Simulation of precipitates in complex steels", *oral presentation at 7<sup>th</sup> European Doctorate Meeting*, Trnava, Slovakia, 14.-16.11.2012.
- G. Stechauner, E. Kozeschnik, "Grain boundary and dislocation pipe diffusion in Al, Fe and Ni", *oral presentation at EUROMAT2013*, Sevilla, Spain, 8.-13.9.2013.
- G. Stechauner, E. Kozeschnik, "Simulation of Cu precipitation in the Fe-Cu binary system", *poster session presented at THERMEC2013*, Las Vegas, USA, 2.-6.12.2013.
- G. Stechauner, "Simulation of Cu precipitation in Fe-Cu binary system", *oral presentation at 8<sup>th</sup> European Doctorate Meeting*, Budapest, Hungary, 13.-14.1.2014
- G. Stechauner, E. Kozeschnik, "Simulation of precipitation kinetics and strengthening in high-alloyed steel", *oral presentation at MSE2014*, Darmstadt, Germany, 22.-26.9.2014.
- G. Stechauner, F. Mendez-Martin, S. Schwarz, E. Kozeschnik, "Tailoring copper precipitates in a 17-4 PH steel by using thermo-kinetic simulation software", *oral presentation at 61. Metallkunde Kolloquium*, Lech am Arlberg, Austria, 15.-17.4.2015.
- G. Stechauner, S. Schwarz, E. Kozeschnik, "Investigation of a possible mechanism for the formation of reverted austenite in 13-8 PH steel", *oral presentation at EUROMAT2015*, Warsaw, Poland, 21.-24.9.2015.
- G. Stechauner, "Strengthening in steel: from binary Fe-Cu to complex compositions", *oral presentation at 1<sup>st</sup> Strengthening Kolloquium*, Thallern, Austria, 5.-6.10.2015.

*"Am Ende wird alles gut.  
Und wenn es nicht gut ist, ist es noch nicht das Ende."*

- Oscar Wilde

# Content

## Section A

1. Introduction.....	1
2. "The Big Picture".....	3
3. Theoretical Background.....	6
3.1 Diffusion in Solids.....	6
3.2 Precipitation in Solid-State.....	10
3.3 The CALPHAD Approach.....	13
4. Applied Simulation Models.....	15
4.1 Calculation of Interfacial Energy.....	15
4.1.1 Size dependence.....	18
4.1.2 Temperature dependence.....	19
4.2 Analysis of Precipitate Growth.....	20
4.3 Evaluation of the Minimum Nucleation Energy.....	23
4.4 Transformation Sequence.....	25
4.5 Coalescence and Cluster Mobility.....	27
5. Simulation of 15-5 PH steel: A case study.....	29
6. Summary and Outlook.....	32
7. References.....	33

## Section B

Paper I	p. 38	G. Stechauner, E. Kozeschnik, "Self-Diffusion in Grain Boundaries and Dislocation Pipes in Al, Fe, and Ni and Application to AlN Precipitation in Steel", <i>J. Mater. Eng. Perform.</i> , 23 (2014) 1576-1579.
Paper II	p. 48	G. Stechauner, E. Kozeschnik, "Assessment of substitutional self-diffusion along short-circuit paths in Al, Fe and Ni", <i>CALPHAD</i> , 47 (2014) 92-99.
Paper III	p. 67	G. Stechauner, E. Kozeschnik, "Simulation of Cu precipitation in the Fe-Cu binary system", <i>Adv. Mater. Res.</i> , 922 (2014) 728-733.
Paper IV	p. 78	G. Stechauner, E. Kozeschnik, "Thermo-kinetic modeling of Cu precipitation in $\alpha$ -Fe", <i>Acta Mater.</i> , 100 (2015) 135-146.
Paper V	p. 110	G. Stechauner, S. Primig, E. Kozeschnik, "Early Stages of Cu Precipitation in 15-5 PH Maraging Steel Revisited - Part II: Thermokinetic Simulation", <i>Steel Res. Int.</i> , 2016, in print.

# Section A

## Introduction and Background

### 1. Introduction

Modern day material development and science is a lively field with ever changing tasks and challenges. It is practically impossible to develop novel methods and clarify longstanding problems by a simple “trial-and-error” approach. Over the last decades, the importance of simulations in the field of material science is of ever increasing significance. It is the three-link chain model that connects processing - structure/properties - performance, which is a central paradigm of modern materials science and engineering. When focusing on the central part, structure and properties, by simulative means, a key tool enabling through-process modeling is obtained. This work centers especially on the development of new models and the application to the existing framework of simulation of precipitation processes.

Precipitation hardening was first reported in 1911 by Alfred Wilm in aluminium alloys [1]. It still represents one of the most effective means of strengthening of materials. The basic principles of this hardening mechanism is the hindering of dislocation movement as a result of the interaction with particles. The amount of strengthening is predominantly a function of radius and inter-particle-spacing [2]. Consequently, understanding the mechanisms of nucleation and growth is key to the development of new materials and the improvement of existing ones. Since the degree of complexity scales, among other things, with the amount of alloying elements, the binary Fe-Cu system was selected in this work as a perfect candidate for detailed precipitation kinetics analysis.

Over the last decades, this system has proven itself to be the hobbyhorse of numerous researchers, and the published works on experimental analyses deliver satisfying results for most observable quantities. However, the thermodynamic simulation of this system, especially kinetic parameters, such as phase fraction and radius evolution, leaves some question marks behind. Whereas Monte-Carlo approaches [3-5] succeed in describing the early stages of nucleation, they are inherently limited by the size of the simulation cell and, therefore, of limited suitability to a description of the

continuous growth and coarsening of precipitates in the meso- and macroscale. Existing continuum-mechanic calculations [6-8] often rely on the use of "unphysical" parameters, such as fitted interfacial energies or diffusion rates deviating from the experimentally assessed ones by some orders of magnitude. Coarsening experiments and calculations [9] succeed in describing the late stages of the precipitate evolution, however, are inherently different when linked directly to the nucleation event. By the time this thesis started, no single work covering the whole precipitation process in a fully consistent manner had been available.

In the present work, a state parameter-based continuum-mechanical Ansatz is selected to simulate the precipitation kinetics of Cu precipitates in binary Fe-Cu. By implementing novel concepts into the existing framework of the thermo-kinetic toolbox MatCalc, satisfying results for both isothermal, as well as continuous heating conditions could be obtained. A major part of the software MatCalc is based on CALPHAD-type Gibbs energies, a mean-field model for precipitation, advanced classical nucleation theory and a predictive model for interface energy calculation. Among the refined models, which clearly go beyond the conventional and established approaches, is an improved calculation of the interfacial energy taking into account entropic effects [10], the consideration of size dependent transformations [11], and the implementation of a cluster coalescence mechanism [12].

In the following section, some basics about diffusion in solids, thermodynamics and precipitation will be outlined. A brief overview concerning predictive simulations and the interface energy calculation will be given. The summary and outlook will conclude the first part of this thesis.

---

## 2. "The Big Picture"

After establishing the cornerstones of this work in the introduction, a big question is left unanswered: "What is this work good for? What is it aimed at? Who is benefiting from it?". Considering the years, I have spent working on this topic, I feel that the reader is eligible to receiving some answers, which I will break down into three separate parts:

- Why simulations?
- Why Fe-Cu?
- Where does it connect to industrial needs?

To start off, I want to define a simulation as "an imitation of an operation or a real-life process/system within pre-set boundaries and conditions". This definition is intentionally vague, to exemplify how far the boundaries for simulations are spread: from riding a mechanical bull, to resuscitating CPR-Annie, to performing thermo-kinetic simulations predicting microstructure and materials properties; all are simulations. And all share the common denominator of *giving insights into mechanisms* and providing a sandbox to modify and adapt parameters to ultimately improve real-life processes.

Exactly this point, providing insights to otherwise not accessible states, is it what makes the simulation so valuable in the work of describing the Fe-Cu system. It was a well-known fact in the early 70s that peak hardening condition of a precipitation hardening Fe-Cu alloy is reached after some hours of annealing around 500 °C [13] and scientists assumed that the cause lies in a coherent precipitate structure with a few atomic diameters in dimension. It was the advanced work of Goodman et al. [13], using the upcoming technique of field ion microscopy, that delivered the experimental proof for the existence of these precipitates. From there on, dozens of papers have been published concerning studies at all different size ranges of Cu-precipitates from a few or less than nanometers during nucleation and first growth [14] up to coarsening experiments involving micrometer sized particles [15].

The picture evolving from experimental work was continuously supported by simulations, also performed in more or less discrete size ranges and often with distinct goals in mind. Monte-Carlo (MC) simulations contributed greatly to the understanding of the early stages, from the formation of the nucleus containing a handful of atoms up to precipitates with sizes of a few nanometers [3-5]. Simulations on the lower end of the nano-scale are typically carried out with a study of the energies of the nuclei and early stages of precipitation, where ab-initio methods can successfully applied [16-18].

The results offer good understanding to nucleation processes, but are not feasible to describe the evolution at a large time-scale.

When exceeding the length and time scales typically studied in ab-initio and MC simulations, later stage precipitation is often studied on the meso- and macro-scale, where the Fe-Cu problem was formulated within kinetic frameworks several times [19-22]. On closer inspection of the corresponding results, one observes that the conventional models can give a general fit to the evolution of some precipitation parameters, however, by either sacrificing accuracy or running into the necessity of having to apply unphysical "fitting" parameters. In the course of the present work, it became clear from the evaluation of the existing data that no such model was presently able to describe the precipitation kinetics in Fe-Cu consistently over the total time and size scale, enveloping the beginnings of nucleation, the growth through various coherency states, and ultimately coarsening.

And this leads to the third point of the present "Big Picture": the connection from the simulation back to the real world, to the needs of industry. By providing insights into the evolution of the material microstructures, a cost efficient, targeted and quick way of materials development becomes possible. I want to conduct a small mind experiment, to emphasize the difference between a calibrated simulation, and the conservative trial-and-error method: picture a high alloy steel, with several tens of wt.-% alloying elements in addition to the base element, iron (Figure 1). In the beginning, one thinks of varying just a single one of these, and to stay consistent with this work, let it be Cu. After a short time, one recognizes that, in order to obtain reasonable mechanical properties, one also has to vary the annealing temperature, which is typically in the range of 350 to 650 °C. An additional degree of freedom comes from the annealing time, which can range from several minutes, to several hours, or even several days. To keep the analysis simple, one always uses the same starting condition after solution treatment and quenching, and keep all other process parameters constant.



Figure 1 - Thought experiment of a trial and error approach to materials development.

Counting everything assumed so far together leads to some hundred states. To obtain statistical confidence against outliers, every condition should be certified with several samples, leading to an even greater amount of experiments. By now adding one more degree of freedom, such as, for

instance, a second annealing step, deformation or varying more than just one element the experimental matrix is bloated to a point from where it cannot be processed straightforwardly, and techniques, such as "design of experiments" must be utilized to be able to carry the experimental load.

Now I want to compare the experimental approach to a simulation. Once, a feasible, predictive and efficient simulation method has been developed, one can easily write a script, which accounts for the various Cu contents, the temperatures, the heating rates, and one can further add processing steps, such as, deformation or multiple heat treatments. Using a sly approach of simulation, where one recycles parts that repeat themselves, and only calculates the actually modified segments, a full simulation run can be completed in a matter of minutes. Hundreds of states could be handled in a matter of days; thousands in a few weeks.

This is the benefit for the user.

Welcome to the world of numerical simulations.

### 3. Theoretical Background

According to Merriam-Webster dictionary, the word "precipitation" describes "the process of separating a solid substance from a liquid" [23]. In everyday life, the term "precipitation" is well-known from meteorologists, describing phenomena such as rain, hail, or the formation of snow. Naturally, the first scientific investigations of precipitation reactions were describing the formation of liquid droplets of vapor, as performed by Thomson [24] and Gibbs [25]. However, it was some forty years later that Wilm discovered a similar process in solid-state in metals [1].

Two conditions must be fulfilled for precipitation to occur: motivation to form a new phase, and the mobility of elements participating in this reaction. The mobility describes the ability of atoms and particles to move within their surroundings, and is generally known as diffusion as described in section 3.1. The motivation for phase separation, on the other hand, portrays the energy landscape within a system and its evolution and will be handled in section 3.2. Only if both of these criteria are met, precipitation can occur. In the following sections, the thermodynamic background for solid-state precipitation, together with the basic models, are briefly reviewed. How these can be used to calculate and predict actual phase transformations will be touched in section 3.3.

#### *3.1 Diffusion in Solids*

It is a well-known experiment from school, that ink, dropped into water, does not stay in its droplet form, but rather disperses until it is homogeneously distributed in the liquid after sufficient time. Amazingly, this process also occurs in solids, driven by solid-state diffusion. It is diffusion that describes the movement of atoms through the lattice, and it is key for internal processes such as microstructure and property changes, solidification and segregation phenomena, or the examined solid-state precipitation phenomenon.

The mathematical, experimental and theoretical background to diffusion itself is extensive and details can be found, for example, in the book of H. Mehrer [26]. This section gives a brief overview, only, and discusses the effect of certain defects, namely grain boundaries and dislocation pipes, on the diffusion kinetics.

In conventional steel microstructures, there exist always some gradients of concentrations of atoms due to segregation, phase transformations or precipitation events. Typically, atoms diffuse from highly concentrated regions into the direction of regions of low concentration, trying to equilibrate the system. The rate of atoms being transferred during diffusion is known as the flux,  $J$ , and is defined as

mass per unit area per time. The relation of flux and concentration gradient,  $c$ , in its most simple and one dimensional case, is given by the equation known as Fick's First Law [27]

$$J = D \frac{\partial c}{\partial x}, \quad (\text{Eq. 1})$$

where  $D$  is the diffusion coefficient, given in units of area per time. The actual movement of an atom through the lattice can be described as a series of finite, random jumps to neighboring sites. To mathematically describe these jumps as a function of time, we can derive Fick's second law (Eq. 2) from Equation 1 as

$$\frac{\partial c}{\partial t} = D \frac{\partial^2 c}{\partial x^2}. \quad (\text{Eq. 2})$$

A displacement of atoms in a crystalline material occurs predominantly by random jumps into empty adjacent lattice positions (in the case of substitutional atoms) or inside the interstitial sublattice (for interstitial atoms). Between these sites, an energy barrier exists, as a consequence of the periodic potential of the crystal lattice, which has to be overcome by the migrating atom. This so called *activation energy for diffusion*  $Q$  is a handy quantity, as it can be used in a temperature dependent formula, to directly calculate diffusion rates. With the pre-exponential factor  $D_0$  and the activation energy  $Q$ , the diffusion coefficient can be calculated with

$$D = D_0 \exp\left(-\frac{Q}{RT}\right), \quad (\text{Eq. 3})$$

where  $R$  is the universal gas constant and  $T$  is the temperature. In this approach, not only self-diffusion of atoms of the same species (e.g. Fe atoms in Fe matrix) can be described, but also all other diffusive events, as long as a corresponding activation energy is known. Luckily, researches throughout the last century put an immeasurable effort into the experimental determination of these values, and extensive tables can be found in literature like Mehrer [26] or the Landolt-Börnstein database [28].

The formulation of Fick given above is based on experimental results of diffusion of salt ions in aqueous solution. Strictly speaking, Fick's first law (Eq. 1) is a special case, where the salt ions do not interact chemically and the diffusion process is governed solely by the random walk of atoms. Thus, in a generalized approach, considering the force acting on an atom is more suitable, and much more realistic. In diffusion, this force is given by the negative gradient of the chemical potential,  $\mu$ . The chemical potential can be linked to the flux,  $J$ , with

$$J = -cB\nabla\mu, \quad (\text{Eq. 4})$$

where  $c$  is the concentration of atoms and  $B$  is the diffusional mobility and Eq. (4) giving a most general relation between thermodynamic forces and the diffusional flux. Using thermo-kinetic simulation software MatCalc, the chemical potential is a calculated quantity, and readily accessible for this task.

This treatment of diffusion, so far, has only considered a single diffusion species, while systems of technical interest typically contain numerous elements. In such a multi-component system, the specific flux,  $J_i$ , of an element  $i$ , can be calculated by using the corresponding values for  $c_i$ ,  $B_i$  and  $\mu_i$ . As the chemical potential is a function of the elemental composition, all multi-component effects potentially arising from solution non-ideality, are already accounted for. Only by using a multi-component approach, where the impact of every single element on every other element is considered, effects, such as uphill diffusion of an element against its composition gradient, can be explained.

Diffusion along "defects", such as grain-boundaries or dislocation pipes, can lead to a substantial increase in the diffusion kinetics [29]. Dislocations are one-dimensional lattice defects of either excess half-lattice planes in the crystal (edge dislocations) or by one atomic distance displaced atoms (screw dislocations), surrounded by tensile and compressive stress fields (see Figure 2 - left). Whereas the dislocation pipe thus represents a "line" of defects through the crystal, a grain boundary is a two-dimensional imperfection and, in that way, of much larger extension. Within a grain, a common crystallographic orientation can be seen. At the boundary of two or more grains, these orientations experience an abrupt and discontinuous change and the interface region can become highly incoherent (Figure 2 - right). Metaphorically speaking, these defects offer more room for migrating atoms, compared to the otherwise densely packed matrix.

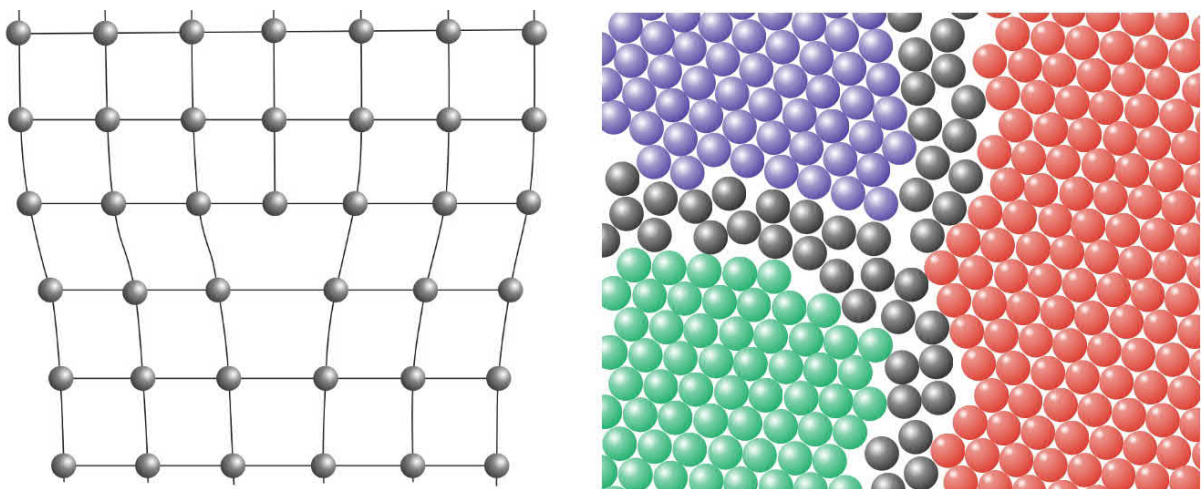


Figure 2 - Schematic reproductions of (left) an edge dislocation and (right) grain boundaries.

Inside a dislocation pipe or grain boundary, the energy barrier for an exchange of lattice position can be considerably decreased. Figure 3 shows the assessed self-diffusion coefficient of body centered Fe for diffusion in bulk and along dislocation pipes and grain boundaries. As a result of accounting for the ferromagnetism below the Curie temperature, a bulge is experienced.

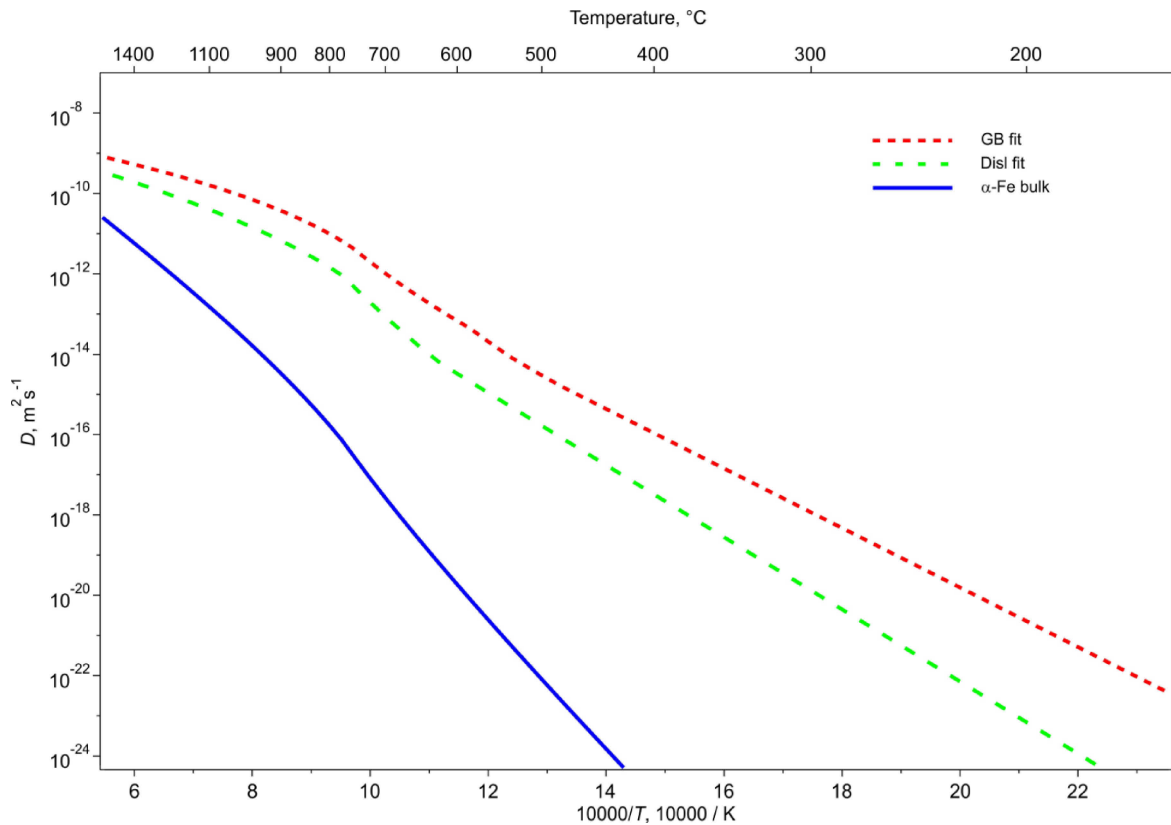


Figure 3 - Self-diffusion in bcc-Fe in (blue) bulk and along (red) grain boundaries and (green) dislocation pipes [29]. The bulge around 800°C represents the change from ferro- to paramagnetic state around the Curie temperature.

The values for bulk diffusion, as shown in Figure 3 and Table 1, are based on the work of Campbell and Rukhin (Ni and Al) [30], Jönsson ( $\alpha$ -Fe) [31], and Fridberg et al. ( $\gamma$ -Fe) [32]; the assessed activation energies and pre-exponential factors for short-circuit diffusion paths are taken from own work [29].

Table 1 - Assessed activation energies and pre-exponential factors for self-diffusion in Fe, Al, and Ni

		$Q$	$D_0$			$Q$	$D_0$	
		[kJ/mol]	[m <sup>2</sup> /s]			[kJ/mol]	[m <sup>2</sup> /s]	
bcc Fe	low $T$ RT - 693K	Bulk	285	$6.0 \cdot 10^{-4}$	Aluminium	Bulk	$127.2$	$1.4 \cdot 10^{-5}$
		GB	135	$2.1 \cdot 10^{-6}$		GB	60.2	$2.0 \cdot 10^{-5}$
		Disl	155	$1.8 \cdot 10^{-6}$		Disl	83.2	$1.5 \cdot 10^{-6}$
	medium $T$ 693 - 1214K	Bulk	330	1.5	Nickel	Bulk	287	$2.3 \cdot 10^{-4}$
		GB	180	$5.3 \cdot 10^{-3}$		GB	122	$1.2 \cdot 10^{-5}$
		Disl	200	$4.5 \cdot 10^{-3}$		Disl	171	$4.0 \cdot 10^{-5}$
	high $T$ $1214 - T_m$	Bulk	240	$2.0 \cdot 10^{-4}$	fcc Fe	Bulk	286	$7.0 \cdot 10^{-5}$
		GB	90	$7.0 \cdot 10^{-7}$		GB	145	$5.5 \cdot 10^{-5}$
		Disl	110	$6.0 \cdot 10^{-7}$		Disl	185	$4.5 \cdot 10^{-5}$

The lattice self-diffusion in defect-poor metals is understood and assessed [30-32] and generally follows the Arrhenius law with the key variables activation energy  $Q$  and pre-exponential factor  $D_0$ . Although the acceleration along short-circuit paths, such as, grain boundaries or dislocation pipes, is certainly more complex and depends greatly on purity, temperature range, used experimental method, type of dislocation and grain boundary, etc., the mean values presented here, as well as the analysis in ref. [29], represent "ready-to-use" values for diffusion enhancement at lattice heterogeneities from room temperature to the melting point, based on a best-practice fit to the available experimental information and averaging specific details of the defects.

### 3.2 Precipitation in Solid-State

In order to quantify the rate at which precipitation phenomena occur, an expression for the nucleation rate, will be derived next. The nucleation rate tells us how many nuclei of a certain phase are formed per unit volume and unit time. To arrive at the nucleation rate, the motivation for phase separation that is a prerequisite for precipitation to occur, is analyzed in a first place. In this context, the motivation for phase separation can be understood as a process that minimizes the Gibbs energy,  $G$ , (Eq. 5), of the precipitation system. The Gibbs energy is a convenient quantity to describe the energy of a thermodynamic system at constant pressure [33] based on enthalpy  $H$ , temperature  $T$  and entropy  $S$

$$G = H - TS . \quad \text{Eq. 5}$$

The derivatives of the Gibbs energy with respect to the state parameters pressure, temperature and number of moles of components deliver important quantities, such as, volume, entropy, or the chemical potential. Knowing the Gibbs energy and its derivatives enables us, therefore, to describe phase stabilities based on energy, or energy dissipation, minimization at a given set of state parameters. In a simple manner, the method to identify the energetically most favorable state, can be depicted by drawing the common tangent (Figure 4) to the individual energy curves in the so-called Gibbs energy / mole fraction (G-X) diagram. By this method, the phase fields, equilibrium compositions, and, by using the lever law, even the equilibrium phase fractions of each phase can be obtained in a graphical way.

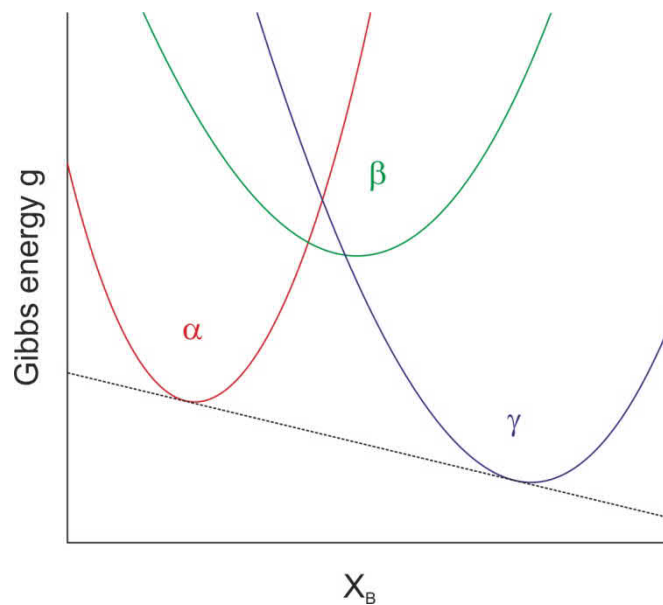


Figure 4 - Gibbs energy curves in a binary A-B alloy. In the present example, the parallel tangent construction delivers a stability region for the  $\alpha$  and  $\gamma$  phases, but no region of  $\beta$  phase stability.

To arrive at an equation for the nucleation rate, the treatments of Volmer and Weber [34] and Becker and Döring [35] are introduced, first. Their methodology is based on the works of Thomson [24] and Gibbs [25], considering a critical droplet which is in equilibrium with its surroundings. When this condition is met, the volumetric work for condensation and evaporation are exactly balanced by the energy required for interface formation, which is given by

$$4fr^2\uparrow = W^* + \frac{4fr^3}{3} \cdot \frac{2\uparrow}{r}, \quad \text{Eq. 6}$$

where  $r$  is the radius of liquid droplet,  $\uparrow$  is the surface tension and  $W^*$  is the work required to form a critical nucleus, which can be rewritten as

$$W^* = \frac{1}{3} \dagger A, \quad \text{Eq. 7}$$

with  $4\pi r^2$  as the surface area  $A$ . This treatment can be translated likewise into solid-state matter, by considering chemical potentials, instead of mechanical work, and one would arrive at a comparable result, where energy from creating new surface area and expressed in terms of the specific free energy,  $\Delta G_{\text{surf}}$ , is balanced by the change of bulk energy expressed in terms of specific volume free energy,  $\Delta G_{\text{vol}}$ . Plotting these two quantities, scaled with respect to the surface area and volume, delivers the well-known Figure 5, which shows the graphical interpretation of the nucleation energy,  $\Delta G_{\text{nucl}}$ .

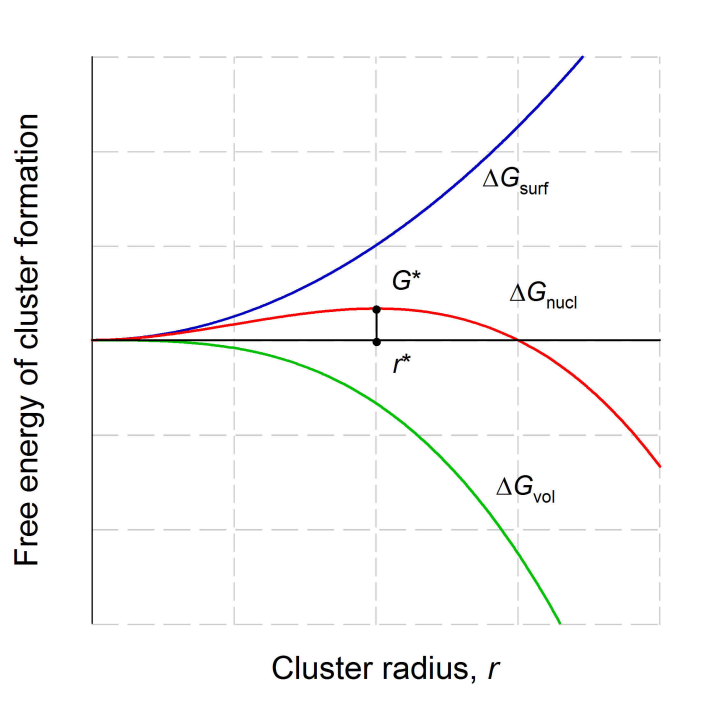


Figure 5 - Free energy of cluster formation as a function of cluster radius.

The exact value for the critical nucleation energy,  $G^*$ , can now be evaluated straightforwardly, by setting the derivative of  $\Delta G_{\text{nucl}}$  equal to zero. This analysis delivers

$$G^* = \frac{16f}{3} \frac{(\Delta G_{\text{surf}})^3}{(\Delta G_{\text{vol}})^2}. \quad \text{Eq. 8}$$

In this equation,  $\Delta G_{\text{surf}}$  represents the effect of the interface energy, while  $\Delta G_{\text{vol}}$  considers the driving force as well as elastic effects, which will be covered in more detail in section 4.  $G^*$  represents a key quantity for steady-state nucleation, which will be covered next.

From the obtained critical nucleation energy, one can directly express the probability  $P$  of a single nucleation event using Boltzmann statistics in the form of

$$P = \exp\left(\frac{-G^*}{k_B T}\right). \quad \text{Eq. 9}$$

While Equation 9 gives the probability for a single nucleation event, one important proportionality factor in the final equation for the nucleation rate is the number of lattice sites,  $N$ , where nucleation events can potentially occur. Based on the type of nucleation site, values between approximately  $10^{29} \text{ m}^{-3}$  for homogeneous nucleation in undisturbed crystal volume,  $10^{24} \text{ m}^{-3}$  for dislocations in deformed fcc, down to values as low as  $10^{13} \text{ m}^{-3}$  for grain boundary corners in  $100 \text{ }\mu\text{m}$  sized grains, can be obtained [33].

Finally, only two further ingredients are missing to the nucleation rate, which are the proportionality factors  $Z$ , Zeldovich factor, and  $S^*$ , the atomic attachment rate. The Zeldovich factor accounts for the reverse transformation probability of critical clusters due to thermal activation. The atomic attachment rate is a kinetic factor based on the individual diffusion rates and concentration differences between precipitate and matrix.

The steady state nucleation rate,  $J_s$ , can finally be written as

$$J_s = NZS^* \exp\left(-\frac{G^*}{k_B T}\right), \quad \text{Eq. 10}$$

where all variables and quantities, except one, are known from the thermodynamic properties of the system. The last missing ingredient is the interfacial energy, which is kind of elusive to experimental measurements and is often used as a fitting factor, to obtain satisfying simulation results. In section 4, I will outline the approach to the calculation of the interfacial energy based upon the generalized broken bond model as introduced by Sonderegger and Kozeschnik [36].

### ***3.3 The CALPHAD Approach***

In the late 60s and early 70s, researchers started to develop methods to evaluate and describe phase diagrams of multi-component thermodynamic systems based on comprehensive Gibbs energy descriptions. The most important technique developed there is the CALPHAD - "CALculation of PHase Diagrams" method [37], and it provides the basis to practically all advanced computational thermodynamics and kinetics software available today.

In the previous section, we have introduced the Gibbs energy in form of G-X curves. While these are helpful to describe and understand the basic phenomena in simplified binary alloys, a "real" thermodynamic system is usually characterized by complex chemical interactions, which cannot be described by an ideal or a regular solution. To successfully work in a multicomponent multiphase

---

environment, the CALPHAD approach provides the general approach to representing the Gibbs energy,  $g$ , as [33]

$$g = g_{\text{IS}} + g_{\text{EX}}, \quad \text{Eq. 11}$$

where  $g_{\text{IS}}$  is the molar Gibbs energy of an ideal solution, and  $g_{\text{EX}}$  represents all excess terms and interactions. The excess terms account for effects coming from non-ideal chemical interactions, contributions from magnetism, and the contribution from short-range chemical ordering effects.

All the required information mentioned above can be conveniently stored in thermodynamic databases, as functions of temperature, pressure and composition. The data is acquired from experimental thermochemical data, like calorimetric tests (enthalpies of formation, heat capacities) and equilibrium phase diagram data [38]. It is the strength of CALPHAD that the properties of a multicomponent phase, i.e. its molar enthalpy, entropy, heat capacity and Gibbs energy, are founded on the thermodynamics of its forming simple compounds. Typically, optimizations are made in low-order binary and ternary systems, where experimental data is often available. On this fundament, reasonable assumptions about the thermodynamics of high-order systems are made.

## 4. Applied Simulation Models

This chapter gives a more detailed view on the newly developed and implemented models that have been used within the MatCalc simulation framework [39] in order to face the challenges treated in the present work. The investigated and supplied experimental material in this project is a precipitation hardening steel, which obtains its strength on the basis of finely dispersed Cu particles. In this chapter, the binary Fe-Cu system will be used illustratively to represent the occurring processes. An application of these models to the technical material and some results of the simulation will be given in the following section.

### 4.1 Calculation of Interfacial Energy

When two, initially separated phases, are brought into contact, the atoms along the fresh interface interact, and the energy related to this phenomenon is called the *interface energy*. The concept of this roots back to Thomson [24] and Gibbs [25] who investigated the formation of liquid droplets from vapor, as we have already discussed in section 3.2. As we have seen, the interface energy is a key quantity in numerous materials related simulations. Unfortunately, the interface energy cannot be directly "measured" from key experiments. Consequently, in this section, we will review a method of calculating the interface energy on a theoretical basis, by using the "Nearest-Neighbor Broken-Bond model" (NNBB), and its advanced version, the "Generalized Broken-Bond model" (GBB).

To understand the principles behind the broken-bond models, a thought experiment, as introduced by R. Becker [40] in 1938, provides a simple approach to the concept and calculation of interfacial energies. Consider two blocks of homogenous phases,  $\alpha_1$  and  $\alpha_2$ . From counting all the atomic bonds within the blocks, we can determine their total energy. Now, assume that the blocks are cut in half, and attached again to the respective other one (Figure 6).

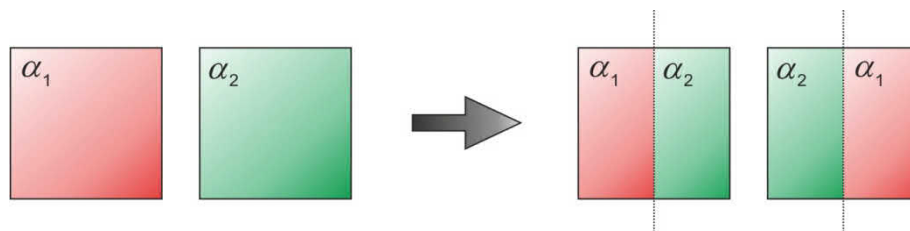


Figure 6 - Scheme for calculation of interface energy as proposed by Becker [40] with the dashed lines being the newly created interface.

The interfacial energy  $\chi$  of the newly created interface can be expressed by Equation 12 with

$$\chi = E_{12}^{\text{new}} - E_1^{\text{broken}} - E_2^{\text{broken}}, \quad \text{Eq. 12}$$

with  $E_{12}^{\text{new}}$  being the energy of the newly created bonds across the interface between the unlike blocks, and  $E_1^{\text{broken}}$  and  $E_2^{\text{broken}}$  representing the energy of the broken bonds of the initial configuration. In order to evaluate the energies as presented in Eq. 12, one needs to know values for the strength of the interatomic bonds. These values are not readily available, and require modern computational science methods, such as Density Functional Theory or Molecular Dynamics. An important contribution to solve this problem, and dodge the requirement of knowing the interatomic bond energies was made by D. Turnbull [41].

The Ansatz used by Turnbull considers two blocks of purely A and B atoms, respectively. Using the formalism that can be found for regular solutions [33], the interatomic energies can be reduced to an effective interaction potential. Since this quantity is part of both, the enthalpy of solution equation, as well as the interface energy equation, these can be combined to

$$\chi = \frac{n_s z_s}{N_A z_L} \cdot \Delta H_{\text{sol}}, \quad \text{Eq. 13}$$

where  $n_s z_s / N_A z_L$  is a structural factor consisting of  $n_s$ , the number of atoms per unit area of interface,  $z_s$ , the number of broken bonds across the interface counted per interface atom,  $N_A$  the Avogadro number,  $z_L$ , the coordination number, and  $\Delta H_{\text{sol}}$  being the enthalpy of solution. Using Equation 13, the interface energy can be calculated straightforwardly, as long as the thermodynamics of a system is known.

The approach of Becker [40] and Turnbull [41], as described here, has shown some promising results in the fcc crystallographic systems, but application to other systems, for example bcc, remained critical due to the simplification of using only the nearest-neighbor. It was the work of Sonderegger and Kozeschnik [36] that provided a generalization of this problem, extending the interaction to  $n$ -nearest neighbors. Thus, their approach is subsequently denoted as the Generalized Broken-Bond model (GBB).

The main idea behind their work was to replace the quantities  $z_s$  and  $z_L$ , only considering nearest-neighbor broken-bonds, by effective quantities  $z_{s,\text{eff}}$  and  $z_{L,\text{eff}}$ , which also take interactions into account with atoms of higher-order coordination spheres. Figure 7 shows a schematic of the broken-bonds across a randomly oriented interface.

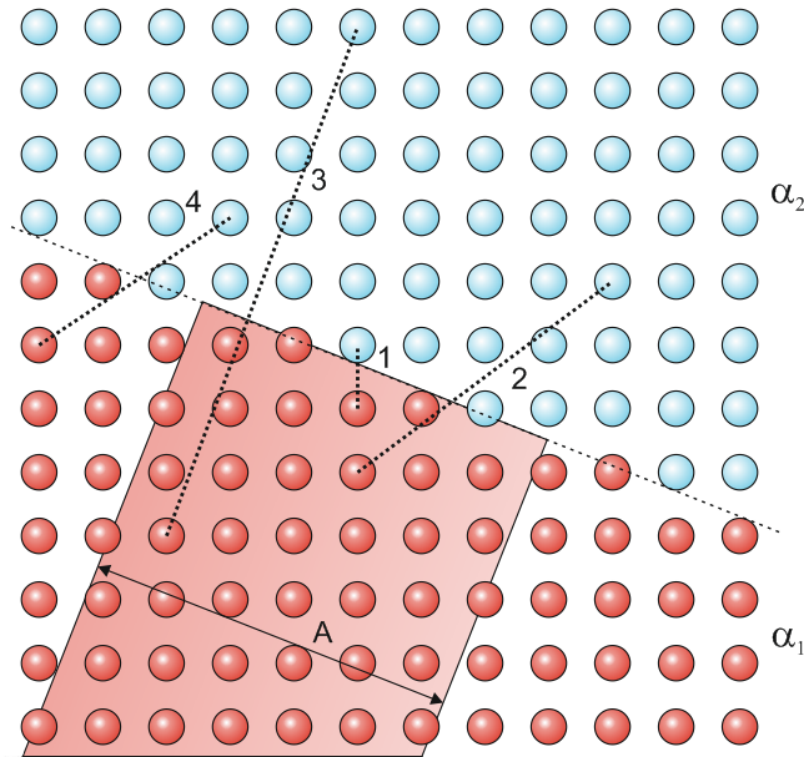


Figure 7 - Schematic representation of the broken-bonds counted in the GBB model. Only broken bonds across the interface are considered. While (1) represents the classical case of a first-nearest-neighbor broken-bond, (2) and (3) represent higher-order broken-bonds. Bond (4) is not considered as it is outside of the reference area.

The analysis of the effective number of broken-bonds is performed in three steps:

1. Define the orientation and crystal structure of the interface.
2. Count the effective number of broken bonds across the interface area  $A$  and take a weighting factor into account considering  $k$ -order coordination bonds.
3. Refer the number of broken-bonds to the mean interface area of a single atom.

The analysis itself is carried out with periodic translational elements and is based on numeric integration. The summation of the bond energies up to a  $k$ -th shell are considered, and the accuracy increases with increasing consideration of coordination shells. The evaluated, effective coordination numbers for  $z_{L,eff,bcc}$  and  $z_{L,eff,fcc}$  are 12.234 and 14.442, compared to the traditional, first-nearest-neighbor values for  $z_{L,bcc}$  and  $z_{L,fcc}$  of 8 and 12, respectively. The mean structural factor  $z_{S,eff}/z_{L,eff}$  giving the ratio of effective broken bonds per atom, is approximately equal for bcc and fcc with roughly 0.33 [36].

The interfacial energy obtained by this method is evaluated under the assumption of a sharp, planar interface, taking only bonds into account, that are broken across the interface. As this ideal

interface is infinitely thin, there is no mixing across the interface taken into account, and the calculated value is an upper limit to the interfacial energy. In reality, entropic contributions come from a diffuse interface because of mixing across the interface, which decreases the effective interfacial energy. This, and the reduction of interface energy because of interface curvature for small particles, will be covered in the next sections.

#### 4.1.1 Size dependence

As explained earlier, a prerequisite of the original GBB model to the calculation of interfacial energy is the planar interface. This state, however, is not present when dealing with the early stages of precipitation, as a fresh nucleus or particle consists naturally only of a couple of atoms, up to probably a few hundred and, thus, has a finite size. The consideration of the size dependence in the GBB model was described by Sonderegger and Kozeschnik [42].

In their approach, they modified the bond-counting procedure, compared to the planar case, by not only considering the atoms within a reference area, but by consideration of all atoms within the precipitate. This quantity is then normalized with respect to all bonds within the precipitate and the number of atoms.

Using the adapted methodology, the authors [42] succeed in counting the number of broken bonds and derive a correction function in terms of the nearest-neighbor distance,  $r_1$ , and the precipitate radius,  $r$ , with

$$\Gamma(r) = 1 - \frac{6}{11} \frac{r_1}{r} + 0.08921 \frac{r_1^2}{r^2} + 0.045 \cdot \ln\left(\frac{10}{3} \frac{r}{r_1}\right) \frac{r_1^2}{r^2}. \quad \text{Eq. 14}$$

A comparison of the size dependent approach compared to the planar case delivers values between  $\Gamma(r) = 0.6$  to  $0.9$  for typical nuclei sizes that are in the order of 1 to 5 times  $r_1$  and it is shown in Figure 8.

The interfacial energy, considering the size dependence of  $\chi(r)$ , is finally given by

$$\chi(r) = \chi_{\text{GBB}} * \Gamma(r) \quad \text{Eq. 15}$$

with  $\chi_{\text{GBB}}$  being the calculated, planar interfacial energy.

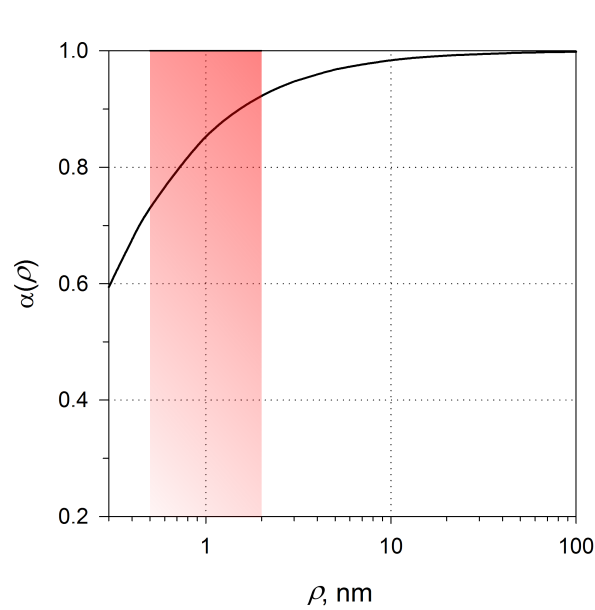


Figure 8 - Size-dependent correction factor to evaluate the interface energy of finite sized precipitates.

#### 4.1.2 Temperature dependence

The second requirement for application of the GBB model that was stated previously, is a sharp interface, as shown in Figure 7. A sharp interface is infinitely thin, with all atoms belonging uniquely to either one phase on the two sides. This condition, however, is highly idealistic, and can thermodynamically only be stable at 0 K. At temperatures above zero, atoms will mix with a certain nonzero probability. Interfaces showing a certain degree of mixing are denoted as diffuse interfaces, and have a decreased total interfacial energy. The mathematical method behind this calculation was developed by Sonderegger and Kozeschnik in ref. [43] and a schematic representation is given by the inserts in Figure 9.

The temperature dependence for the diffuse interface is given by the critical temperature  $T_c$  of the corresponding phase, which is related to the interaction energy of the atoms within the phase. In the case of Fe-Cu, we can evaluate [22]  $T_c$  by following the phase boundary of the miscibility gap and then read the highest temperature. At this temperature, the phase decomposes, thus the interface is infinitely large, which is the opposite of being sharp. Following the curve in Figure 9, one sees that at low temperatures the model of Sonderegger and Kozeschnik [43] predicts a sharp interface. The interface energy reduction  $S(T/T_c)$  is substantial. For Fe-Cu, at typical annealing temperatures for precipitation of 400 to 700 °C, the reduction is in the order of 80 to 50% (Figure 9).

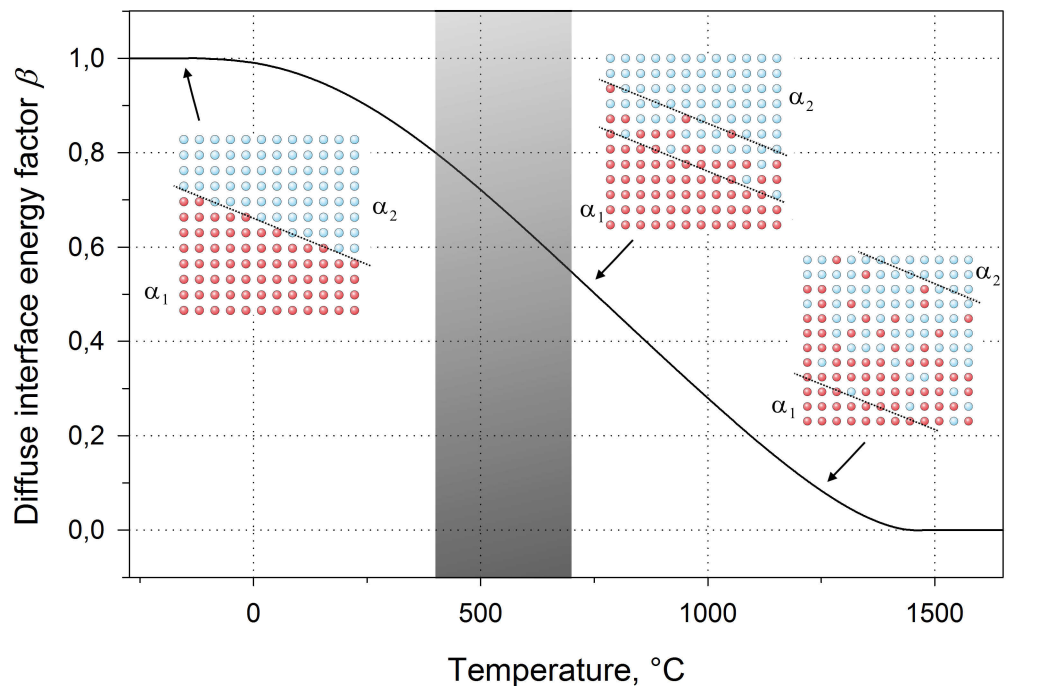


Figure 9 - The diffuse interface energy factor for the regular solution critical temperature of 1750 K as evaluated in the Fe-Cu system. Typical annealing temperature is highlighted by the gray area. Inserts show different states of a sharp interface, being ideally, completely sharp on the very left, to a rather diffuse interface on the right end.

The calculation of temperature dependent interfacial energy  $\chi(T)$  is again multiplicative with

$$\chi(T) = \chi_{\text{GBB}} * S(T/T_c). \quad \text{Eq. 16}$$

## 4.2 Analysis of Precipitate Growth

The first stage of a phase transformation is the generation of supercritical nuclei and has been covered in chapter 3. The nucleation process is a stochastic process, which can be described quantitatively only on a statistical basis. In contrast to this stochastic event, the successive stage of precipitate growth is a deterministic one. The laws that control the growth and shrinking processes of the new phase can be described by appropriate evolution equations. As the actual answer to this task is quite lengthy, as a full review on moving phase boundaries should be given, and intensive in mathematics, this section should only cover the basics behind precipitate growth as it is implemented in MatCalc. A full review of this topic can be found in ref. [33].

The situation that is present after nucleation of a supercritical particle in a supersaturated matrix is depicted in Figure 10. The sketch shows the composition profile surrounding the precipitate and its forming elements, together with the diffusive fluxes. The gradients  $J$  in Figure 10 are given by

Fick's first law (see section 3.1). Apparently, and as shown by the different sizes of the arrows, the diffusive fluxes do not necessarily need to balance.

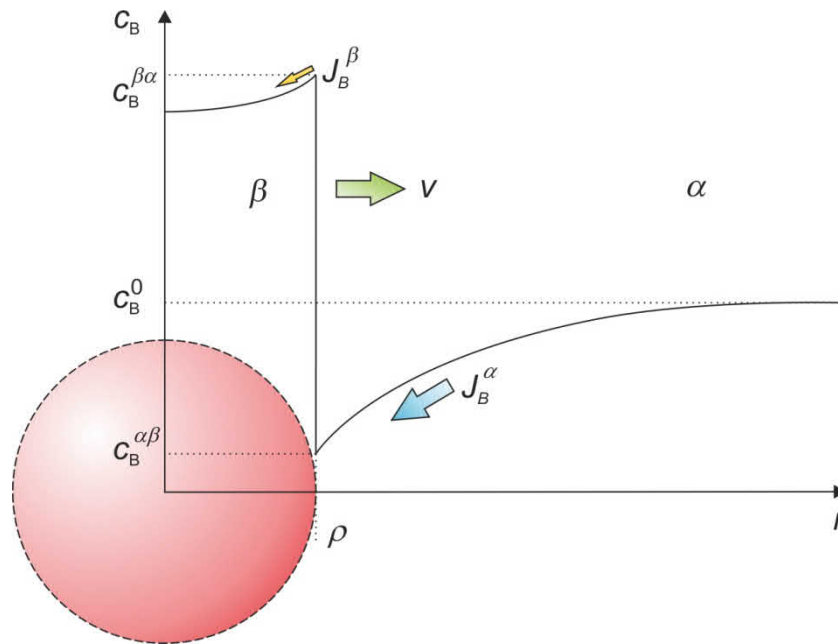


Figure 10 - Schematic representation of a B-rich precipitate growing in a supersaturated matrix.

If, as shown here, the flux toward the interface is dominant, mass balance requires that this imbalance is compensated by a movement of the phase boundary with a velocity  $v$ . The mass balance equation for the diffusion-controlled migration of the phase boundary can be written as

$$J_i^{rs} + J_i^{sr} = [[c_i^{rs}]] \cdot v, \quad \text{Eq. 17}$$

where  $[[c_i^{rs}]]$  is the difference in the concentrations on the precipitate and matrix interface, respectively. This fundamental equation describes the diffusional growth generally, for any species  $i$ . Solving this problem, diffusional transport of either mass or energy, for the unknown velocity and interface compositions, is known as the "Stefan problem", with the difficulty that additional assumptions have been introduced in the solution procedure, since more unknowns are present in this formulation compared to the number of equations. Out of the numerous strategies to reduce the degrees of freedom and solve this problem, the one developed by Svoboda et al. [44], using the "Thermodynamic Extremal Principle" (TEP), will be shown in the following.

The TEP was originally stated by L. Onsager [45] and reformulated in ref. [33] as:

*A closed solid-state thermodynamics system at constant temperature and pressure, which is out of equilibrium, evolves along the particular kinetic pathway with maximum entropy production.*

This statement is valid if the temporal change in Gibbs energy,  $\dot{G}$ , of a solid-state thermodynamic system, equals minus one half of the energy dissipation rate,  $Q$ . For a constant temperature, the maximum entropy production is equivalent to the maximum energy dissipation, and the authors present the relation between Gibbs energy,  $G$ , and the energy dissipation rate,  $Q$ , in terms of independent state parameters,  $q_i$ , and generalized velocities,  $\dot{q}_i$  as

$$\frac{\partial G}{\partial q_i} = -\frac{1}{2} \frac{\partial Q}{\partial \dot{q}_i}. \quad \text{Eq. 18}$$

In a next step, a formulation for both terms,  $G$  and  $Q$ , is required and can be found in the work of Svoboda, Fischer, Fratzl and Kozeschnik [44], and is thus further denoted as the SFFK model.

The SFFK model offers mean-field evolution equations for substitutional and interstitial phases. In the "mean-field" approach, an arrangement of homogeneous spherical precipitates is embedded in a homogeneous multicomponent matrix. The total Gibbs energy of this system can be given as the sum of the following contributions:

1. the *Gibbs energy of the matrix*: The sum of the number of moles of components in the matrix is multiplied by the corresponding chemical potentials performed over all elements in the system.
2. the *Gibbs energy of the precipitates* offers two contributions, both multiplied by the volume of the precipitates: first, the elastic stress field caused by the volume misfit; second, the specific chemical energy given by the concentration and chemical potentials in the precipitates.
3. the *total interface energy*: Over all precipitates, the sum of the interface energy is weighted by the surface area.

Once the Gibbs energy of the system is defined, the next step for the application of the TEP (Eq. 18) is to define possible mechanisms by which the excess Gibbs energy can be dissipated in the course of the system evolution. The three processes as defined by Svoboda et al. [44] are:

1. *interface migration*: The movement of the precipitate-matrix interface is accompanied by a local rearrangement of atoms. This proceeds against a retarding force, which can be compared to mechanical friction, thus it dissipates energy.

2. *diffusion inside the precipitate*: The evolution of chemical composition within the precipitate is accompanied by diffusive fluxes that dissipate energy by the production of entropy.
3. *diffusion outside the precipitate*: The growth of the precipitate or the evolution in composition is accompanied by long-range transport of atoms toward (or away) from the precipitate. The diffusive processes occur in the embedding matrix and dissipate energy by the production of configurational entropy.

Inserting the individual contributions into the TEP equation (Eq. 18) delivers a linear system of equations for the kinetic parameters. The time integration of these kinetic parameters can then be performed with standard techniques as described in ref. [46].

### ***4.3 Evaluation of the Minimum Nucleation Energy***

In section 3.2, the Gibbs energy for nucleation was given to determine the nucleation energy (Eq. 8) and the nucleation probability (Eq. 9), respectively. An important quantity in this equation is the driving force, which can, in principle, be read straightforwardly from G-x diagrams (Figure 11) after application of the parallel tangent construction.

In a supersaturated compound of A and B atoms, where the B atoms are in solid solution with the A matrix atoms, Figure 11 shows the free energy curves to the corresponding  $\Gamma$  and S phases and the given matrix composition in point A. The driving force  $d_{\text{chem}}$  for precipitation of S phase can be obtained by drawing a tangent to the  $\Gamma$ -phase in point A and shifting a parallel to S-phase. This construction delivers the so called ortho-equilibrium nucleus composition and access to the chemical composition of precipitate phase S, as well as the molar driving force. Both quantities are required for a calculation of nucleation energy.

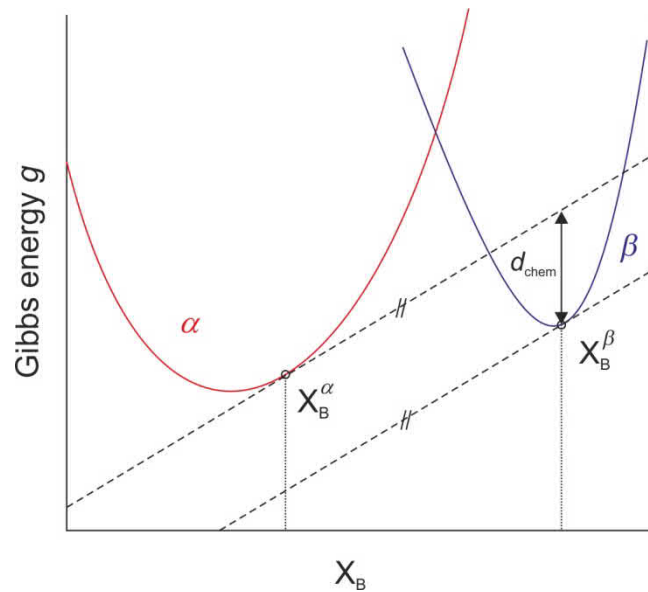


Figure 11 - G-X diagram allowing for an evaluation of driving forces in a supersaturated solid solution.

However, this approach to the nucleation energy  $G^*$  is a simplification, as the interfacial energy itself, as well as the chemical driving force, are dependent on the composition of the S phase. This was first discussed by Hobstetter [47] and later by Kozeschnik [48]. The authors propose an alternative model using on the concept of a minimum nucleation barrier,  $G^*$ , based on the composition-dependence of interfacial energy and driving force. Calculating the critical nucleation energy and the nucleation probability, respectively, from this approach in the Fe-Cu system delivers a Cu-rich nucleus instead of an almost pure Cu particle (Figure 12).

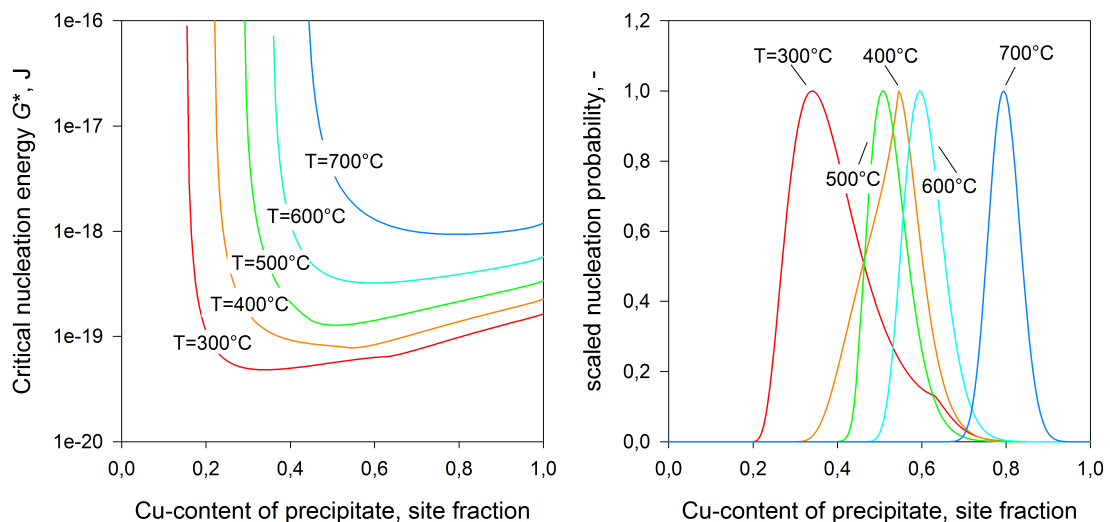


Figure 12 - (a) Critical nucleation energy  $G^*$  and the (b) normalized nucleation probability in an Fe-3wt.-%Cu system [49].

Figure 12 shows that the critical nucleation barrier for a particle incorporating Fe is below the barrier of the Cu-rich particle with highest driving force and, thus, the most likely nucleus as a

function of chemical composition and temperature is not the one corresponding to the equilibrium composition with minimum Fe, but rather the one with substantial Fe incorporation. Moreover, while, at low temperatures, the nucleus is rather rich in Fe, it will change with an increase in temperature towards an almost pure Cu composition, as predicted by the ortho-nucleus concept. The predicted nucleus composition delivering the highest nucleation rates thus becomes a strong function of temperature, which is not predicted from the ortho-equilibrium concept. The benefit of this method is that it is based purely on thermodynamics and no kinetic assumptions are necessary.

#### ***4.4 Transformation Sequence***

The crystal structure of the early coherent Cu precipitates is constrained by the surrounding  $\gamma$ -Fe matrix in which they are embedded. During growth, the precipitates pass through one, or two, metastable states, being 9R and 3R structure [14], until ultimately, the stable fcc structure is obtained [15]. The first transformation, from bcc to 9R occurs as the interfacial strain increases with growing particle size. Once a critical radius is reached, a martensitic transformation is triggered, and by twinning, a 9R structure forms, that is also known as the "Herring Bone" structure [14]. This semi-coherent structure offers better stress accommodation across the interface compared to the coherent bcc structure.

At even larger radii, the final transformation towards the equilibrium fcc structure occurs. This point is reached, when the volumetric misfit becomes the dominant term in the particle free energy. In this work, we assume that the transformation radii for bcc/9R transformation is around 2-3 nm, and the 9R/fcc transformation occurs at 6-10 nm. These values are chosen in accordance to experimental information provided in refs. [14,15]. Figure 13 shows 9R and fcc precipitates, reproduced from the works of Othen et al. [14] and Speich and Oriani [15], respectively.

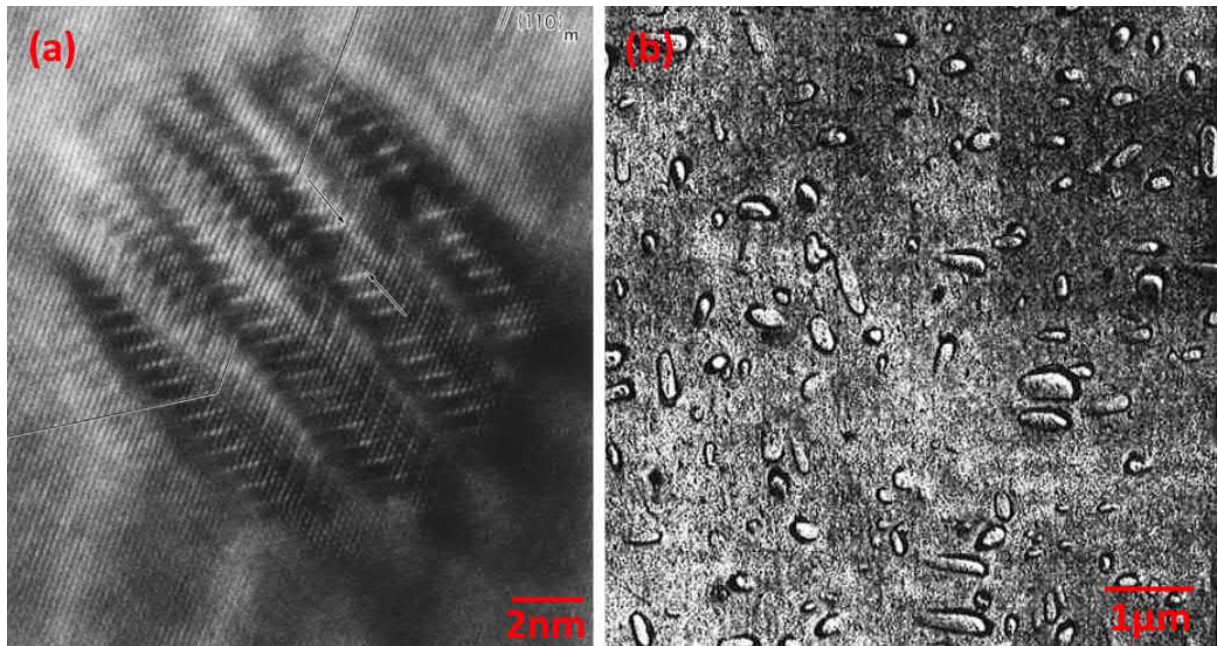


Figure 13 - (a) 9R Cu precipitate in Fe-1.3wt.-%Cu alloy after 100 h annealing at 550 °C, reproduced from ref. [14], reprinted with permission of Taylor & Francis (b) fcc Cu precipitate in Fe-5.4wt.-%Cu alloy after 4 h annealing at 830 °C, reproduced from ref. [15], reprinted with permission of The Minerals, Metals & Materials Society.

The actual implementation of the transformation between the different structures is realized in such a way that the number density of parent phase precipitates is gradually decreased in favor of the product phase. This process is starting at the lower radius transformation threshold,  $r_{t,min}$ , and finishes at the higher radius transformation threshold,  $r_{t,max}$ . Between the thresholds, a linear mixing (transformation) rule is applied (Figure 14).

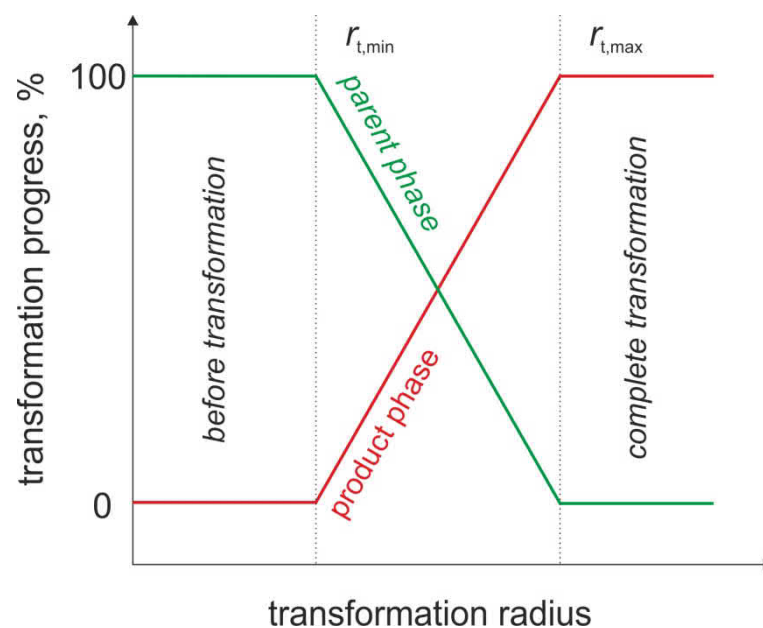


Figure 14 - Schematic reproduction of the radius dependent transformation model applied in this work.

As we consider an in-situ transformation from one crystal structure to the other, we assume that the chemical composition remains unchanged in the transformation process.

#### ***4.5 Coalescence and Cluster Mobility***

In the Fe-Cu system, as well as several others, the attractive and repulsive interactions between vacancies (Va) and the other alloying elements are of immediate relevance for the kinetic processes. Soisson and Fu [50] investigated these vacancy-solute interactions, and analyzed the nature of Fe-Va interactions to be repulsive, while Cu-Va are attractive. Barashev and Arokiam [51] deduce that strong binding energies up to the second nearest neighbor lead to stable Cu-Va dipoles, which do not easily dissolve during diffusion.

The mobility of Cu clusters in an Fe matrix was investigated by several authors [7,50,52], and it was found that the diffusion rates are accelerated by several orders of magnitude compared to the monomer diffusion rates. Warczok et al. [12] performed rigid lattice Metropolis Monte Carlo simulations in the Fe-Cu system, with a single vacancy driving the evolution within the system. Their simulations showed that a vacancy preferably populates the matrix/precipitate interface, thus leading to a substantial increase in the mobility of the interface. Jourdan et al. [5,53] evaluated this acceleration to be of two orders of magnitude compared to monomers. The authors agree that the high mobility of clusters leads to a Brownian motion-like migration through the matrix that finally results in cluster collision and particle coalescence and ultimately leads to coarsening. Figure 15 shows the coarsening characteristics obtained in the simulations of Warczok et al. [12] at various times. In the beginning, the Cu clusters and atoms are distributed randomly in the simulation box. With ongoing simulation time, a strong coalescence occurs, until ultimately only a few precipitates, much larger in size, are left.

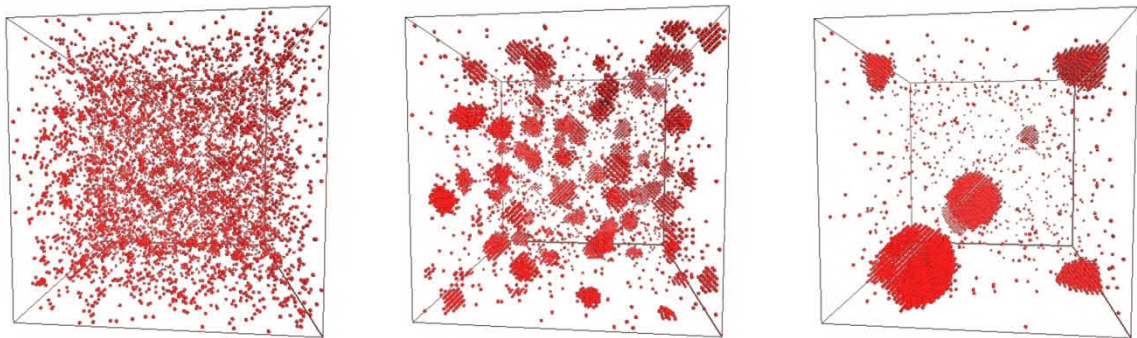


Figure 15 - Monte Carlo calculations of the clustering and coalescence in Fe-3at.-%Cu. Cu is shown in red, matrix Fe is not shown for clarity.

The Ansatz that Warczok et al. [12] developed in their work is based on the work on vapor droplet coalescence by Binder and Stauffer [54,55]. Accordingly, each cluster has a certain size-dependent diffusion rate,  $D_i$ , with

$$D_i = D_m \cdot l^n, \quad (\text{Eq. 19})$$

where  $l$  represents the cluster size,  $D_m$  the diffusion rate of the monomer, and  $n$  the Binder-Stauffer coefficient. As a consequence of the continuous collisions of clusters, it is assumed that the total number density of precipitates,  $N$ , decreases proportionally to the cross-sectional area of the precipitates, which is given by the mean radius  $\bar{r}^2$ . The rate of the number density change as a consequence of coalescence, can be expressed as

$$\dot{N}_i^c = kN\bar{r}^2 D_i, \quad (\text{Eq. 20}),$$

with  $k$  representing a calibration factor for the strength of coalescence. A direct consequence of coalescence is the earlier onset of growth during kinetic simulations and the disappearance of the typical steady-state plateau before onset of coarsening, which is commonly observed in mean-field models for the precipitate size evolution.

## 5. Simulation of 15-5 PH steel: A case study

In this final chapter, I want to briefly showcase the work on precipitation hardening steel, performed in cooperation with S. Primig et al., since it represents an outstanding example for the use of thermo-kinetic simulations in materials science. This case study consolidates all the methods and principles that are outlined in the previous sections and is aimed at illustrating the performed work. A thorough analysis of this topic can be found in the respective papers [49,56].

S. Primig et al. performed differential scanning calorimetry (DSC) experiments on a 15-5 PH steel (Table 2) and observed two exothermic reactions at around 300 and 500 °C. The established theory in literature attributes the former of the two reactions to nucleation of Cu precipitates, and the latter one to the growth of these very particles. These peaks were further investigated by atom probe tomography (APT). From these experiments, only a weak clustering was detected around 300 °C, and no clear and distinct interpretation could be derived purely from the experimental results, since the expected and modeled clusters sizes are too close to the detection limit of the APT device. For the second reaction, the APT measurements detected enrichment in the center of the precipitates by Cu. In this context, the thermo-kinetic simulations offer important additional information.

Table 2 - Chemical composition of 15-5 PH maraging steel in weight percent.

<b>15-5 PH</b>	<b>C</b>	<b>Si</b>	<b>Mn</b>	<b>Cr</b>	<b>Ni</b>	<b>Cu</b>	<b>Nb</b>	<b>Fe</b>
wt.-%	0.04	0.3	0.6	14.9	5.1	3.3	0.3	bal.

I applied the calibration of the binary Fe-Cu system without further manipulations of the parameters to the complex composition of the supplied technical alloy. By using the same heating ramp as in the DSC experiment, a simulation setup close to reality was established. Figure 16 is showing the so-called thermo-kinetic triplet, which is always a key result in materials simulation, as the three quantities, phase fraction, number density and radius, offer a comprehensive overview to the precipitate evolution within the material. Together with the chemical composition of the matrix, the results support the hypothesis of Primig et al. [56]. A quantitative reproduction of the heat flow (Figure 17) allows to further identify the mechanisms behind the exothermic reactions.

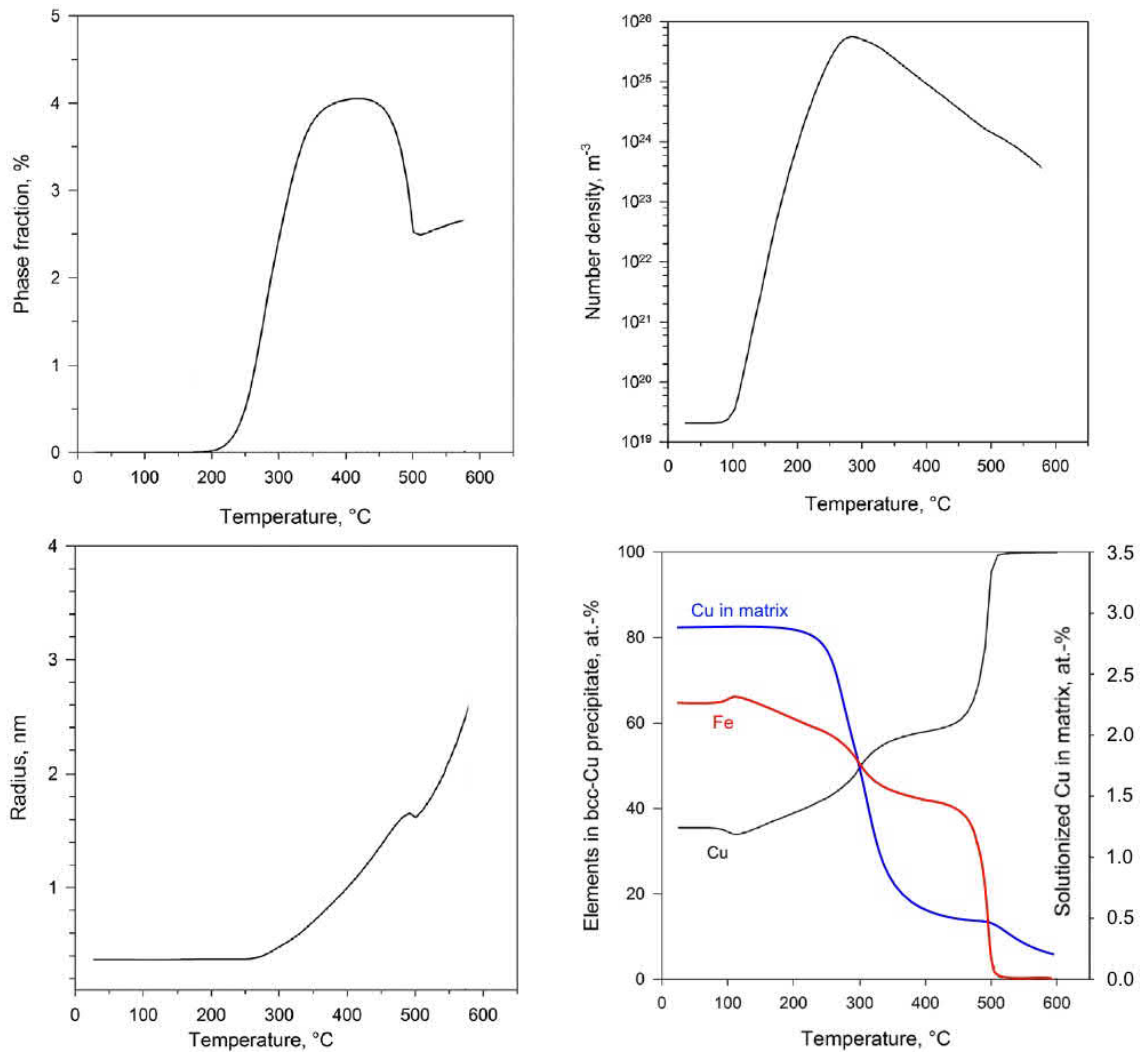


Figure 16 - Simulation results of 15-5PH steel, showing the thermo-kinetic triplet, phase fraction, number density and radius, together with evolution of chemical composition for precipitate and matrix.

In the range of the first peak, nucleation and growth of Fe-rich Cu clusters occurs. This is accompanied by a decrease of the amount of free Cu atoms within the matrix and is the source to the heat flow signal of the first exothermic reaction. At the time where the second reaction occurs, the matrix is almost depleted of Cu atoms, thus, further nucleation or growth by the attachment of new Cu atoms to existing precipitates cannot be the source of the signal. In accordance with the APT results, the simulation predicts a transition around 500 °C from the initially Fe-rich particle to an almost pure Cu precipitate. In this course, the enthalpy of the Cu-precipitate changes drastically, resulting in the significant heat flow signal.

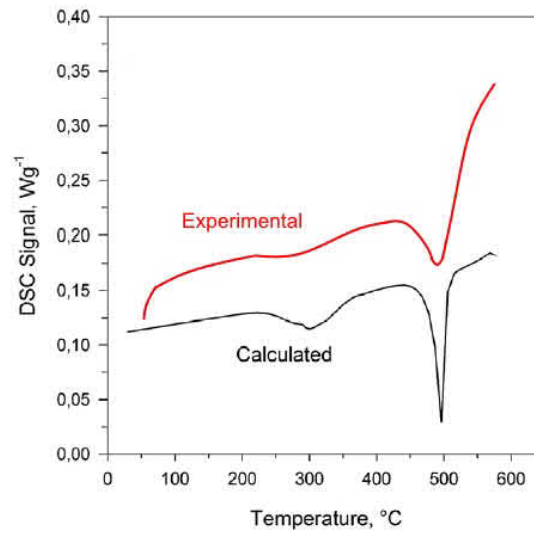


Figure 17 - Calculated and experimental DSC curves in 15-5PH steel.

This published work represents a formidable example of modern materials science, where results are obtained experimentally and further substantiation is provided in a simulation.

## 6. Summary and Outlook

With the methodologies and models developed in this work, the first consistent and comprehensive simulation of precipitation in the binary Fe-Cu system, which successfully reproduces experimental data, has been developed. Starting from the existing MatCalc simulation framework that is based on CALPHAD-type Gibbs energies, a mean-field model for precipitate growth, advanced classical nucleation theory and a predictive model for interface energy calculations, I applied and implemented novel methods, such as the radius dependent transformation, the temperature-dependence of interfaces, or application of cluster coalescence.

Within the present approach, I successfully reproduced the evolution of the kinetic triplet, representing phase fraction, radius, and number density, over a large temperature range from 450 to 700 °C. As MatCalc has knowledge of the total system Gibbs energy, and constantly monitors all processes, such as nucleation, growth, coarsening, dissolution and transformations, the information can be used to even calculate thermo-chemical properties and reproduce Differential Scanning Calorimetry experiments.

In order to reproduce precipitation kinetics in technical alloys, the knowledge about grain boundary and dislocation pipe diffusion enhancement is fundamental. This work offers easy-to-use equations based on the well assessed bulk diffusion rates. It was shown that the effect of so-called short-circuit diffusion paths is decisive in the precipitation simulation.

The present work gives insights into the processes of precipitation kinetics, which are fundamental to modern steel development. Some of the models, such as the temperature dependent interface energy, were already successfully implemented into other systems. The present findings can be further applied to the development of new alloys and materials systems.

## 7. References

1. A. Wilm, "Physikalisch-metallurgische Untersuchungen über magnesiumhaltige Aluminiumlegierungen", *Metallurgie: Zeitschrift für die gesamte Hüttenkunde*, 8 (1911) 225-227.
2. M.R. Ahmadi, E. Povoden-Karadeniz, K.I. Öksüz, A. Falahati, E. Kozeschnik, "A model for precipitation strengthening in multi-particle systems", *Comp. Mater. Sci.*, 91 (2014) 173-186.
3. N. Castin, M.I. Pascuet, L. Malerba, "Modeling the first stages of Cu precipitation in alpha-Fe using a hybrid atomistic kinetic Monte Carlo approach", *J. Chem. Phys.*, 135 (2011) 1-9.
4. D. Molnar, R. Mukherjee, A. Choudhury, A. Mora, P. Binkele, M. Selzer, B. Nestler, S. Schmauder, "Multiscale Simulations on the coarsening of Cu-rich precipitates in alpha-Fe using kinetic Monte Carlo, molecular dynamics and phase-field modeling", *Acta Mater.*, 60 (2012) 6961-6971.
5. T. Jourdan, J.-L. Bocquet, F. Soisson, "Modeling homogeneous precipitation with an event-based Monte Carlo method: application to the case of Fe-Cu", *Acta Mater.*, 58 (2010) 3295-3302.
6. A.V. Barashev, S.I. Golubov, D.J. Bacon, P.E.J. Flewitt, T.A. Lewis, "Copper precipitation in Fe-Cu alloys under electron and neutron irradiation", *Acta Mater.*, 52 (2004) 877-886.
7. F. Christien, A. Barbu, "Modelling of copper precipitation in iron during thermal aging and irradiation", *J. Nucl. Mater.*, 324 (2004) 90-96.
8. I. Holzer, E. Kozeschnik, "Computer simulation of the yield strength evolution in Cu-precipitation strengthened ferritic steel", *Mater. Sci. Eng. A*, 527 (2010) 3546-3551.
9. R. Monzen, K. Takada, K. Matsuda, "Coarsening kinetics of Cu particles in an Fe-1.5% Cu alloy", *Z. Metallkd.*, 94 (2003) 1241-1246.
10. B. Sonderegger, E. Kozeschnik, "Interfacial energy of diffuse phase boundaries in the generalized broken-bond approach", *Metall. Mater. Trans. A*, 41 (2010) 3262-3269.
11. B. Sonderegger, E. Kozeschnik, "Size dependence of the interfacial energy in the generalized nearest-neighbor broken-bond approach", *Scripta Mater.*, 60 (2009) 635-638.
12. P. Warczok, J. Zenisek, E. Kozeschnik, "Atomistic and continuums modeling of cluster migration and coagulation in precipitation reactions", *Comput. Mater. Sci.*, 60 (2012) 59-65.
13. S.R. Goodman, S.S. Brenner, J.R. Low Jr., "An FIM-atom probe study of the precipitation of copper from iron-1.4 at. pct copper. part I: field-ion microscopy", *Metall. Trans.*, 4 (1973) 2363-2369.

14. P.J. Othen, M.L. Jenkins, G.D.W. Smith, "High-resolution electron microscopy studies of the structure of Cu precipitates in alpha-Fe", *Philos. Mag. Lett.*, 70 (1994) 1–24.
15. G.R. Speich, R.A. Oriani, "The rate of coarsening of copper precipitate in an alpha-iron matrix", *Trans. Metall. Soc. AIME*, 233 (1965) 623–631.
16. A. Seko, S.R. Nishitani, I. Tanaka, H. Adachi, E.F. Fujita, "First-principle calculation on free energy of precipitate nucleation", *CALPHAD*, 28 (2004) 173-176.
17. K. Yuge, A. Seko, I. Tanaka, S.R. Nishitani, "First-principles study of the effect of lattice vibrations on Cu nucleation free energy in Fe-Cu alloys", *Phys. Rev. B*, 72 (2005) 1-7.
18. D. Reith, M. Stoehr, R. Podloucky, T.C. Kerscher, S. Muller, "First-principles modeling of temperature- and concentration-dependent solubility in the phase-separating alloy  $\text{Fe}_{x}\text{Cu}_{1-x}$ ", *Phys. Rev. B*, 86 (2012) 020201.
19. M. Perez, M. Dumont, D. Acevedo-Reyes, "Implementation of classical nucleation and growth theories for precipitation", *Acta Mater.*, 56 (2008) 2119–2132.
20. I. Holzer, E. Kozeschnik, "Computer simulation of the yield strength evolution in Cu-precipitation strengthened ferritic steel", *Mater. Sci. Eng. A*, 527 (2010) 3546–3551.
21. J.B. Yang, M. Enomoto, C. Zhang, "Modeling Cu precipitation in tempered martensitic steels", *Mater. Sci. Eng. A*, 422 (2006) 232–240.
22. G. Stechauner, E. Kozeschnik, "Thermo-kinetic modeling of Cu precipitation in  $\alpha$ -Fe", *Acta Mater.*, 100 (2015) 135-146.
23. "precipitation." *Merriam-Webster.com*,  
<http://www.merriam-webster.com/dictionary/precipitation>, 20.6.2016.
24. W. Thomson, "On the Equilibrium of Vapour at a Curved Surface of Liquid", *P. Roy. Soc. Edinb.*, 7 (1870) 63-68.
25. J.W. Gibbs, "The Scientific Papers", New York: Dover Publications Inc., 1961.
26. H. Mehrer, "Diffusion in Solids", Berlin-Heidelberg: Springer-Verlag, 2007.
27. A. Fick, "Ueber diffusion", *Annalen der Physik*, 170 (1855) 59-86.
28. I. Kaur, W. Gust, "Grain and interphase boundary diffusion", in: H.Mehrer, (Ed.). Springer Materials - The Landolt-Börnstein Database, 2012. (Chapter12).
29. G. Stechauner, E. Kozeschnik, "Assessment of substitutional self-diffusion along short-circuit paths in Al, Fe, and Ni", *CALPHAD*, 47 (2014) 92-99.

- 
30. C.E. Campbell, A.L. Rukhin, "Evaluation of self-diffusion data using weighted means statistics", *Acta Mater.*, 59 (2011) 5194–5201.
  31. B. Jönsson, "On ferromagnetic ordering and lattice diffusion - a simple model", *Z. Metallkd.*, 83 (1992) 349-355.
  32. J. Fridberg, L.-E. Törndahl, M. Hillert, "Diffusion in iron", *Jernkont. Ann.*, 153 (1969) 263-276.
  33. E. Kozeschnik, "Modeling Solid-State Precipitation", New York: Momentum Press, LLC, 2013.
  34. M. Volmer, A. Weber, "Keimbildung in übersättigten Gebilden", *Z. Phys. Chem.*, 119 (1926) 277-301.
  35. R. Becker, W. Döring, "Kinetische Behandlung der Keimbildung in übersättigten Dämpfen", *Ann. Phys.*, 24 (1935) 719-752.
  36. B. Sonderegger, E. Kozeschnik, "Generalized Nearest Neighbor Broken Bond Analysis of Randomly Oriented Coherent Interfaces in Multi-Component fcc and bcc Structures", *Metall. Mater. Trans. A.*, 40 (2009) 499-510.
  37. H. L. Lukas, S. G. Fries, B. Sundman, "Computational thermodynamics: the Calphad method", Vol. 131, Cambridge University Press, 2007.
  38. N. Saunders, A.P. Miodownik, "Calphad calculation of phase diagrams", Pergamon Materials Series, Vol. 1, Elsevier Science Ltd.
  39. <http://matcalc.at/>
  40. R. Becker, "Die Keimbildung bei der Ausscheidung in Metallischen Mischkristallen", *Ann. Phys.*, 32 (1938) 128-140.
  41. D. Turnbull, "Impurities and Imperfections", *American Society of Metals*, (1955) 121-144.
  42. B. Sonderegger, E. Kozeschnik, "Size Dependence of the Interfacial Energy in the Generalized Nearest-Neighbor Broken-Bond Approach", *Scripta Mater.*, 60 (2009) 635-638.
  43. B. Sonderegger, E. Kozeschnik, "Interfacial Energy of Diffuse Phase Boundaries in the Generalized Broken-Bond Approach", *Metall. Mater. Trans. A*, 41 (2010) 3262-3269.
  44. J. Svoboda, F.D. Fischer, P. Fratzl, E. Kozeschnik, "Modelling of Kinetics in Multi-Component Multi-Phase System with Spherical Precipitates I. - Theory", *Mater. Sci. Eng. A*, 385 (2004) 166-174.
  45. L. Onsager, "Reciprocal Relations in Irreversible Processes. I.", *Phys. Rev.*, 37 (1931) 405-426.

- 
46. E. Kozeschnik, J. Svoboda, P. Fratzl, F.D. Fischer, "Modelling of kinetics in multi-component multi-phase systems with spherical precipitates II – numerical solution and application", *Mater. Sci. Eng. A*, 385 (2004) 157-165.
  47. J.N. Hobstetter, "Stable Transformation Nuclei in Solids", *Trans. AIME*, 180 (1949) 121-130.
  48. E. Kozeschnik, "Thermodynamic Prediction of the Equilibrium Chemical Composition of Critical Nuclei: Bcc Cu Precipitation in  $\alpha$ -Fe", *Scripta Mater.*, 59 (2008) 1018-1021.
  49. G. Stechauner, S. Primig, E. Kozeschnik, "Early Stages of Cu Precipitation in 15-5 PH Maraging Steel Revisited – Part II: Thermokinetic Simulation", *Steel Res. Int.*, 2016, in print.
  50. F. Soisson, C.C. Fu, "Cu-precipitation kinetics in alpha-Fe from atomistic simulations: vacancy-trapping effects and Cu-cluster mobility", *Phys. Rev. B*, 76 (2007) 1–12.
  51. A.V. Barashev, A.C. Arokiam, "Monte Carlo modelling of Cu atom diffusion in  $\alpha$ -Fe via the vacancy mechanism", *Philos. Mag. Lett.*, 86 (2006) 321–332.
  52. S.I. Golubov, A. Serra, Yu.N. Osetsky, A.V. Barashev, "On the validity of the cluster model to describe the evolution of Cu precipitates in Fe–Cu alloys", *J. Nucl. Mater.*, 277 (2000) 113–115.
  53. T. Jourdan, F. Soisson, E. Clouet, A. Barbu, "Influence of cluster mobility on Cu precipitation in alpha-Fe: a cluster dynamics modeling", *Acta Mater.*, 58 (2010) 3400–3405.
  54. K. Binder, D. Stauffer, "Statistical theory of nucleation, condensation and coagulation", *Adv. Phys.*, 25 (1976) 343–396.
  55. K. Binder, "Theory for the dynamics of clusters: II. Critical diffusion in binary systems and the kinetics of phase separation", *Phys. Rev. B*, 15 (1977) 4425-4447.
  56. S. Primig, G. Stechauner, E. Kozeschnik, "Early Stages of Cu Precipitation in 15-5 PH Maraging Steel Revisited – Part I: Experimental Analysis ", *Steel Res. Int.*, 2016, in print.

# **Section B**

## **Scientific Papers**

# Paper one

Self-Diffusion in Grain Boundaries and Dislocation Pipes in Al, Fe,  
and Ni and Application to AlN Precipitation in Steel

Georg Stechauner and Ernst Kozeschnik

Journal of Materials Engineering and Performance

Volume 23, Year 2014, pages 1576-1579.

# Self-diffusion in grain boundaries and dislocation pipes in Al, Fe and Ni and application to AlN precipitation in steel

G. Stechauner<sup>a,\*</sup> and E. Kozeschnik<sup>b</sup>

<sup>a</sup> Materials Center Leoben Forschung GmbH, Leoben, Austria

<sup>b</sup> „Christian Doppler Laboratory for Early Stages of Precipitation“, Institute of Materials Science and Technology, Vienna University of Technology, Austria

\* Corresponding author: georg.stechauner@tuwien.ac.at

## Abstract

Diffusion along microstructural defects, such as grain boundaries or dislocation pipes, is significantly faster than diffusion through an undisturbed crystal. The ratio of diffusion enhancement is 3-4 orders of magnitude close to the melting point and reaches up to several ten orders of magnitude close to room temperature. An assessment of literature shows a large scatter in the available data and emphasizes the need for representative mean values. Applying a least mean square fit to selected experimental information delivers temperature-dependent functions for the ratio of grain boundary and dislocation pipe to bulk diffusion, respectively. We demonstrate that application of the attained results in a computational framework for the kinetics of precipitation makes the predictive simulation possible for the evolution of particles located at dislocations and grain boundaries.

## 1. Introduction

Diffusion in solids is a well-known phenomenon and has been investigated heavily over the last decades. Accurate assessments of bulk self-diffusion in Al and Ni have been performed by Campbell [1] and in Fe by Fridberg et al. [2] and Jönsson [3], respectively. The assessed data for the bulk diffusion rates, that is diffusion in an equilibrated and defect-poor alloy, lie predominantly within a narrow confidence band and are generally in good agreement with each other. However, the acceleration of diffusion kinetics along short-circuit paths, such as grain boundaries or dislocation pipes, is rather complex. Data and publications on this topic are sparse in some systems, and the scatter of data can be in the range of several orders of magnitude. Simple temperature extrapolation of individual sets of data is not advisable and, even within the measured temperature range, uncertainties remain.

Kaur and Gust [4] have reviewed grain boundary and dislocation pipe diffusion data in the eighties. Since then, a handful of newer experiments have become available, which are taken into account in the present assessment. After analysis of the dislocation and grain boundary diffusion

coefficients obtained in our analysis, these results are utilized in a study of AlN formation along grain boundaries and dislocations in microalloyed steel.

## 2. Experimental challenges

Obtaining reliable values for diffusion coefficients over a wide range of temperatures is a challenging task. Several effects must be taken into account that can lead to unavoidable scatter in the data. Whereas the bulk diffusion rate is a quantity that can be obtained experimentally by relatively easy means, grain boundary and, even more so, dislocation pipe self-diffusion are dependent on various factors and they are significantly more difficult to measure. One major reason in this context is the tremendous effect of material purity on the diffusion rate. Whereas older research [5] is sometimes contradicting more recent publications [6-8], it seems accepted, nowadays, that an increase in purity will increase the resulting diffusion rates, for instance, along grain boundaries. In addition to purity, the misorientation of the grain boundary is an important factor, carrying even the possibility of the occurrence of coincidence site lattices. An increase in misorientation generally increases the diffusion rate, as long as no coincidence site lattices occur [9]. Consequently, even experiments that are very similar in purity and other parameters yield a considerable scatter.

The use of radiotracers and serial-sectioning is the method of choice in Ni and Fe system, where the isotopes  $^{63}\text{Ni}$  and  $^{59}\text{Fe}$  are readily available. For the Al system, tracer self-diffusion measurements are difficult to obtain because the only useful tracer isotope is  $^{26}\text{Al}$ . Since this isotope has a half-life of  $7.4 \cdot 10^5$  years, the number of radioactive counts available in the experiment is rather low [9]. Complex investigation methods must generally be applied to gather data on Al self-diffusion [10,11]. Detailed information on this issue is reported in ref. [4]. For the diffusion along fcc-Fe dislocation pipes, no experimental data are accessible to the authors. Consequently, in the present work, we assume that this quantity has a similar value as that for Ni, as they share the same crystal structure and a melting temperature in the same order of magnitude.

## 3. Statistical analysis

The original data sources for Ni [7,12-15], Al [10,11,16], bcc-Fe [5, 17-19] and fcc-Fe [20-22] short-circuit self-diffusion are plotted in Figure 1. For the sake of clarity, we show the experimental diffusion rates only at the reported maximum/minimum temperature as obtained from the  $Q$  and  $D_0$  values given in the respective literature sources. Details on the assessment procedure are reported elsewhere [23].

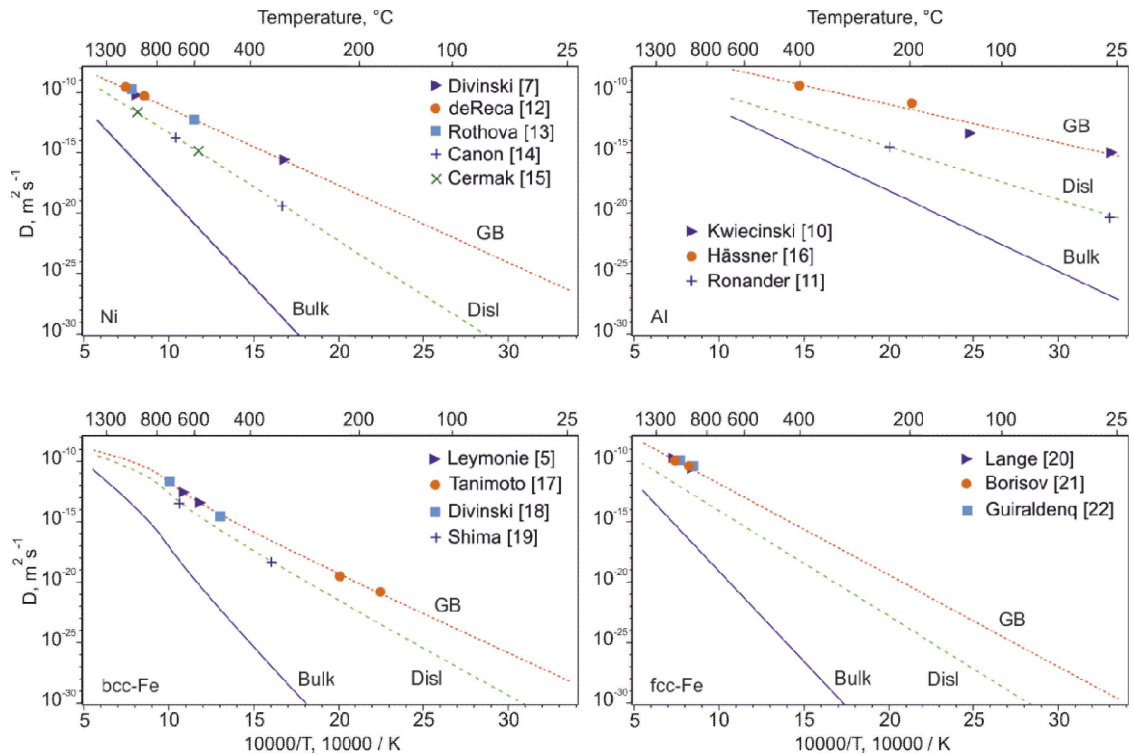


Figure 1 - Arrhenius plots showing the effective self-diffusion rates along grain boundaries (GB), dislocation pipes (Disl) and bulk, respectively, for Ni, Al and Fe.

The fits are performed in such a way that a single mathematical equation describes the data over the entire temperature regime. For bcc-Fe, three separate regions need to be accounted for to consider the transition from ferro- to paramagnetic ordering. The following Tables 1 and 2 summarize the values for activation energy and pre-exponential factor, which are used here to calculate the diffusion ratio  $D_{\text{GB}}/D_{\text{Bulk}} = D_{0,\text{GB}}/D_{0,\text{Bulk}} \cdot \exp(-(Q_{\text{GB}} - Q_{\text{Bulk}})/RT)$ . The ratio for  $D_{\text{Disl}}/D_{\text{Bulk}}$  can be obtained likewise by using  $Q$  and  $D_0$  for dislocation pipes.

Table 1 - Activation energy and pre-exponential factors as shown in Fig. 1 for Ni, Al and fcc-Fe

		$Q$ [kJ/mol]	$D_0$ [ $\text{m}^2/\text{s}$ ]	Source
<b>Ni</b>	Bulk	287	$2.3 \cdot 10^{-4}$	Ref. [1]
	GB	122	$1.2 \cdot 10^{-5}$	this work
	Disl	171	$4 \cdot 10^{-5}$	this work
<b>Al</b>	Bulk	127.2	$1.40 \cdot 10^{-5}$	Ref. [1]
	GB	60.2	$2.00 \cdot 10^{-5}$	this work
	Disl	83.2	$1.50 \cdot 10^{-6}$	this work
<b>fcc-Fe</b>	Bulk	286	$7 \cdot 10^{-5}$	Ref. [2]
	GB	145	$5.5 \cdot 10^{-5}$	this work
	Disl	167	$4.5 \cdot 10^{-6}$	this work

Table 2 - Activation energy and pre-exponential factors as shown in Fig. 1 for bcc-Fe

bcc-Fe	low T		medium T		high T		Source
	RT – 693K		693K – 1214K		1214K – T <sub>m</sub>		
	Q [kJ/mol]	D <sub>0</sub> [m <sup>2</sup> /s]	Q [kJ/mol]	D <sub>0</sub> [m <sup>2</sup> /s]	Q [kJ/mol]	D <sub>0</sub> [m <sup>2</sup> /s]	
<b>Bulk</b>	285	6*10 <sup>-4</sup>	330	1.5	240	2*10 <sup>-4</sup>	Fitted Ref. [3]
<b>GB</b>	125	6*10 <sup>-7</sup>	170	1.5*10 <sup>-3</sup>	80	2*10 <sup>-7</sup>	this work
<b>Disl</b>	150	1.5*10 <sup>-6</sup>	195	3.8*10 <sup>-3</sup>	105	5*10 <sup>-7</sup>	this work

#### 4. Application to AlN precipitation at grain boundaries and dislocations of microalloyed steel

Precipitation of carbides and nitrides in microalloyed steel is of high technical relevance, since the interaction of precipitates and dislocations provides one of the major strengthening mechanisms in metals [24]. In addition, precipitates can pin grain boundaries and, thus, provide a convenient means for controlling grain size evolution during heat treatment.

With the thermo-kinetic software package MatCalc (<http://matcalc.at>), which is developed for the simulation of precipitation kinetics in multi-component systems, the evolution of AlN precipitates in microalloyed steel is calculated. We utilize the thermodynamic database mc\_fe.tdb [25] and the mobility database mc\_fe.ddb [26], which are based on the CALPHAD approach, to evaluate the precipitation kinetics of the AlN particles at dislocations and grain boundaries. We have chosen this example because Al impurity diffusion is linked linearly to the self-diffusion coefficient of Fe, as documented in the work of Fridberg et al [2]. The diffusion data and ratios reported in the previous section are implemented for precipitation at grain boundaries according to the model that has been developed recently by Kozeschnik et al. [27], utilizing the grain boundary diffusion coefficient as one of the key input parameters. Dislocation pipe diffusion enters the simulations in determining the number of potential nucleation sites for precipitation as well as accelerating diffusion in terms of the effective diffusion coefficients. The exact treatment of this effect is described in ref. [28]. Since the diffusivity of interstitial N is significantly faster than the diffusivity of the substitutional element Al, we consider Al as the rate-controlling element for diffusion-controlled growth of AlN. Consequently, the effect of heterogeneous diffusion is only taken into account for the substitutional element Al. The chemical composition used in the simulations is given in Table 3.

Table 3 - Chemical composition of alloys (in wt.-%)

Lit.	Al	N	C	O
[29]	0.046	0.0067	0.001	0.049
[30]	0.055	0.024	0.18	-

Figures 2 and 3 show the experimental phase fraction of AlN together with the simulated curves for precipitation on grain boundaries and dislocations, respectively. In determining the experimental phase fractions, Brahmi and Borelly [29] performed annealing in silica capsules containing low He pressures in salt-baths and air-furnaces and low temperature aging in oil baths. König and Scholz [30] performed annealing in salt-baths and air-furnaces. In the simulations, precipitates of AlN are considered in two populations nucleating at grain boundaries and dislocations, respectively. Values for grain boundary size and dislocation density of  $7.5\mu\text{m}$  and  $10^{12} [\text{m}^{-2}]$  for ferrite, and  $50\mu\text{m}$  and  $10^{11} [\text{m}^{-2}]$  for austenite, consider the actual sample microstructure and have been used in simulations before [31]. To demonstrate the effect of heterogeneous diffusion on the precipitate evolution, the phase fraction calculated with the proposed values is compared to no diffusion enhancement at grain boundaries and dislocations. Both figures show clearly the high impact and importance of the assessed diffusion ratios.

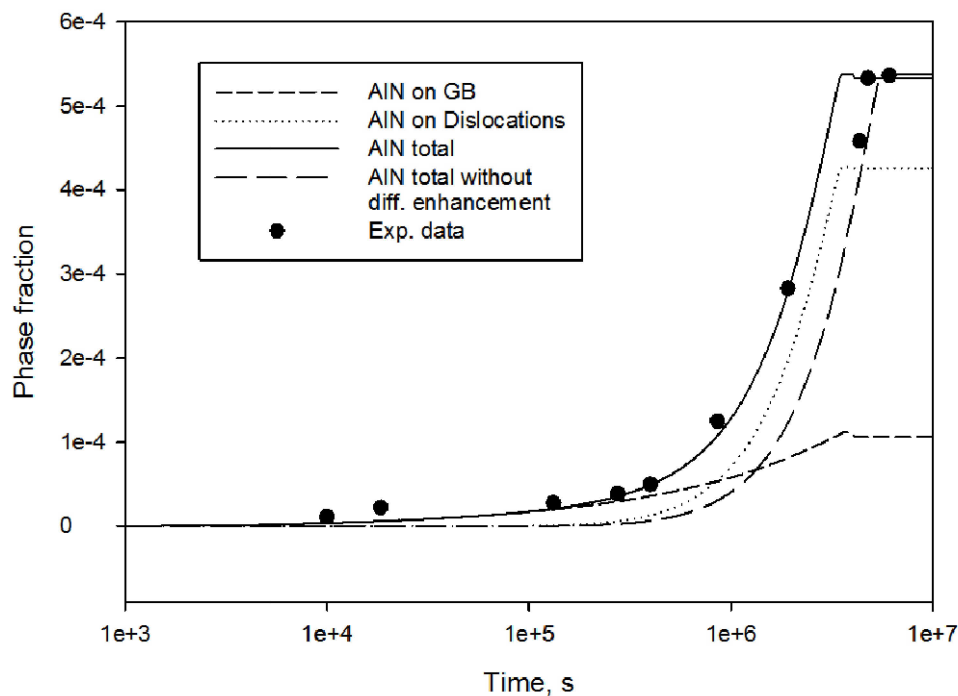


Figure 2 - Phase fraction evolution of AlN in ferrite at 500°C in a microalloyed steel [29] with 0.046 wt.-% Al and 0.0067 wt.-% N, determined by thermoelectric power measurements.

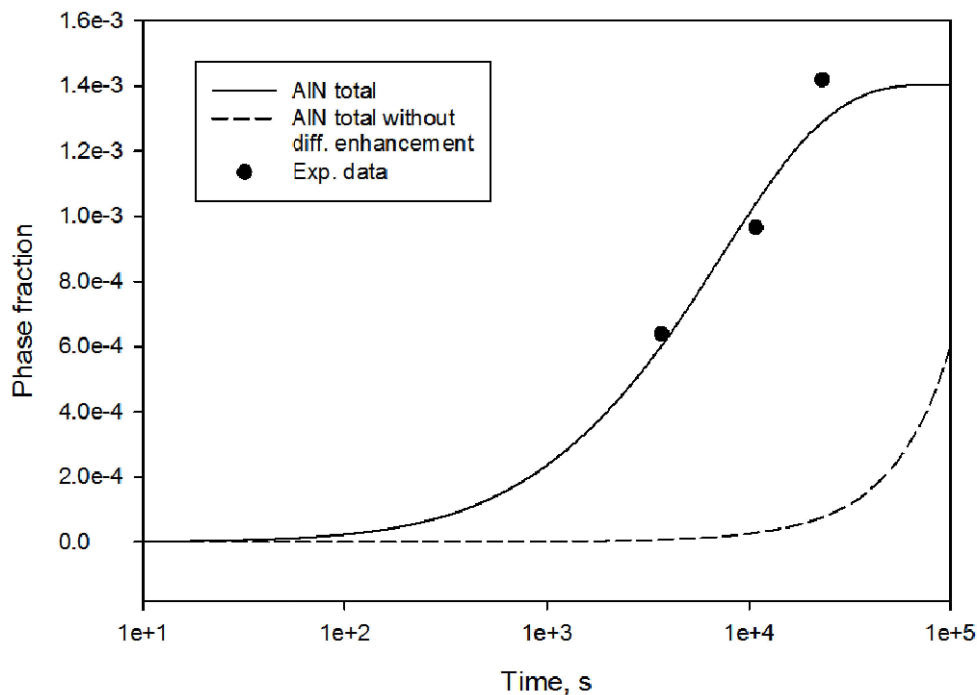


Figure 3 - Phase fraction evolution of AlN in austenite at 1100°C in a microalloyed steel [30] with 0.055 wt.-% Al and 0.024 wt.-% N, determined by analytical chemistry.

## 5. Summary

Diffusion along grain boundaries and dislocation pipes is significantly faster than bulk diffusion. The ratio comparing diffusion along these short-circuit paths with the bulk values is a main input parameter for thermo-kinetic simulations, concerning the nucleation and growth of precipitates. Compared to previously used estimates, mainly based on crystallographic structure, the major improvement of our proposed diffusion ratios is the reproduction of available literature data in the form of representative mean values. The evaluation of diffusivity in each system, Al, Fe and Ni, by a least mean square fit delivers the activation energy  $Q$  and pre-exponential factor  $D_0$  between room temperature up to the melting temperature.

It is demonstrated that the simulation of heterogeneous AlN precipitation in microalloyed steel delivers accurate results. In the simulations, two populations of precipitates, nucleating on grain boundaries and dislocation pipes, respectively, are considered. Only if short-circuit diffusion is taken into account, the experimental data can be reproduced in a satisfactory manner.

## Acknowledgement

Financial support by the Austrian Federal Government (in particular from the Bundesministerium für Verkehr, Innovation und Technologie and the Bundesministerium für Wirtschaft, Familie und Jugend) and the Styrian Provincial Government, represented by Österreichische Forschungsförderungsgesellschaft mbH and by Steirische Wirtschaftsförderungsgesellschaft mbH, within the research activities of the K2 Competence Centre on “Integrated Research in Materials, Processing and Product Engineering”, operated by the Materials Center Leoben Forschung GmbH in the framework of the Austrian COMET Competence Centre Programme, is gratefully acknowledged.

## References

1. C.E. Campbell, A.L. Rukhin, "Evaluation of self-diffusion data using weighted means statistics", *Acta Mater.*, 59 (2011) 5194-5201.
2. J. Fridberg, L.-E. Törndahl, M. Hillert, "Diffusion in iron", *Jernkont. Ann.*, 153 (1969) 263-276.
3. B. Jönsson, "On Ferromagnetic Ordering and Lattice Diffusion – A Simple Model", *Z. Metallkd.*, 83 (1992) 349-355.
4. I. Kaur, W. Gust, "12 Grain and interphase boundary diffusion, in: Landolt-Börnstein - Group III Condensed Matter: Numerical Data and Functional Relationships in Science and Technology, Volume 26: Diffusion in Solid Metals and Alloys", *SpringerMaterials*, 2012.
5. C. Leymonie, Y. Adda, A. Kirianenko, P. Lacombe, "Nouvelle détermination des constantes d'autodiffusion intergranulaire du fer cubique centre", *C.R. Acad. Sci. Paris*, 248 (1959) 1512-1515, in French.
6. H. Hänsel, L. Stratmann, H. Keller, H.J. Grabke, "Effects of the Grain Boundary Segregants Phosphorus, Sulfur, Carbon and Nitrogen on the Grain Boundary Self-Diffusivity in Alpha-Iron", *Acta Metall.*, 33 (1985) 659-665.
7. S.V. Divinski, G. Reglitz, G. Wilde, "Grain boundary self-diffusion in polycrystalline nickel of different purity levels", *Acta Mater.*, 58 (2010) 386-395.
8. T. Surholt, C. Herzig, "Grain boundary self-diffusion in Cu polycrystals of different purity", *Acta Mater.*, 45 (1997) 3817-3823.
9. N.L. Peterson, "Self-diffusion in pure metals", *J. Nucl. Mater.*, 69&70 (1978) 3-37.
10. J. Kwiecinski, J.W. Wyrzykowski, "Investigation of grain boundary self-diffusion at low temperatures in polycrystalline aluminium by means of the dislocation spreading method", *Acta Metall. Mater.*, 39 (1991) 1953-1958.

11. E. Ronander, S. Kritzinger, "A quantitative study of anomalous annealing phenomena in quenched aluminum", *J. Appl. Phys.*, 49 (1978) 3980-3986.
12. N.W. deReca, C.A. Pampillo, "Grain boundary diffusivity via bulk diffusion measurements during grain growth", *Scripta Metall. Mater.*, 9 (1975) 1355-1361.
13. V. Rothova, J. Bursik, M. Svoboda, J. Cermak, "Grain Boundary self-diffusion in Nickel", *Defect Diffus. Forum*, 263 (2007) 207-212.
14. R.F. Canon, J.P. Stark, "Grain Boundary Self-Diffusion in Nickel", *J. Appl. Phys.*, 40 (1969) 366-373.
15. J. Cermak, Z. Cochnar, "Self-diffusion of  $^{63}\text{Ni}$  along dislocations", *Mater. Sci. Eng.*, 174 (1994) 9-13.
16. A. Hässner, "Untersuchung der Korngrenzdifffusion von Zn-65 in alpha-Aluminium-Zink-Legierungen", *Krist. Tech.*, 9 (1974) 1371-1388, in German.
17. H. Tanimoto, P. Farber, R. Würschum, R.Z. Valiev, H.-E. Schaefer, "Self-diffusion in high-density nanocrystalline Fe", *Nanostruct. Mater.*, 12 (1999) 681-684.
18. S.V. Divinski, J. Geise, E. Rabkin, C. Herzig, "Grain boundary self-diffusion in  $\alpha$ -iron of different purity: effect of dislocation enhanced diffusion", *Z. Metallkd.*, 95 (2004) 945-952.
19. Y. Shima, Y. Ishikawa, H. Nitta, Y. Yamazaki, K. Mimura, M. Isshiki, Y. Iijima, "Self-diffusion along dislocations in ultra high purity iron", *Mater. Trans.*, 43 (2002) 173-177.
20. W. Lange, A. Hässner, G. Mischer, "Messung der Korngrenzendifffusion von Nickel-63 in Nickel und  $\gamma$ -Eisen", *Phys. Stat. Sol.*, 5 (1964) 63-71, in German.
21. V.T. Borisov, V.M. Golikov, G.V. Scherbedinskiy, "Relation between diffusion coefficients and grain boundary energy", *Fiz. Metal. Metalloved.*, 17 (1964) 881-885.
22. P. Guiraldenq, P. Lacombe, "Mesure des coefficients d'autodiffusion intergranulaire du fer en phase  $\gamma$  et comparaison avec l'autodiffusion aux joints de grains du fer  $\alpha$ ", *Acta Metall.*, 13 (1965) 51-53, in French.
23. G. Stechauner, E. Kozeschnik, "Assessment of substitutional self-diffusion along short-circuit paths in Al, Fe and Ni", *CALPHAD*, 47 (2014) 92-99.
24. T. Gladman, D. Dulieu, I. D. McIvor, "Structure-Property Relationships in High-Strength Microalloyed Steels", *In Proceedings of an International Symposium on High-Strength, Low-Alloy Steels*, Washington DC, USA, October 1975.
25. E. Povoden-Karadeniz, *Thermodynamic database mc\_fe\_v2.008.tdb*, 2013.
26. E. Povoden-Karadeniz, *Mobility database mc\_fe\_v2.000\_prebeta\_004*, 2013.

27. E. Kozeschnik, J. Svoboda, R. Radis, F.D. Fischer, "Mean-field model for the growth and coarsening of stoichiometric precipitates at grain boundaries", *Model. Simul. Mater. Sc.*, 18 (2010) 1-19.
28. R. Radis, E. Kozeschnik, "Numerical simulation of NbC precipitation in microalloyed steel", *Model. Simul. Mater. Sci. Eng.*, 20 (2012) 1-15.
29. A. Brahmi, R. Borrelly, "Study of Aluminium Nitride Precipitation in Pure Fe-Al-N Alloy by Thermoelectric Power Measurements", *Acta Mater.*, 45 (1997) 1889-1897.
30. P. König, W. Scholz, H. Ulmer, "Wechselwirkung von Aluminium, Vanadium und Stickstoff in aluminiumberuhigten, mit Vanadin und Stickstoff legierten schweißbaren Baustählen mit rd. 0,2 % C und 1,5 % Mn", *Archiv für das Eisenhüttenwesen*, 32 (1961) 541-556, in German.
31. R. Radis, E. Kozeschnik, "Kinetics of AlN precipitation in microalloyed steel", *Model. Simul. Mater. Sci. Eng.*, 18 (2010) 1-16.

# Paper two

Assessment of Substitutional Self-Diffusion along Short-Circuit  
Paths in Al, Fe and Ni

Georg Stechauner and Ernst Kozeschnik

CALPHAD

Volume 47, Year 2014, pages 92-99.

# Assessment of substitutional self-diffusion along short-circuit paths in Al, Fe and Ni

G. Stechauner<sup>a,\*</sup> and E. Kozeschnik<sup>b</sup>

<sup>a</sup> Materials Center Leoben Forschung GmbH, Leoben, Austria

<sup>b</sup> „Christian Doppler Laboratory for Early Stages of Precipitation“, Institute of Materials Science and Technology, Vienna University of Technology, Austria

\* Corresponding author:

georg.stechauner@tuwien.ac.at

Georg Stechauner

Favoritenstraße 9-11 / E308

1040 Wien

Austria

+43 1 58801-30847

## Abstract

The kinetics of self-diffusion along grain boundaries and dislocations (pipe diffusion) is analyzed in Al,  $\alpha$ - and  $\gamma$ -Fe and Ni. The available experimental information is critically reviewed. The suggested values given in the present work are assessed with focus on consistency and applicability to thermo-kinetic simulation. The proposed data are evaluated between room temperature and the melting point.

## Keywords

Diffusion ratio; activation energy; frequency factor; grain boundary; dislocation pipe

## Research Highlights

- Assessment of activation energy and frequency factor on short-circuit paths in Al, Fe, and Ni
- Consistent ratios over temperature range from melting point to room temperature
- Ready-to-use diffusion ratios for thermo-kinetic simulations

## 1. Introduction

The availability of reliable short-circuit self-diffusion diffusion data is a prerequisite for physically-based simulation of diffusion-controlled phase transformations involving grain boundaries (GB) and dislocations (Disl). Diffusion along these fast penetration paths strongly impacts, for instance, the formation of precipitates residing at these heterogeneous nucleation sites. In computer simulations of precipitation, dislocation-pipe and grain boundary diffusion are essential physical mechanisms and the accuracy of simulations relies strongly on the availability of these data, e.g., refs. [1,2]. Unfortunately,

short-circuit self-diffusion diffusion data covering a wide range of temperatures are sparse and often contradictory, while consistent assessments of the bulk diffusivities for the Ni- and Al-system by Campbell and Rukhin [3], for  $\alpha$ - and  $\delta$ -Fe by Jönsson [4] and for  $\gamma$ -Fe by Fridberg et al. [5] are readily at hand.

In the present work, we reassess the available literature data on dislocation pipe and grain boundary diffusion in Fe, Al and Ni. Suggested values on the diffusion enhancement along the short circuit paths are given in the form of activation energies and pre-exponential factors. Since the theoretical background for dislocation and grain boundary diffusion is discussed by, e.g., Peterson [6], Baluffi [7] and Gjostein [8], respectively, we will not review this topic here.

## 2. Assessment

Diffusion is a thermally activated process and it generally follows an Arrhenius law. The diffusion coefficient  $D$  is commonly expressed as

$$D = D_0 \exp\left(-\frac{Q}{RT}\right), \quad \text{Eq. 1}$$

where  $D_0$  is the pre-exponential factor, also denoted as the frequency factor, and  $Q$  is the activation energy for diffusion.  $R$  is the gas constant and  $T$  is temperature.

A general treatment of diffusion rate acceleration due to grain boundaries and dislocation pipes is given by Klotsman et al. [9] and Hong et al. [10], respectively. They propose a reduced activation energy for short-circuit self-diffusion diffusion with  $Q_{\text{GB}}/Q_{\text{Bulk}} \sim 0.3 - 0.4$  and  $Q_{\text{Disl}}/Q_{\text{Bulk}} \sim 0.57 - 0.74$ , respectively, where  $Q_{\text{Bulk}}$  is the activation energy for diffusion in the bulk crystal lattice. These ranges hold considerably well against experimental results and also satisfy the experimentally observed slopes for the temperature dependence of the diffusion coefficient in a general picture [11]. However, upon extrapolation of the independent activation energies up to melting temperature, to obtain the frequency factor  $D_0$ , the values span several orders of magnitude.

Schematic illustrations of the spectrum of observed diffusion data are given in refs. [8,11]. While these figures are viable to demonstrate the general operative mechanisms and correlations, one must use these data with care when applying to phase transformation calculations that depend on short-circuit self-diffusion coefficients. It is the aim of this work, to deliver consistent diffusion ratios covering the temperature range from melting point to room temperature, based on available literature data obtained with a variety of experimental techniques.

The assessment process in the present work is performed in two steps: first, the experimental diffusion data from primary literature are plotted in an Arrhenius diagram to determine  $Q$  and  $D_0$  by a least mean square fit. Where no experimental data points are available, we use the values of  $Q$  and  $D_0$  as proposed by the referenced works to calculate data points at critical temperature regions. In a second step, we plot all experimental information in a single figure and identify outliers, i.e., values that are clearly not in agreement with other measurements. By fitting a curve to this scatter-plot, we obtain  $Q$  and  $D_0$  for grain boundaries and dislocation pipes, respectively. This enables us to calculate the diffusion ratios as

$$\frac{D_{\text{GB}}}{D_{\text{Bulk}}} = \frac{D_{0,\text{GB}}}{D_{0,\text{Bulk}}} \exp\left(-\frac{Q_{\text{GB}} - Q_{\text{Bulk}}}{RT}\right), \quad \text{Eq. 2}$$

$$\frac{D_{\text{Disl}}}{D_{\text{Bulk}}} = \frac{D_{0,\text{Disl}}}{D_{0,\text{Bulk}}} \exp\left(-\frac{Q_{\text{Disl}} - Q_{\text{Bulk}}}{RT}\right). \quad \text{Eq. 3}$$

Consequently, the suggested values for the relative grain boundary and dislocation diffusion are given as ratios with respect to the accepted bulk diffusivities from Campbell and Rukhin [3], Jönsson [4] and Fridberg et al. [5]. Using Eqs. 2 and 3 together with the results summarized in Tables 2, 4, 6 and 8, the effective diffusion ratios in the underlying systems are assessed.

Finally, we have to emphasize an important aspect of diffusion along short-circuit paths, relating to the particular constitution of the dislocation or grain boundary. The effective short-circuit diffusion rates presented here are not unique quantities for a single “general” high-angle grain boundary or a “general” dislocation. Instead, these rates strongly depend on, e.g., the grain boundary misorientation, the dislocation character, being either of edge or screw type or a mixture of these, or the segregation state of elements at these heterogeneous sites. Each of these factors can change the diffusion rates by several orders of magnitude, which is reflected also in the observed scatter of experimental data. When utilizing the proposed ratios in kinetic simulations, one has to be aware that a single formulation for the diffusion coefficients is a severe simplification, while, in reality, the subject is much more involved. A state-of-the-art discussion of this topic was given by Sommer and Herzig [12], Divinski et al. [13] and Bokstein and Divinski [14].

### 3. Results and Discussion

The available experimental results for grain boundary and dislocation pipe diffusion commonly contain the quantities  $\delta$  and  $a^2$ , which represent the grain boundary thickness and the cross-sectional area of the dislocation pipe, respectively. In our assessment, we use the commonly accepted values for

$\delta$  and  $a$  of 0.5nm, according to refs. [11,14]. These are effective values measured on a series of self-diffusion experiments in various systems and allow for a consistent treatment throughout literature [14]. They were also confirmed by Sommer and Herzig [12] who measured  $D_{GB}$  and  $D_{Disl}$  directly and used  $\delta$  and  $a$ , respectively, as factors for comparison with other results inherently containing these quantities. We adopt this approach in the present work.

In the analysis of the experimental results, the purity of the samples is given in the “N”-notation. The leading digit represents how many 9s are in the purity, the trailing digit gives the last digit of the purity (e.g.: 3N5 = 99.95 wt.-% purity). The temperatures denote the confidence range where experiments have been performed. If only  $Q$  and  $D_0$  are given in the primary literature, two arbitrary data points are calculated and displayed in the graphs.

### 3.1 Aluminium

For the assessment of short-circuit self-diffusion in Al, only limited amount of literature sources are available. The reason for this is probably founded in the unavailability of convenient Al isotopes for radioactive tracer experiments. Whereas  $^{59}\text{Fe}$  and  $^{63}\text{Ni}$  are suitable isotopes for measuring diffusion in Fe and Ni, the only isotope for Al that can be used is  $^{26}\text{Al}$ . However, the large half-life of  $7.4 \cdot 10^5$  years produces only weak radioactive signals in the sectioning experiments [15]. Table 1 comprises the available data on Al short circuit diffusion.

Table 1 – Summary of Al grain boundary and dislocation pipe self-diffusion information

Ref	Material / purity	Temp. range [K]	Diffusion path	$Q$ kJ/mol	$D_0$ m <sup>2</sup> /s	# of data points	Experimental method
[16]	-	-	GB	60.2	$1.9 \cdot 10^{-5}$	-	-
[17]	-	523 - 623	GB	48.4	$3.3 \cdot 10^{-6}$	3	-
[18]	4N	473 - 673	GB	48.8	$2.7 \cdot 10^{-6}$	5	Theoretical estimate
[19]	4N, 4 $\mu\text{m}$	293 - 403	GB	29.1	$8.1 \cdot 10^{-11}$	3	Dislocation spreading
[19]	4N, 22 $\mu\text{m}$	293 - 403	GB	43.2	$2.9 \cdot 10^{-8}$	3	Dislocation spreading
[20]	6N	323 - 454	Disl	80.2	$7.9 \cdot 10^{-7}$	38	Defect annealing
[21]	4N	-	Disl	84.7	$2.3 \cdot 10^{-6}$	-	Defect annealing

Kwiczinski and Wyrzykowski [19] performed investigations of short-circuit self-diffusion based on the dislocation spreading method, which is based on the interaction of lattice dislocations with GBs. The samples were deformed to ensure the occurrence of so called trapped lattice dislocations (TLDs) on all grain boundaries. At elevated temperatures, these TLDs undergo dissociation with the

kinetics being controlled by GB diffusion, leading to fractions of GBs with visible TLDs less than unity. In order to compare the provided data to other methods, we extrapolate to a fraction of unity.

Hässner [18] investigated the diffusion kinetics of  $^{65}\text{Zn}$  in Al and Al-Zn alloys experimentally. On basis of his measurements, together with data from Seeger [16] and energies provided by Shine and d'Heurle [22], he derived a theoretical estimate for GB self-diffusion of Al.

When studying the diffusion rates as a function of the GB tilt angle, cusps occur in the samples, which correlate with coincidence site lattices [17]. Since GBs in polycrystals have no preferred orientation, the obtained diffusivities represent average rates, which are assumed to be shifted towards the highest diffusivities [8]. This suggestion is also utilized in the determination of mean diffusion rates for the data of Lange and Jurisch [17].

A graphical representation of the experimental values available for short-circuit Al self-diffusion is presented in Table 1, together with our assessed values as shown in Fig. 1. Table 2 summarizes the proposed values for activation energy and pre-exponential factor for the homogeneous and short-circuit self-diffusion coefficient of Al.

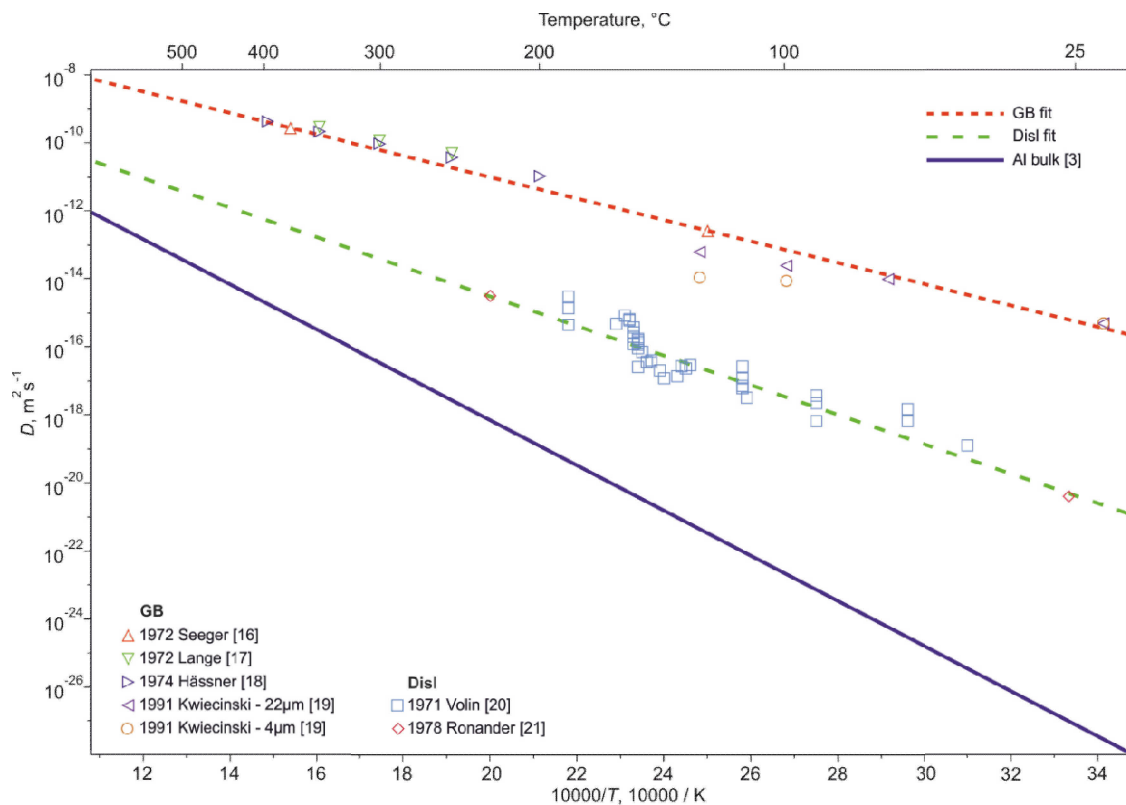


Figure 1 – Experimental and assessed data for grain boundary and dislocation pipe self-diffusion in Al.

Table 2 – Proposed  $Q$  and  $D_0$  for Al grain boundary and dislocation pipe self-diffusion.

	$Q$ [kJ/mol]	$D_0$ [m <sup>2</sup> /s]	Source
Bulk	127.2	$1.4 \cdot 10^{-5}$	Ref. [3]
GB	60.2	$2.0 \cdot 10^{-5}$	this work
Disl	83.2	$1.5 \cdot 10^{-6}$	this work

The diffusion ratios are obtained as

$$\frac{D_{\text{Al,GB}}}{D_{\text{Al,Bulk}}} = 1.4 \exp\left(\frac{67000}{RT}\right), \quad (4)$$

$$\frac{D_{\text{Al,Disl}}}{D_{\text{Al,Bulk}}} = 0.11 \exp\left(\frac{44000}{RT}\right). \quad (5)$$

Here and in the following equations  $R$  is in J/mol·K and  $T$  is in K.

### 3.2 Iron – bcc

Grain boundary and dislocation pipe diffusion in  $\alpha$ -(bcc)-Fe has been targeted in a substantial number of experimental studies, which is partially attributed to the availability of suitable radioisotopes. Consequently, many investigation of short-circuit self-diffusion have been performed with the method of serial sectioning, which commonly delivers reliable results based on direct evaluation of experimental data. The performed assessment is extrapolated to  $\delta$ -(bcc)-Fe regions based on the constant ratio between  $D_{\text{GB}}/D_{\text{Bulk}}$  and  $D_{\text{Disl}}/D_{\text{Bulk}}$ , respectively.

Table 3 starts with summarizing the information on  $\alpha$ -Fe short circuit diffusion as reviewed in the work of Kaur and Gust [23]. Since then, several additional experiments have become available, which are utilized in our present compilation. In the analysis, only experiments in high purity material are considered.

Table 3 –  $\alpha$ -Fe grain boundary and dislocation pipe self-diffusion data

Ref	Material / purity	Temp. range [K]	Diffusion Path	$Q$ kJ/mol	$D_0$ m <sup>2</sup> /s	# of data points	Experimental method
[24]	2N6	852 - 925	GB	154.9	$1.4 \cdot 10^{-4}$	4	Sectioning
[25]	2N7	854 - 1020	GB	170.2	$1.6 \cdot 10^{-3}$	6	Sectioning
[25]	4N	800 - 925	GB	183.8	$3.3 \cdot 10^{-3}$	5	Sectioning
[26]	3N8	980 - 1130	GB	158.2	$1.6 \cdot 10^{-3}$	4	Absorbtion kinetic
[27]	3N5	774 - 955	GB	167.2	$9.7 \cdot 10^{-4}$	9	Sectioning
[8]	-	-	GB	145.8	$7.3 \cdot 10^{-6}$	-	Theoretical estimate
[28]	3N3	836 - 1023	GB	165.6	$6.7 \cdot 10^{-3}$	4	Sectioning
[29]	3N2	877 - 1020	GB	195.4	$3.5 \cdot 10^{-2}$	28	Sectioning
[30]	-	446 - 500	GB	101.1	$1.1 \cdot 10^{-9}$	4	Sectioning
[13]	4N4	770 - 1055	GB	189.5	$2.8 \cdot 10^{-2}$	8	Sectioning
[31]	5N	523 - 1033	GB	164.5	$2.6 \cdot 10^{-1}$	13	Sectioning
[32]	3N	429 - 471	GB	99.4	$3.3 \cdot 10^{-11}$	3	Neutron reflectometry
[33]	3N8	568 - 925	Disl	183.2	$1.7 \cdot 10^{-4}$	10	Sectioning
[34]	5N	625 - 940	Disl	169.3	$1.0 \cdot 10^{-4}$	8 (14)	Sectioning

Early results of Leymonie et al. [24,25], based on the sectioning and radiotracer technique with Fe of 2Nx and 4N purity, suggest an increased diffusion rate for specimens with less purity, which appears to be contradicting. It is accepted, nowadays, that an increased purity will increase the resulting diffusion rates. This was shown, e.g., in Fe by Hänsel et al. [29], in Ni by Divinski et al. [35] and Prokoshkina et al. [36], in Cu by Surholt and Herzig [37] and others. Since our applied fit reproduces the experimental data considerably well for various purity levels, the influence of composition seems to be outweighed by the applied measurement temperature and method. The specimens of Inoue et al. [31] are of highest reported purity. These authors argue that, due to the unprecedented purity, higher diffusivities were achieved compared to many other researchers. In materials of technical interest, this extreme purity is rarely obtained, which is why we have omitted these values in our assessment.

Tanimoto et al. [30] and Schmidt et al. [32] have performed low-temperature experiments on nano-crystalline Fe. The different experimental methods applied deliver a considerable scatter in observed diffusivities (Fig. 2). Tanimoto et al. have performed their radiotracer experiments in nanocrystalline, high density Fe using Ar-ions for sputter sectioning, which disturb the measurement of grain boundary diffusivities in these nano-structured materials [32]. By using neutron reflectometry, Schmidt et al. have measured the diffusion rate without influencing the microstructure. Still, both

experiments bear uncertainties, as the effects of grain boundary diffusion in nano-crystalline materials are far from being understood.

Mehrer and Lübbehusen [33] and Shima et al. [34] have investigated dislocation-pipe diffusion in  $\alpha$ -Fe. Both authors provide comparable results for the 600-700°C region but show some scatter at lower temperatures.

In contrast to our preceding work [38], we included the results of Schmidt et al. [32] and Mehrer and Lübbehusen [33] in the present assessment. In our assessment procedure, this leads to considerably lower diffusion rates, especially in the low temperature region.

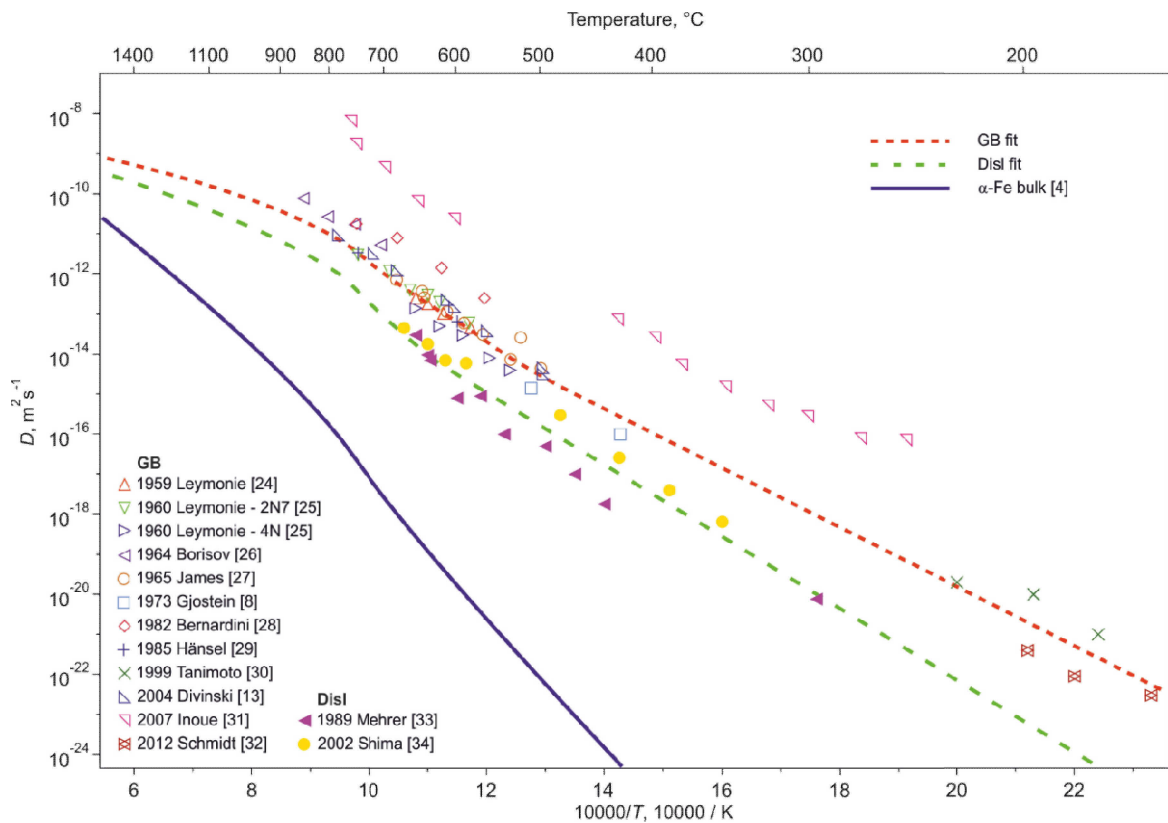


Figure 2 – Experimental data for grain boundary and dislocation pipe diffusion in  $\alpha$ -Fe and corresponding assessments.

The ferro- and paramagnetic ordering in  $\alpha$ -Fe leads to strong bulging in diffusion rates around the Curie temperature. For a reasonable representation of the non-linear diffusivity values, the region from room temperature to the melting point is separated into three ranges: the ferromagnetic region (low  $T$ ), the intermediate region (medium  $T$ ) and the paramagnetic region (high  $T$ ).  $Q$  and  $D_0$ , as fitted from the data in Fig. 2, are summarized in Table 4.

Table 4 - Proposed  $Q$  and  $D_0$  for  $\alpha$ -Fe grain boundary and dislocation pipe self-diffusion.

Temperature region	low $T$		medium $T$		high $T$		Source
	RT – 693K		693 – 1214K		1214 – $T_m$		
	$Q$	$D_0$	$Q$	$D_0$	$Q$	$D_0$	
	[kJ/mol]	[m <sup>2</sup> /s]	[kJ/mol]	[m <sup>2</sup> /s]	[kJ/mol]	[m <sup>2</sup> /s]	
Bulk	285	$6.0 \cdot 10^{-4}$	330	1.5	240	$2.0 \cdot 10^{-4}$	Fitted from Ref. [4]
GB	135	$2.1 \cdot 10^{-6}$	180	$5.3 \cdot 10^{-3}$	90	$7.0 \cdot 10^{-7}$	this work
Disl	155	$1.8 \cdot 10^{-6}$	200	$4.5 \cdot 10^{-3}$	110	$6.0 \cdot 10^{-7}$	this work

Although the absolute values for  $Q$  and  $D_0$  given in Table 4 must be assessed within the individual temperature regimes, the ratios of  $Q_{GB}/Q_{Bulk}$  and  $Q_{Disl}/Q_{Bulk}$ , respectively, can be expressed as single pairs of values due to the fact that the non-Arrhenius temperature dependence of the diffusion coefficient induced by the ferromagnetic transition is already incorporated in the bulk diffusivity. The assessed ratios can be expressed as

$$\frac{D_{r-Fe,GB}}{D_{r-Fe,Bulk}} = 0.0035 \exp\left(\frac{150000}{RT}\right), \quad (6)$$

$$\frac{D_{r-Fe,Disl}}{D_{r-Fe,Bulk}} = 0.003 \exp\left(\frac{130000}{RT}\right). \quad (7)$$

### 3.3 Iron - fcc

The allotropic phase transformation in pure Fe from  $\alpha$  (bcc) to  $\gamma$  (fcc) occurs at a temperature of 911°C. For this reason, no experimental self-diffusion values are reported for  $\gamma$ -Fe below this temperature. Still, lower temperatures can be of interest in technical alloys were the  $\gamma$  region is stabilised by elements, such as Ni, Co, etc. Therefore, we can only provide a low-temperature extrapolation based on the available data for grain boundaries from higher temperatures (Fig. 3).

For dislocation pipe diffusion in  $\gamma$ -Fe, unfortunately, no experimental data has been found. Since Ni and  $\gamma$ -Fe share the same crystal structure and a comparable  $T_m$ , however, we provide an estimate of the short-circuit self-diffusion values for  $Q$  and  $D_0$  in  $\gamma$ -Fe based on the diffusion ratios from Ni. The data for grain boundary diffusion in  $\gamma$ -Fe is compiled in Table 5.

Table 5 – Summary of  $\gamma$ -Fe grain boundary and dislocation pipe self diffusion data

Ref	Material / purity	Temp. range [K]	Diffusion path	$Q$ kJ/mol	$D_0$ m <sup>2</sup> /s	# of data points	Experimental method
[39]	2N6	1273 - 1473	GB	165.0	$1.1 \cdot 10^{-3}$	-	Sectioning
[40]	2N7	1222 - 1432	GB	172.3	$5.1 \cdot 10^{-4}$	-	Sectioning
[41]	-	1213 - 1403	GB	153.6	$8.5 \cdot 10^{-5}$	8	Sectioning
[42]	-	-	GB	158.8	$3.2 \cdot 10^{-4}$	-	-
[26]	3N8	1220 - 1380	GB	100.7	$7.9 \cdot 10^{-7}$	4	Absorbtion kinetic method
[43]	2N7	1196 - 1289	GB	174.6	$1.4 \cdot 10^{-3}$	4	Sectioning
[43]	4N	1191 - 1287	GB	165.9	$4.4 \cdot 10^{-4}$	5	Sectioning
[27]	3N5	949 - 1159	GB	148.7	$3.2 \cdot 10^{-5}$	12	Sectioning
[8]	-	-	GB	127.5	$1.2 \cdot 10^{-4}$	-	Theoretical estimate

The existing grain boundary diffusion data represents a homogenous set with a consistent slope (Fig. 3). The only clear outliers are the values from Gjostein [8], whose data represents a mean diffusion rate for grain boundaries in fcc metals. While the slope fits considerably well, the frequency factor seems to be overestimated.

In order to increase the quantity of experimental data, the restriction for pure self-diffusion was dropped in  $\gamma$ -Fe and data from Lange et al. [41] was additionally considered, providing values for impurity diffusion of  $^{63}\text{Ni}$  along  $\gamma$ -Fe GBs. The results coincide very well with the other authors.

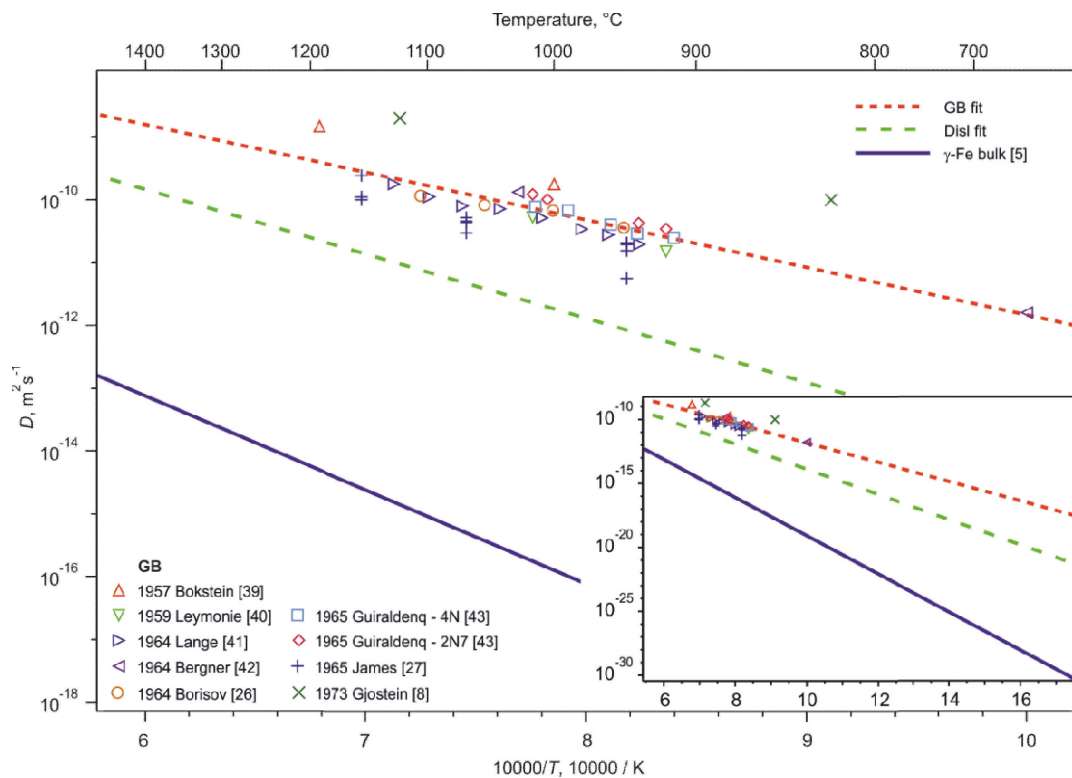


Figure 3 – Experimental data for grain boundary and dislocation pipe diffusion in  $\gamma$ -Fe and corresponding assessments.

The assessed  $Q$  and  $D_0$  values for GB and Disl diffusion are compiled in Table 6.

Table 6 - Proposed  $Q$  and  $D_0$  for  $\gamma$ -Fe grain boundary and dislocation pipe self-diffusion.

	$Q$ [kJ/mol]	$D_0$ [m <sup>2</sup> /s]	Source
<b>Bulk</b>	286	$7.0 \cdot 10^{-5}$	Ref. [5]
<b>GB</b>	145	$5.5 \cdot 10^{-5}$	this work
<b>Disl</b>	185	$4.5 \cdot 10^{-5}$	this work

The ratio for diffusion enhancement along short-circuit paths in  $\gamma$ -Fe are

$$\frac{D_{x-Fe,GB}}{D_{x-Fe,Bulk}} = 0.79 \exp\left(\frac{141000}{RT}\right), \quad (8)$$

$$\frac{D_{x-Fe,Disl}}{D_{x-Fe,Bulk}} = 0.64 \exp\left(\frac{101000}{RT}\right). \quad (9)$$

### 3.4 Nickel

The system, which attracted most interest in the field of short-circuit diffusion measurement, is Ni. A suitable isotope for radioactive tracer analysis, no ferro-magnetic transition and the absence of allotropic transformations lead to convenient experimental boundary conditions. Our proposed fit (Figures 4 and 5) covers most of the experimental data and delivers reasonable results over the whole temperature region. The data for diffusion along grain boundaries and dislocation pipes in Ni is summarized in Table 7.

For the sake of clarity, we present separate figures for grain boundary (Fig. 4) and dislocation pipe diffusion (Fig. 5) in the Ni system. The activation energy of our proposed grain boundary fit shows a similar slope to most available experimental data. Especially, the data of Divinski et al. [35] extrapolate considerably well over the whole temperature range. Whereas most authors report activation energies in the same range, the slopes for refs. [36,47,50] deviate considerably from these data (Fig. 4). Prokoshkina et al. [36] discuss the strong effect of impurities on GB diffusion, which could explain the deviating activation energies. Neuhaus and Herzig [50] discuss a number of potential reasons, which explain the differences, however, these are not further inspected and verified. As the results are in clear contradiction to the large number of consistent results, they are omitted in this evaluation.

Table 7 - Summary of Ni grain boundary and dislocation pipe self diffusion data

Ref	Material / purity	Temp. range [K]	Diffusion path	Q kJ/mol	$D_0$ m <sup>2</sup> /s	# of data points	Experimental method
[44]	3N5, BC - 45°	973 - 1373	GB	102.2	$7.4 \cdot 10^{-7}$	4	Sectioning
[45]	4N	854 - 1025	GB	107.0	$8.7 \cdot 10^{-6}$	8	Sectioning
[41]	-	1123 - 1383	GB	108.6	$6.9 \cdot 10^{-7}$	6	Sectioning
[46]	3N7	748 - 923	GB	116.9	$1.1 \cdot 10^{-5}$	5	Sectioning
[47]	4N	1080 - 1350	GB	231.5	$6.6 \cdot 10^{-2}$	8	Sectioning
[48]	4N	1173 - 1323	GB	129.5	$3.9 \cdot 10^{-5}$	10	Grain growth
[49]	3N7	826 - 1389	GB	113.9	$6.9 \cdot 10^{-6}$	11	Sectioning
[50]	4N8	641 - 1324	GB	184.4	$6.9 \cdot 10^{-2}$	6	Sectioning
[51]	-	900 - 1400	GB	104.4	$6.4 \cdot 10^{-6}$	4	Molecular Dynamics Simulations
[52]	4N5	873 - 1273	GB	124.1	$2.3 \cdot 10^{-5}$	5	Sectioning
[35]	5N	595 - 1250	GB	122.6	$1.0 \cdot 10^{-5}$	7	Sectioning
[36]	4N	584 - 1275	GB	163.5	$3.7 \cdot 10^{-4}$	8	Sectioning
[53]	5N	779 - 872	Disl	155.3	$1.1 \cdot 10^{-2}$	5	Autoradiography
[54]	3N7	600 - 970	Disl	180.4	$1.5 \cdot 10^{-4}$	5	Autoradiography
[55]	4N - PC	853 - 1230	Disl	184.3	$3.3 \cdot 10^{-4}$	6	Sectioning
[55]	4N - MC	666 - 869	Disl	233.3	0.2	5	Sectioning
[55]	Ni-9.8Cr	853 - 1230	Disl	199.6	$1.2 \cdot 10^{-3}$	6	Sectioning

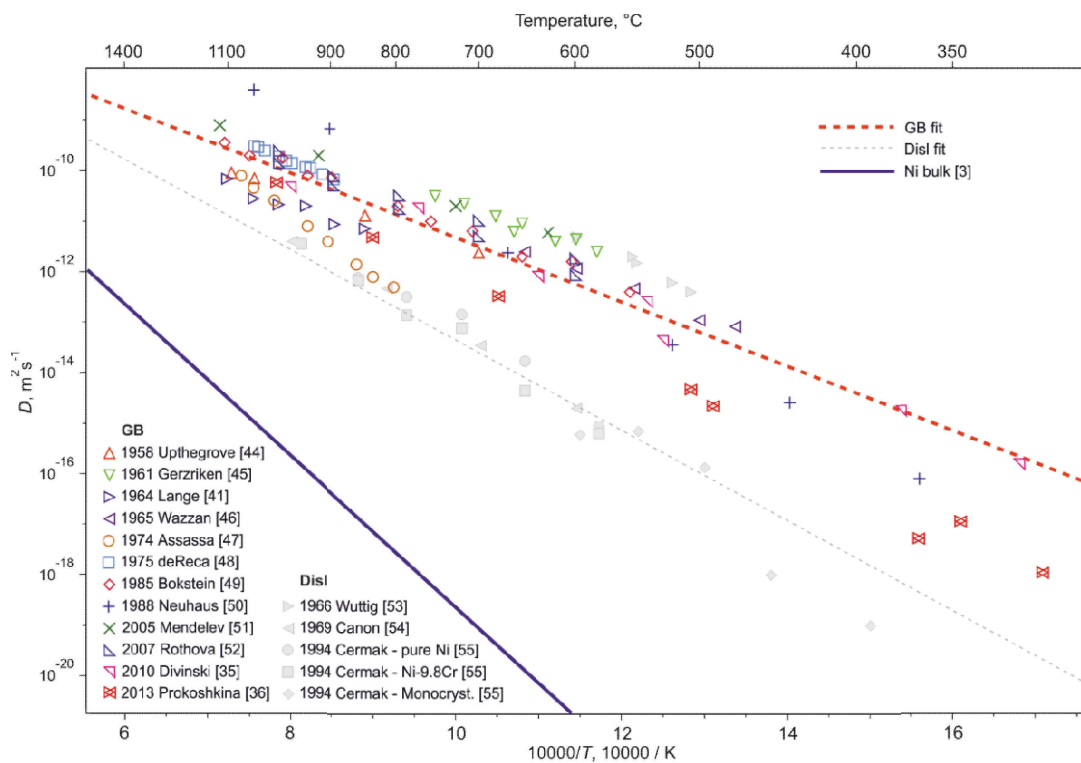


Figure 4 –Experimental data for grain boundary diffusion in Ni and corresponding assessments. Dislocation data is shown in light grey.

The experiments from Canon and Stark [54] have been performed on low-angle grain boundaries. Consequently, these data are considered as dislocation pipe diffusion values, here. They report the structure of the grain boundaries to consist of edge dislocation arrays, activation energies were found using a dislocation pipe model. Both,  $Q$  and  $D_0$  are in agreement with results of other dislocation pipe experiments (Fig. 5).

The other two experiments utilized in the present assessment and focussing on dislocation pipe diffusion have been performed by Cermak and Cochnar [55] and Wuttig and Birnbaum [53], respectively. Whereas the results of the first authors are in good agreement with the data of Canon and Stark, the latter ones report considerably higher diffusion rates. While the activation energy is within the experimental scatter, according to Canon and Stark, no explanation for the difference in the frequency factor values could be identified. Therefore, the values of Wuttig and Birnbaum are excluded from our assessment. The results for pure Ni (monocrystal/MC and polycrystals/PC) and Ni-9.8Cr [55] are comparably close and both are taken into consideration, therefore. The activation energy of the monocrystal data shows some deviation, especially in the low temperature region. For technical reasons, higher emphasis is put on the values from poly-crystals.

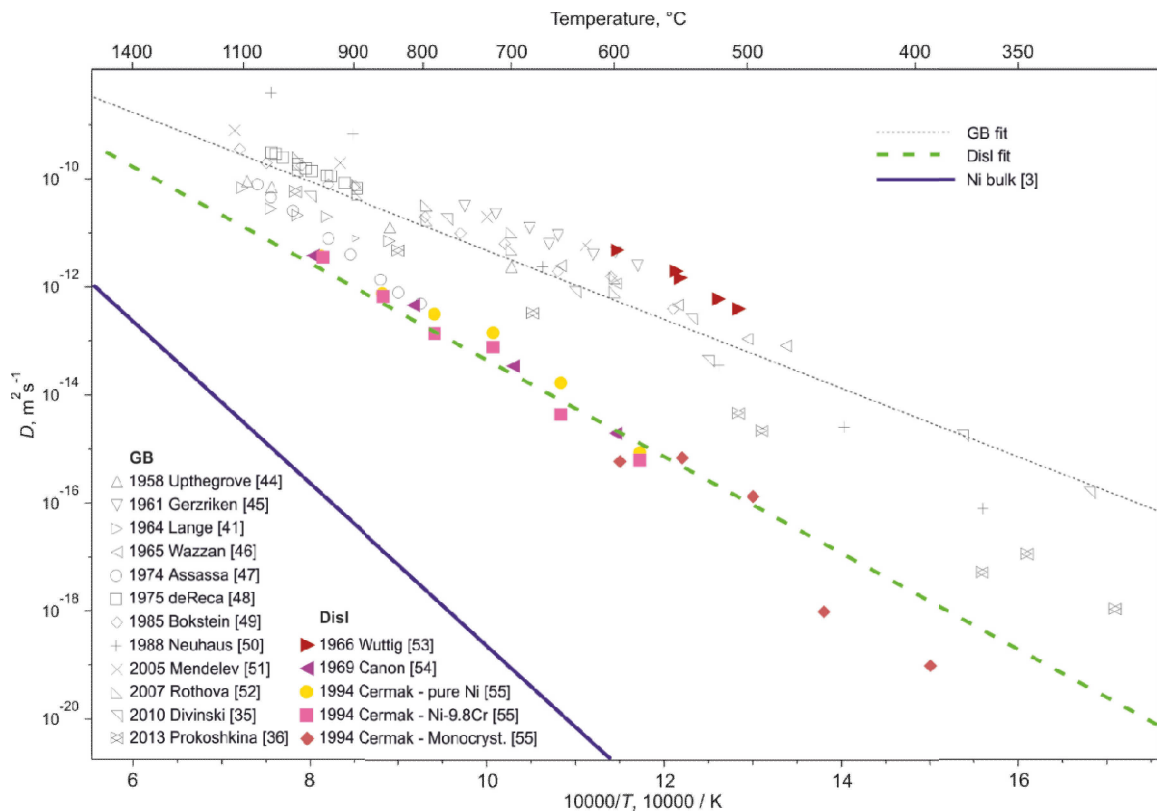


Figure 5 – Highlighted experimental data for dislocation pipe diffusion in Ni and corresponding assessments.

The assessed values for  $Q$  and  $D_0$  are listed in Table 8.

Table 8 – Proposed  $Q$  and  $D_0$  for Ni grain boundary and dislocation pipe self-diffusion.

	$Q$ [kJ/mol]	$D_0$ [m <sup>2</sup> /s]	Source
<b>Bulk</b>	287	$2.3 \cdot 10^{-4}$	Ref. [3]
<b>GB</b>	122	$1.2 \cdot 10^{-5}$	this work
<b>Disl</b>	171	$4.0 \cdot 10^{-5}$	this work

The assessed ratios for the diffusion enhancement in Ni are

$$\frac{D_{\text{Ni,GB}}}{D_{\text{Ni,Bulk}}} = 0.05 \exp\left(\frac{165000}{RT}\right), \quad (10)$$

$$\frac{D_{\text{Ni,Disl}}}{D_{\text{Ni,Bulk}}} = 0.17 \exp\left(\frac{116000}{RT}\right). \quad (11)$$

#### 4. Summary

The lattice self-diffusion in equilibrated and defect poor metals is well understood and assessed. Diffusion generally follows the Arrhenius law with the key variables activation energy  $Q$  and frequency factor  $D_0$ . Nevertheless, the acceleration of diffusion kinetics along grain boundaries and dislocation pipes proves to be rather complex. Measurement conditions, such as purity, temperature range, used method, etc. differ greatly, and the scatter of the reported data is in the range of several orders of magnitude. In the present paper, we provide a least squares fit of diffusion values for  $Q$  and  $D_0$  based on the available literature. The results are reported in the form of absolute values for  $Q$  and  $D_0$  as well as the ratio of  $D_{\text{GB}}/D_{\text{Bulk}}$  and  $D_{\text{Disl}}/D_{\text{Bulk}}$ , respectively. The current analysis is performed over the whole temperature range, from melting point to room temperature.

#### Acknowledgment

Financial support by the Austrian Federal Government (in particular from the Bundesministerium für Verkehr, Innovation und Technologie and the Bundesministerium für Wirtschaft, Familie und Jugend) and the Styrian Provincial Government, represented by Österreichische Forschungsförderungsgesellschaft mbH and by Steirische Wirtschaftsförderungsgesellschaft mbH, within the research activities of the K2 Competence Centre on “Integrated Research in Materials,

Processing and Product Engineering”, operated by the Materials Center Leoben Forschung GmbH in the framework of the Austrian COMET Competence Centre Programme, is gratefully acknowledged.

## Literature

1. R. Radis, E. Kozeschnik, "Kinetics of AlN precipitation in microalloyed steel", *Model. Simul. Mater. Sci. Eng.*, 18 (2010) 1-16.
2. R. Radis, E. Kozeschnik, "Numerical simulation of NbC precipitation in microalloyed steel", *Model. Simul. Mater. Sci. Eng.*, 20 (2012) 1-15.
3. C.E. Campbell, A.L. Rukhin, "Evaluation of self-diffusion data using weighted means statistics", *Acta Mater.*, 59 (2011) 5194-5201.
4. B. Jönsson, "On Ferromagnetic Ordering and Lattice Diffusion – A Simple Model", *Z. Metallkd.*, 83 (1992) 349-355.
5. J. Fridberg, L.-E. Törndahl, M. Hillert, "Diffusion in iron", *Jernkont. Ann.*, 153 (1969) 263-276.
6. N.L. Peterson, "Grain-boundary diffusion in metals", *Int. Mater. Rev.*, 28 (1983) 65-91.
7. R.W. Balluffi, "Grain Boundary Diffusion Mechanisms in Metals", *Metall. Trans. A*, 13A (1982) 2069-2095.
8. N.A. Gjostein, "Diffusion", ASM, Metals Park, OH, 1973.
9. S.M. Klotsman, A.N. Timofeyev, I.Sh. Traktenberg, "Mechanism of diffusion via structural defects (dislocations and grain boundary regions) in metals", *Fiz. Metal. Metalloved.*, 23 (1967) 257-261.
10. S.-G. Hong, K.-O. Lee, S.-B. Lee, "Dynamic strain aging effect on the fatigue resistance of type 316L stainless steel", *Int. J. Fatigue*, 27 (2005) 1420-1424.
11. H. Mehrer, "Diffusion in solids", Springer-Verlag Berlin Heidelberg, New York, 2007.
12. J. Sommer, Chr. Herzig, "Direct determination of grain-boundary and dislocation self-diffusion coefficients in silver from experiments in type-C kinetics", *J. Appl. Phys.*, 72 (1992) 2758-2766.
13. S.V. Divinski, J. Geise, E. Rabkin, C. Herzig, "Grain boundary self-diffusion in  $\alpha$ -iron of different purity: effect of dislocation enhanced diffusion", *Z. Metallkd.*, 95 (2004) 945-952.
14. S.V. Divinski, B.S. Bokstein, "Recent Advances and Unsolved Problems of Grain Boundary Diffusion", *Defect Diffus. Forum*, 309-310 (2011) 1-8.
15. N.L. Peterson, "Self-diffusion in pure metals", *J. Nucl. Mater.*, 69&70 (1978) 3-37.
16. A. Seeger, "The mechanisms of diffusion in metals and alloys", *J. Less-Common Met.*, 28 (1972) 387-418.
17. W. Lange, M. Jurisch, quoted in Ref. 6.

18. A. Hässner, "Untersuchung der Korngrenzdifffusion von Zb-65 in  $\alpha$ -Aluminium-Zink-Legierungen", *Krist. Tech.*, 9 (1974) 1371-1388. In German.
19. J. Kwiecinski, J.W. Wyrzykowski, "Investigation of grain boundary self-diffusion at low temperatures in polycrystalline aluminium by means of the dislocation spreading method", *Acta Metall. Mater.*, 39 (1991) 1953-1958.
20. T.E. Volin, K.H. Lie, R.W. Balluffi, "Measurement of rapid mass transport along individual dislocations in aluminum", *Acta Metall.*, 19 (1971) 263-274.
21. E. Ronander, S. Kritzinger, "A quantitative study of anomalous annealing phenomena in quenched Aluminum", *J. Appl. Phys.*, 49 (1978) 3980-3986.
22. M.C. Shine, F.M.d'Heurle, "Activation Energy for Electromigration in Aluminum Films Alloyed with Copper", *IBM J. Res. Develop.*, 15 (1971) 378-383.
23. I. Kaur, W. Gust, "12 Grain and interphase boundary diffusion, in: Landolt-Börnstein - Group III Condensed Matter: Numerical Data and Functional Relationships in Science and Technology", Volume 26: Diffusion in Solid Metals and Alloys, SpringerMaterials, 2012.
24. C. Leymonie, Y. Adda, A. Kirianenko, P. Lacombe, "Nouvelle determination des constantes d'autodiffusion intergranulaire du fer cubique centré", *C.R. Acad. Sci. Paris*, 248 (1959) 1512-1515. In French.
25. C. Leymonie, *Thèse Paris* (1960).
26. V.T. Borisov, V.M. Golikov, G.V. Scherbedinskiy, "Relation between diffusion coefficients and grain boundary energy", *Fiz. Metal. Metalloved.*, 17 (1964) 80-85.
27. D.W. James, G.M. Leak, "Grain Boundary Diffusion of Iron, Cobalt and Nickel in Alpha-iron and of Iron in Gamma-iron", *Philos. Mag.*, 12 (1965) 491-503.
28. J. Bernardini, P. Gas, E.D. Hondros, M.P. Seah, "The Role of Solute Segregation in Grain Boundary Diffusion", *Proc. R. Soc. Lond. A*, 379 (1982) 159-178.
29. H. Hänsel, L. Stratmann, H. Keller, H.J. Grabke, "Effects of the grain boundary segregants P, S, C and N on the grain boundary self-diffusivity in  $\alpha$ -iron", *Acta Metall.*, 33 (1985) 659-665.
30. H. Tanimoto, P. Farber, R. Würschum, R.Z. Valiev, H.-E. Schaefer, "Self-diffusion in high-density nanocrystalline Fe", *Nanostruct. Mater.*, 12 (1999) 681-684.
31. A. Inoue, H. Nitta, Y. Iijima, "Grain boundary self-diffusion in high purity iron", *Acta Mater.*, 55 (2007) 5910-5916.

32. H. Schmidt, S. Chakravarty, M. Jiang, E. Hüger, P.K. Parida, T. Geue, J. Stahn, U. Tietze, D.Lott, "Grain boundary self-diffusion in Fe films with a stable nanostructure", *J. Mater. Sci.*, 47 (2012) 4087-4092.
33. H. Mehrer, M. Lübbehusen, "Self-diffusion along dislocations and in the lattice of alpha-iron", *Defect Diffus. Forum*, 66-69 (1989) 591-604.
34. Y. Shima, Y. Ishikawa, H. Nitta, Y. Yamazaki, K. Mimura, M. Isshiki, Y. Iijima, "Self-Diffusion along Dislocations in Ultra High Purity Iron", *Mater. Trans.*, 43 (2002) 173-177.
35. S.V. Divinski, G. Reglitz, G. Wilde, "Grain boundary self-diffusion in polycrystalline nickel of different purity levels", *Acta Mater.*, 58 (2010) 386-395.
36. D. Prokoshkina, V. A. Esin, G. Wilde, S. V. Divinski, "Grain boundary width, energy and self-diffusion in nickel: Effect of material purity", *Acta Mater.*, 61 (2013) 5188-5197.
37. T. Surholt, C. Herzig, "Grain boundary self-diffusion in Cu polycrystals of different purity", *Acta Mater.*, 45 (1997) 3817-3823.
38. G. Stechauner, E. Kozeschnik, "Self-Diffusion in Grain Boundaries and Dislocation Pipes in Al, Fe, and Ni and Application to AlN Precipitation in Steel", *J. Mater. Eng. Perform.*, 23 (2014) 1576-1579.
39. S.Z. Bokstein, S.T. Kishkin, S.T. Moroz, "The effect of metal composition structure on the diffusion of components along grain boundaries", *Appl. Radiat. Isotopes*, 2 (1957) 253.
40. C. Leymonie, P. Lacombe, "Mesure de l'énergie d'activation d'autodiffusion Intergranulaire du fer", *Mem. Sci. Rev. Met.*, 56 (1959) 74-80. In French.
41. W. Lange, A. Hässner, G. Mischer, "Messung der Korngrenzdifffusion von Nickel-63 in Nickel und  $\gamma$ -Eisen", *Phys. Stat. Sol.*, 5 (1964) 63-71. In German.
42. D. Bergner, *Dissertation Bergakademie Freiberg* (1964); quoted in Ref. 18.
43. P. Guiraldenq, P. Lacombe, "Mesure des coefficients d'autodiffusion intergranulaire du fer en phase  $\gamma$  et comparaison avec l'autodiffusion aux joints de grains du fer  $\alpha$ ", *Acta Metall.*, 13 (1965) 51-53. In French.
44. W.R. Upthegrove, M.J. Sinnott, "Grain boundary self-diffusion of nickel", *T. Am. Soc. Metal.*, 50 (1958) 1031-1046.
45. S.D. Gerzriken, T.J. Jatsenko, *Sbornik Naucnych Rabot Inst. Metallofiz., Akad. Nauk Ukr.SSR*, 12 (1961) 135-141. In Russian.
46. A.R. Wazzan, "Lattice and Grain Boundary Self-Diffusion in Nickel", *J. Appl. Phys.*, 36 (1965) 3596-3599.

47. W. Assassa, P. Guiraldenq, "Influence du silicium sur l'autodiffusion en volume et intergranulaire du nickel dans des alliages nickel-silicium", *C. R. Acad. Sc. Paris*, 279 (1974) 59-62. In French.
48. N.W. deReca, C.A. Pampillo, "Grain boundary diffusivity via bulk diffusion measurements during grain growth", *Scripta Metall. Mater.*, 9 (1975) 1355-1361.
49. S.S. Bokstein, S.T. Kischkin, Y.M. Mishin, I.M. Razumovskii, *Dokl. Akad. Nauk SSSR*, 280 (1985) 1125-1128. In Russian.
50. P. Neuhaus, C. Herzig, "The Temperature Dependence of Grain Boundary Self Diffusion in Nickel", *Z. Metallkd.*, 79 (1988) 595-599.
51. M.I. Mendeleev, H. Zhang, D.J. Srolovitz, "Grain boundary selfdiffusion in Ni: Effect of boundary inclination", *J. Mater. Res.*, 20 (2005) 1146-1153.
52. V. Rothova, J. Bursik, M. Svoboda, J. Cermak, "Grain Boundary Self-Diffusion in Nickel", *Defect Diffus. Forum*, 263 (2007) 207-212.
53. M. Wuttig, H.K. Birnbaum, "Self-Diffusion along Edge Dislocations in Nickel", *Phys. Rev.*, 147 (1966) 495-504.
54. R.F. Canon, J.P. Stark, "Grain Boundary Self-Diffusion in Nickel", *J. Appl. Phys.*, 40 (1969) 4366-4373.
55. J. Cermak, Z. Cochnar, "Self-diffusion of  $^{63}\text{Ni}$  along dislocations", *Mater. Sci. Eng.*, 174 (1994) 9-13.

# Paper three

Simulation of Cu Precipitation in the Fe-Cu Binary System

Georg Stechauner and Ernst Kozeschnik

Advanced Materials Research

Volume 922, Year 2014, pages 728-733.

# Simulation of Cu precipitation in the Fe-Cu binary system

Georg Stechauner<sup>1,2,\*</sup>, Ernst Kozeschnik<sup>1,3</sup>

<sup>1</sup>Institute of Materials Science and Technology, Vienna University of Technology, Austria

<sup>2</sup>Materials Center Leoben Forschungsgesellschaft mbH, Leoben, Austria

<sup>3</sup>Christian Doppler Laboratory for Early Stages of Precipitation, Institute of Materials Science and Technology, Vienna University of Technology, Austria.

Email: georg.stechauner@tuwien.ac.at, ernst.kozeschnik@tuwien.ac.at

## Keywords

Fe-Cu precipitation, simulation, transformation, interface energy, coalescence

## Abstract

Cu precipitation in steel has been investigated numerous times. Still, a consistent simulation of the nucleation, growth and coarsening kinetics of Cu precipitates is lacking. Major reason for this is the fact that Cu precipitation involves complex physical interactions and mechanisms, which go beyond the classical precipitation models based on evaporation and absorption of precipitate-forming monomers (atoms). In the present work, we attempt a comprehensive modeling approach, incorporating coalescence results from Monte Carlo simulation, prediction of the nucleus composition based on the minimum energy barrier concept, diffusion enhancement from quenched-in vacancies, dislocation pipe diffusion, as well as the transformation sequence of Cu-precipitates from bcc-9R-fcc. Our simulations of number density, radius and phase fraction coincide well with experimental values. The results are consistent over a large temperature range, which is demonstrated in a TTP-plot.

## 1. Introduction

Cu precipitation kinetics in ferritic steel has been studied by means of experimental as well as numerical studies many time, e.g. [1-4]. It is generally accepted that Cu precipitates nucleate in body centred cubic (bcc) crystal structure and undergo a transformation via the semi-coherent 9R structure to incoherent face centred cubic (fcc) structure [5]. Precipitates with a radius below 2.5 nm [1,2] to 4 nm [6] are assumed to be fully coherent. Larger precipitates gradually lose coherency and finally transform into fcc. This loss of coherency is accompanied by a compositional change of the Cu precipitates from Fe-rich nuclei in the early stages to almost pure Cu in incoherent stages.

Computer simulation of this complex precipitation reaction demands the consideration of several mechanisms, which exceed the standard framework of conventional simulation packages. Only

after implementation of these mechanisms into the simulation, a consistent description of the precipitation problem in Fe-Cu is possible.

The present simulation approach is applied to an Fe-1.4 wt.% Cu alloy, which was investigated experimentally by Perez et al. [7]. The simulation results are visualized in a ttp-plot in the range between 400°C to 700°C with the 10 and 90 percent precipitation lines. A comparison with available experimental data shows a consistent reproduction over the whole temperature range.

## 2. Simulation of Cu-precipitation in ferritic steel

The numerical simulations are carried out with the software MatCalc [8-11], using the thermodynamic database mc\_fe\_v2.000.tdb [12], and the diffusion data of Fridberg et al. [13]. Diffusion enhancement on short-circuit diffusion-paths is considered as proposed in ref. [14].

### 2.1 The numerical model

The numerical model utilized in following simulations is based on Classical Nucleation Theory (CNT) [15]. The number of newly formed precipitates per unit volume and time is given by the time-dependent nucleation rate  $J$  as

$$J = N_0 Z S^* \cdot \exp\left(\frac{-G^*}{k \cdot T}\right) \cdot \exp\left(\frac{-\tau}{t}\right), \quad (1)$$

where  $N_0$  represents the total number of potential nucleation sites,  $Z$  is the Zeldovich factor,  $\beta$  is the atomic attachment rate,  $G^*$  is the critical nucleation energy,  $k$  is the Boltzmann constant,  $T$  is the temperature,  $\tau$  is the incubation time and  $t$  is time. The critical nucleation energy  $G^*$  is

$$G^* = \frac{16f}{3} \frac{\chi^3}{U G_{\text{vol}}^2}, \quad (2)$$

where  $G_{\text{vol}}$  is the volume free energy change and  $\gamma$  is the effective energy of the precipitate / matrix interface.

After nucleation, further growth is described with the evolution equations for multi-component multi-phase precipitation derived in ref. [9] and based on the numerical integration scheme described in ref. [10]. Even though this approach was successfully used for other complex precipitation reactions, see e.g. [16-19], in the Fe-Cu system, several additional mechanisms have to be

considered. In the present paper, the conventional treatment is advanced by consideration of the following effects:

- (i) nucleation with variable precipitate composition according to minimum  $G^*$ ,
- (ii) size correction for the interfacial energy due to curvature as proposed in ref. [20],
- (iii) entropic corrections for the interfacial energy due to mixing of atoms along the matrix / precipitate interface at elevated temperatures as proposed in ref. [21],
- (iv) coalescence and acceleration of Cu cluster mobility,
- (v) consideration of three nucleation populations to reproduce the structural transformation evolution from bcc-9R-fcc.

In the following, these effects are discussed in the context of the present simulations.

(i) Nucleus composition: Investigating eq. (1) more thoroughly, one can see that almost all input quantities are uniquely determined. More information on the corresponding equations can be found, for instance, in refs. [22,23]. The only unknown is the chemical composition of the precipitate nucleus. This undefined degree of freedom must be fixed by some assumption or hypothesis. In conventional precipitation kinetics simulations, the nucleus composition is often assumed to be in the ortho-equilibrium state, which corresponds to the state with maximum chemical driving force. However, especially at lower temperatures, this condition is unrealistic and cannot be reached in many instances. Here, the ortho-nucleus would consist of almost pure Cu with a small solubility for Fe.

When investigating eq. (2), we observe that the critical nucleation energy depends on the cube of the interfacial energy and inversely quadratically on the driving force. The interfacial energy itself is strongly affected by the nucleus composition as it is approximately a quadratic function of the composition difference between precipitate and matrix. With  $G^*$  in the exponent of the nucleation rate expression, it appears plausible to assume that the nucleation event occurs with highest probability at a composition, which yields the lowest nucleation energy  $G^*$ . This criterion is adopted in the present simulations.

(ii)-(iii) Interfacial energy calculation: The energy of the planar sharp bcc and fcc precipitate / matrix interfaces ( $\gamma_0$ ) is a most essential input parameter in precipitation kinetics simulations. In the present study, it is calculated from the generalized broken-bond (GBB) model [24] (Fig. 1). As shown in the

figure, the interfacial energy  $\gamma_0$  for bcc-Fe is strongly influenced by the ferromagnetic ordering of the matrix.  $\gamma_0$  cannot be used directly and must be further processed into the *effective* interfacial energy  $\gamma$  by considering two effects. These are the size of the precipitate, having an effect on the interfacial curvature, and atomic mixing across the precipitate / matrix interface. The size effect on the interfacial energy is taken into account by a radius-dependent correction factor as derived in ref. [20]. The atomic mixing process is considered on basis of the corresponding diffuse interface energy model [21]. The critical temperature  $T_c$  in this model is evaluated by investigating the miscibility gap in the Fe-Cu system at a composition of  $X_{Cu}=0.5$ . A value of 1860K is observed. The effective interfacial energy as used in the present simulations is the result of the planar, sharp interface multiplied with the diffuse interface correction and consideration of the size effect (Fig. 1).

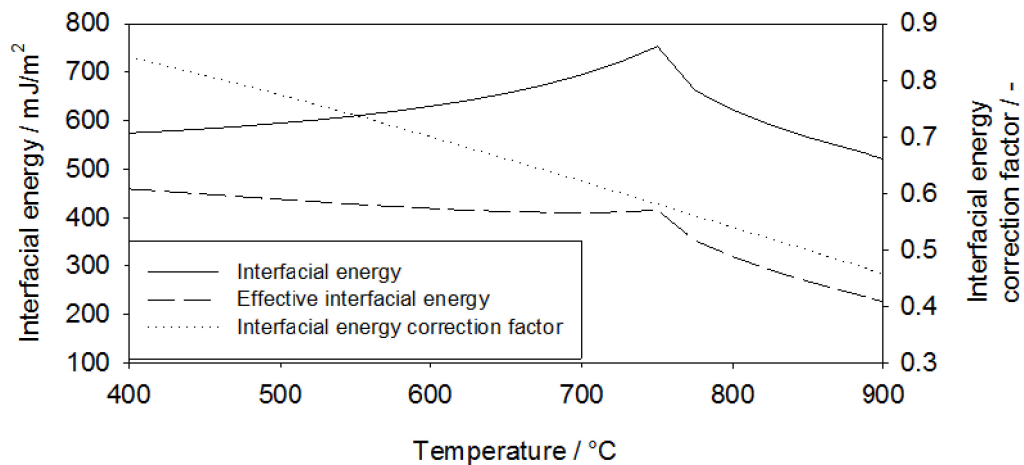


Figure 1 - Planar, sharp interface energy  $\gamma_0$  of equilibrium bcc Cu precipitates calculated from the GBB model with diffuse interface correction.

(iv) Coalescence of particles: In recent work, Warczok et al. [25] demonstrated, on basis of atomistic and continuums modeling of cluster migration, a strong tendency of Cu particles for coalescence. After implementing the Binder-Staufffer kinetics [25], which governs the cluster migration rate with a coefficient between  $-4/3$  to  $-3/4$ , it was possible to simulate phase fraction, radius and number density evolution in a consistent way and in accordance with experiment. The high mobility of Cu clusters compared to Cu-monomers was also investigated by Jourdan [26]. An acceleration of cluster diffusion of two orders of magnitude was found compared to monomers. This effect is implemented by definition of a general diffusion enhancement with a factor of 100.

(v) Semi- and Incoherent Cu-precipitates: Finally, the experimentally observed loss of coherency of Cu-precipitates when transforming from bcc via 9R to fcc crystal structure [1,5,6,27] is taken into account by considering a radius-dependent transformation model. When both precipitate types (bcc and fcc) are treated simultaneously and in competition, faster precipitation of the coherent metastable bcc phase with lower Cu content and, thus, lower interfacial energy is observed. With time, the precipitates grow and undergo a structural transformation: between 2-3nm radius, the bcc precipitates transform to the 9R structure and, subsequently, between 4-8nm transform to incoherent fcc precipitates. Consistent with experimental results, the final constitution consists of solely fcc particles.

### 3. Results and Discussion

In this section, the present simulation method is utilized to simulate experimental data of number density  $N$ , mean radius  $r$  and phase fraction  $f$  from ref. [1] as well as to determine the 10% and 90% precipitation lines for the Fe-1.4 wt.% Cu alloy as investigated in ref. [7]. A series of simulated plots is presented, incorporating the previously discussed effects (i)-(v). All plots are compared to the reported experimental data.

The precipitation of Cu in a Fe-1.4 at.% Cu alloy at 500°C was investigated by Goodman [1], providing us with important data-triplets of  $N$ ,  $r$  and  $f$ . The simulation is carried out as an isothermal treatment at 500°C. Figure 2 shows the results, which are split into (a)-(c) for easier interpretation. The simulation is run until a constant phase fraction is reached. With the correct evolution of all three Cu precipitation parameters from early stages to coarsening, this methodology is applied to the calculation of the ttp-plot for Cu-precipitation from ferrite.

To generate the ttp-plots, the relative phase fractions of the cumulative curve are evaluated from isothermal kinetic simulations carried out with MatCalc in 25K steps between 400°C and 700°C. Figure 3 shows the ttp-plots for the different simulation steps, starting with the simulation for ortho-equilibrium nuclei (Fig. 3 (a)). Stepwise, the impact of the variable nucleus composition (Fig. 3 (b)) together with the effects of precipitate size and atomic mixing across the interface (Fig. 3 (c)) and, finally, coalescence (Fig. 3 (d)) are taken into account. This is discussed in more detail subsequently. In the evaluation of the times for 10% and 90% ttp-lines, the maximum precipitated phase fraction of each considered temperature was used as reference.

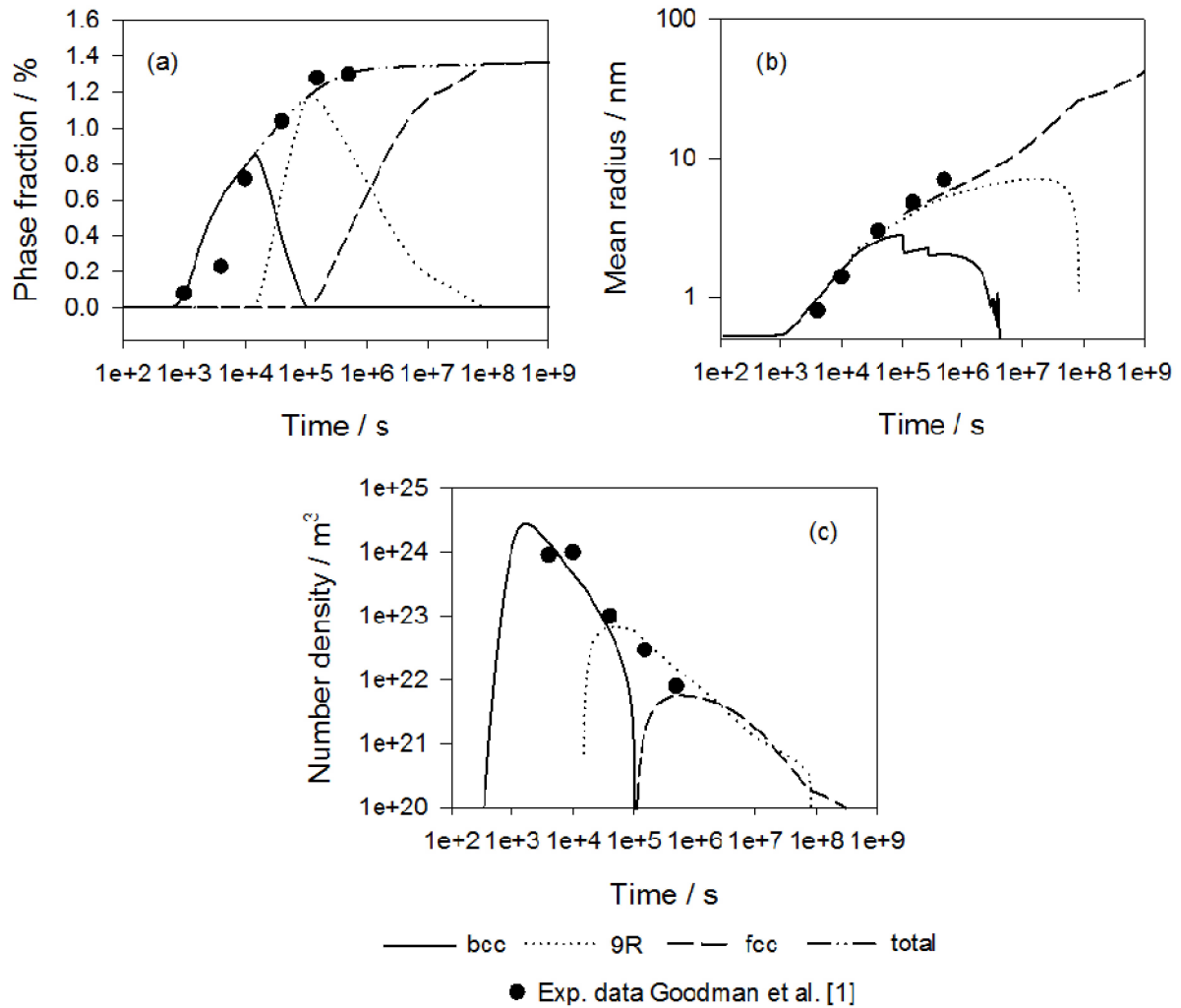


Figure 2 - Results of the kinetic simulation for Fe-1.4 wt.% Cu alloy investigated by Goodman [1]. (a)-(c) show the phase fraction  $f$ , mean radius  $r$  and number density  $N$  of the three considered populations bcc, 9R and fcc. All effects (i) to (v) were considered.

In Fig. 3 (a), the precipitate fractions are evaluated numerically using the assumption of a maximum chemical nucleation driving force, which corresponds to the assumption of ortho-equilibrium composition for the precipitate nucleus [22,23]. No further assumptions are made and the evaluation routines in MatCalc are utilized as developed originally in refs. [9-11] and without any undetermined fitting parameter. The agreement of simulation and experiment in this case is poor. The precipitation start times are orders of magnitude too late and the maximum precipitation temperature is evaluated too low by values of more than 100K.

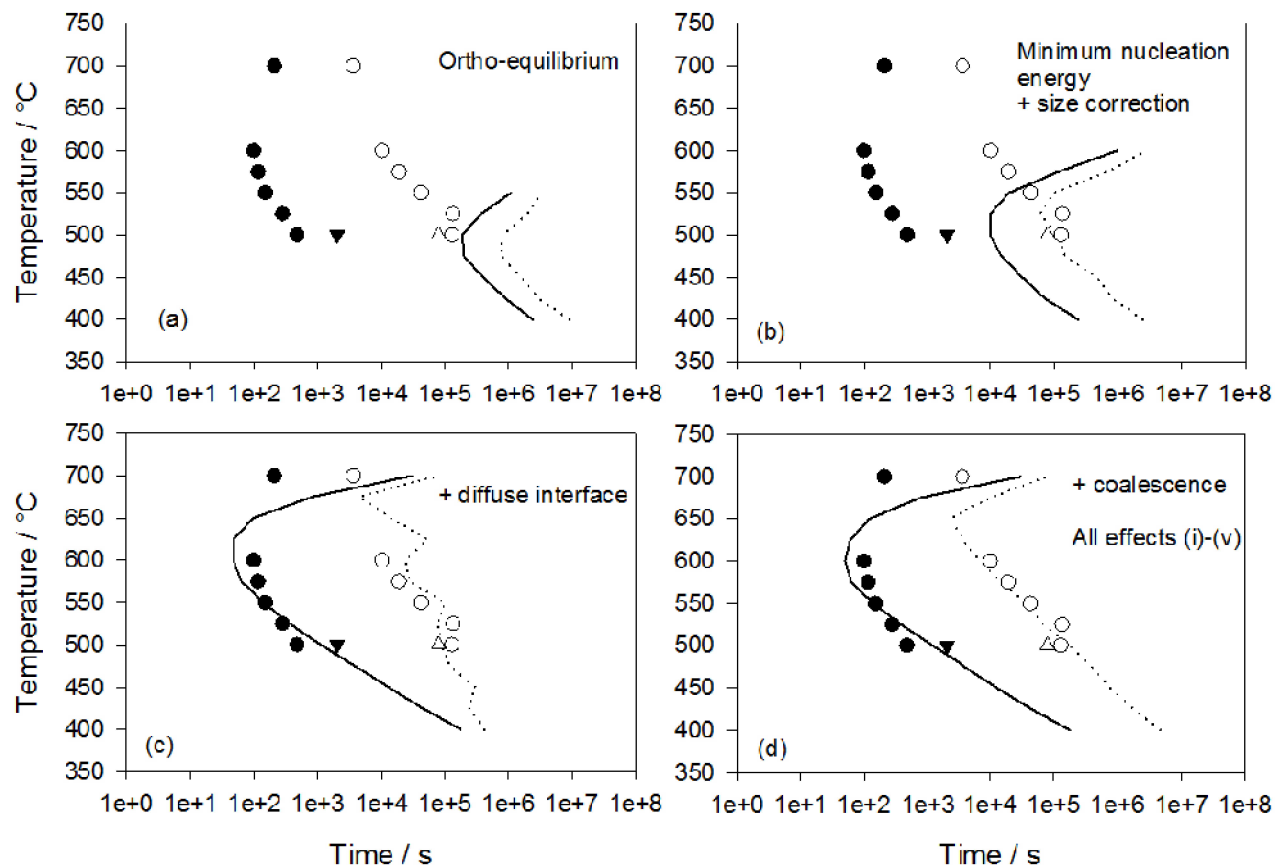


Figure 3 (a)-(d). Calculated ttp-plots for 10% and 90% Cu-precipitation compared with the experimental data referred in [1] triangles and [7] circles, with (a) ortho-equilibrium nucleus composition, (b) minimum  $G^*$  nucleus composition and precipitate size effect, (c) entropic effect of mixing at interface and (d) coalescence and, therefore, all different effects (i)-(v).

In Fig. 3 (b), the simulation is adapted such as to take into account the compositional variations of the Cu nuclei as well as the precipitate size effect. Even though precipitation start times occur an order of magnitude earlier, the process is still too slow, and the evaluated temperatures are also still off by about 100K. In Fig. 3 (c), the entropic effect of mixing at the interface is considered. Compared to the prior results, the precipitation start times are considerably shorter and in good qualitative and quantitative agreement with experimental evidence. Especially, the 10% line closely matches the experimental data.

Fig. 3 (d) finally incorporates all effects, comparable to the detailed simulation results of Fig. 2. With all mechanisms, excellent agreement between simulation and experiment in the entire temperature range can be achieved. Moreover, not only the phase fraction lines shown in Fig. 3 (d) are simulated correctly, but all three precipitation parameters, phase fraction, mean radius as well as number density, are consistently reproduced. The main difference between plot (c) and (d) is the

correct treatment of growth and coarsening of bcc-precipitates due to the consideration of particle coalescence.

#### 4. Summary

An advanced simulation approach is developed for the numerical simulation of Cu-precipitation in ferritic steel, taking into account the major mechanisms affecting the precipitation kinetics in Cu-alloyed ferritic steels. These are the varying nucleus composition, the transformation sequence from coherent bcc-Cu to incoherent fcc-Cu, the interfacial energy size correction due to the curvature of small particles and the temperature-dependent reduction of the interfacial energy of the coherent bcc Cu precipitates due to diffuse interfaces as well as the coalescence and high cluster mobility of Cu-particles. With these model ingredients, the experimental ttp-data for Fe-1.4wt.% Cu is reproduced consistently and in a predictive manner.

#### Acknowledgement

Financial support by the Austrian Federal Government (in particular from Bundesministerium für Verkehr, Innovation und Technologie and Bundesministerium für Wirtschaft, Familie und Jugend) represented by Österreichische Forschungsförderungsgesellschaft mbH and the Styrian and the Tyrolean Provincial Government, represented by Steirische Wirtschaftsförderungsgesellschaft mbH and Standortagentur Tirol, within the framework of the COMET Funding Programme is gratefully acknowledged.

#### References

1. S.R. Goodman, S.S. Brenner, J.R. Low, Jr., "An FIM-Atom Probe Study of the Precipitation of Copper from Iron-1.4 At. Pct Copper. Part I: Field-Ion Microscopy", *Metall. Trans.*, 4 (1973) 2363-2369.
2. S.R. Goodman, S.S. Brenner, J.R. Low, Jr., "An FIM-Atom Probe Study of the Precipitation of Copper from Iron-1.4 At. Pct Copper. Part II: Atom Probe Analyses", *Metall. Trans.*, 4 (1973) 2371-2378.
3. M.E. Fine, J.Z. Liu, M.D. Asta, "An unsolved mystery: The composition of bcc Cu alloy precipitates in bcc Fe and steels", *Mat. Sci. Eng. A*, 463 (2007) 271-274.
4. E. Kozeschnik, "Thermodynamic prediction of the equilibrium chemical composition of critical nuclei: Bcc Cu precipitation in  $\alpha$ -Fe", *Scripta Mater.*, 59 (2008) 1018-1021.

5. P.J. Othen, M.L. Jenkins, G.D.W. Smith, "High-resolution electron microscopy studies of the structure of Cu precipitates in alpha-Fe", *Phil. Mag. Lett.*, 70 (1994) 1-24.
6. Y. Le Buoar, "Atomistic study of the coherency loss during the BCC-9R transformation of small copper precipitates in ferritic steels", *Acta Mater.*, 49 (2001) 2661-2669.
7. M. Perez, F. Perrard, V. Massardier, X. Kleber, V. Schmitt, A. Deschamps, "Low Temperature Solubility Limit of Copper in Iron", *Mater. Sci. Forum*, 500-501 (2005) 631-638.
8. E. Kozeschnik, B. Buchmayr, in: H. Cerjak, H.K.D.H. Bhadeshia (Eds.), *Mathematical Modelling of Weld Phenomena*, 2001, IOM Communications Ltd, London 349-361.
9. J. Svoboda, F.D. Fischer, P. Fratzl, E. Kozeschnik, "Modelling of kinetics in multi-component multi-phase systems with spherical precipitates I – theory", *Mater. Sci. Eng. A*, 385 (2004) 166-174.
10. E. Kozeschnik, J. Svoboda, P. Fratzl, F.D. Fischer, "Modelling of kinetics in multi-component multi-phase systems with spherical precipitates II – numerical solution and application", *Mater. Sci. Eng. A*, 385 (2004) 157-165.
11. E. Kozeschnik, J. Svoboda, F.D. Fischer, "Modified evolution equations for the precipitation kinetics of complex phases in multi-component systems", *CALPHAD*, 28 (2004) 379-382.
12. E. Povoden-Karadeniz, *Thermodynamic database mc\_fe\_v2.000.tdb*, Vienna University of Technology, 2013.
13. J. Fridberg, L.E. Törndahl, M. Hillert, "Diffusion in Iron", *Jernkontorets Ann.*, 153 (1969) 263-276.
14. G. Stechauner, E. Kozeschnik, "Assessment of substitutional self-diffusion along short-circuit paths in Al, Fe and Ni", *CALPHAD*, 47 (2014) 92-99.
15. K.C. Russell, "Nucleation in solids: the induction and steady state effects", *Adv. Colloid Interfac.*, 13 (1980) 205-318.
16. B. Sonderegger, E. Kozeschnik, H. Leitner, H. Clemens, J. Svoboda and F.D. Fischer, "Computational analysis of the precipitation kinetics in a complex tool steel", *Int. J. Mat. Res.*, 99 (2008) 410-415.
17. B. Sonderegger, E. Kozeschnik, H. Leitner, H. Clemens, J. Svoboda, F.D. Fischer and P. Staron, "Kinetics of Precipitation in a Complex Hot-work Tool Steel", *Steel Res. Int.*, 81 (2010) 64-73.
18. R. Radis and E. Kozeschnik, "Kinetics of AlN precipitation in microalloyed steel", *Model. Simul. Mater. Sci. Eng.*, 18 (2010) 055003 (16pp).

19. R. Radis and E. Kozeschnik, "Numerical simulation of NbC precipitation in microalloyed steel", *Model. Sim. Mater. Sci. Eng.*, 20 (2012) 055010 (15pp).
20. B. Sonderegger, E. Kozeschnik, "Size dependence of the interfacial energy in the generalized nearest-neighbor broken-bond approach", *Scripta Mater.*, 60 (2009) 635-638.
21. B. Sonderegger, E. Kozeschnik, "Interfacial Energy of Diffuse Phase Boundaries in the Generalized Broken-Bond Approach", *Metall. Mater. Trans. A*, 41 (2010) 3262-3269.
22. E. Kozeschnik, J. Svoboda, F.D. Fischer, in Proc. Int. Conference Solid-Solid Phase Transformations in Inorganic Materials, PTM 2005, Phoenix, AZ, USA, 2005, 301-310.
23. "Computational Materials Engineering - An Introduction to Computational Microstructure Evolution of Polycrystalline Materials", K.G.F. Janssens, D. Raabe, E. Kozeschnik, M.A. Miodownik, B. Nestler, Elsevier Publishing, ISBN 978-0-12-369468-3, 2007.
24. B. Sonderegger, E. Kozeschnik, "Generalized Nearest-Neighbor Broken-Bond Analysis of Randomly Oriented Coherent Interfaces in Multicomponent Fcc and Bcc Structures", *Metall. Mater. Trans. A*, 40 (2009) 499-510.
25. P. Warczok, J. Zenisek, E. Kozeschnik, "Atomistic and continuums modeling of cluster migration and coagulation in precipitation reactions", *Comp. Mater. Sci.*, 60 (2012) 59-65.
26. T. Jourdan, J.-L. Bocquet, F. Soisson, "Modeling homogeneous precipitation with an event-based Monte Carlo method: Application to the case of Fe-Cu", *Acta Mater.*, 58 (2010) 3295-3302.
27. T. Nagano, M. Enomoto, "Simulation of the growth of copper critical nucleus in dilute bcc Fe-Cu alloys", *Scripta Mater.*, 55 (2006) 223-226.

# Paper four

Thermo-Kinetic Modeling of Cu Precipitation in  $\alpha$ -Fe

Georg Stechauner and Ernst Kozeschnik

Acta Materialia

Volume 100, Year 2015, pages 135-146.

# Thermo-kinetic modeling of Cu precipitation in $\gamma$ -Fe

G. Stechauner<sup>a,\*</sup> and E. Kozeschnik<sup>b</sup>

<sup>a</sup> Materials Center Leoben Forschung GmbH, Leoben, Austria

<sup>b</sup> Christian Doppler Laboratory for „Early Stages of Precipitation“, Institute of Materials Science and Technology, Vienna University of Technology, Austria

\*Corresponding author: georg.stechauner@tuwien.ac.at

Georg Stechauner

Getreidemarkt 9 / E308

1060 Wien

Austria

+43 1 58801-30847

## Abstract

Consistent and predictive simulation of precipitation in the Fe-Cu system is a complex task. So far, no comprehensive approach is reported in literature that is capable of reproducing simultaneously all fundamental precipitation parameters (phase fraction, mean radius and number density) within a single set of model parameters and over an extended range of temperatures. In the present paper, we address this problem and present a novel approach for simulation of Cu-precipitation based on CALPHAD-type Gibbs energies, a mean-field model for precipitate growth, advanced classical nucleation theory and a predictive model for interface energy calculation. For successful simulation, several physical mechanisms are accounted for in addition to conventional Kampmann-Wagner-based precipitation modeling to achieve a consistent evolution of precipitation parameters. These comprise of models for the transition from bcc to 9R to fcc structure, curvature and temperature effects on interfacial energy, particle coalescence as well as a thermodynamic reassessment of the Fe-Cu system. We compare our results with experimental data as well as first-principles calculations from literature and, finally, predict a time-temperature-precipitation (TTP) diagram that reproduces the experimental one well within the experimental scatter.

## Keywords

Thermo-kinetic simulation, continuums-based modelling, Fe-Cu precipitation, thermodynamic assessment

## 1. Introduction

Precipitation of Cu-particles in binary Fe-Cu has been studied numerous times and with a multitude of experimental and simulation techniques since it attracts both, technological as well as academic, interest. Cu alloyed steel grades are often used for pressure vessels in irradiated environments [1] as well as structural or naval application [2], with the Cu-precipitates playing a major role in materials strengthening. The growth evolution of Cu precipitates is linked to various mechanical properties, such as embrittlement, and it is of utmost importance, for both safety reasons and plant life extension. Cu precipitates are further found as the main strengthening element in maraging steels of 17-4 PH grade [3]. By controlling the nucleation and growth of the particles with proper heat treatments, the hardness and strength can be adjusted to desired values. From the academic point of view, binary Fe-Cu offers a broad spectrum of challenges. Effects, such as transformation of crystal structure, variable nucleus composition, coalescence of Cu particles, ferro-magnetic transition and effects attributed to strong Cu-Vacancy binding have to be considered. Extensive work is available on the structural transformation sequence from bcc to martensitic 9R / 3R to fcc [4-6]. An assessment of strengths and weaknesses of different experimental methods is discussed by Lozano-Perez et al. [7].

A vast amount of literature is also available addressing the simulation of precipitate formation in the Fe-Cu system. The different approaches can be categorized according to the length scale / precipitate sizes that they potentially cover. The earliest stages are commonly described by Monte-Carlo (MC) [8-14] and first-principles studies [15-17], techniques that potentially shed light on the questions of nucleus compositions, binding energies and the vacancy-mediated diffusion mechanism. More sophisticated approaches, such as the event-based kinetic MC [11], can also reproduce the precipitate evolution considerably well. Although these methods have the capability of delivering essential information on the physical mechanisms governing Cu-precipitation, their application is generally limited to the early stages of precipitation due to significant computational cost with increasing simulation domain size.

On a larger length and time scale, classical nucleation and growth theory have been utilized [1,18-24] to predict the evolution of phase fractions, radii and number densities in a continuum-mechanical framework. These models generally deliver results with small to medium computational effort, having no limitation in simulation box size and, therefore, are capable of describing the entire evolution of precipitate populations from nucleation to coarsening.

With these continuum-based precipitation modeling approaches, the reproduction of one of the three precipitation parameters [12,20,21], e.g., the phase fraction, or two precipitation parameters

[1,23], e.g., phase fraction and mean radius or phase fraction and number density, succeeds considerably well. However, reproducing the corresponding third, dependent precipitation parameter at the same time introduces significant difficulties and, often, lack of consistency. As a consequence, in some of these approaches, diffusion rates or interfacial energies are introduced, which differ greatly from independently assessed values for these quantities in order to achieve a satisfactory reproduction of the available experimental data. This issue is discussed later in the present publication. Coarsening is often looked into separately [25-27] and it is commonly described in the framework of Lifshitz-Slyozov-Wagner (LSW) theory [28,29].

In the present work, we introduce a comprehensive and consistent model for simulation of the precipitation kinetics in the Fe-Cu system, which goes beyond the traditional precipitation modeling approaches. We describe the fundamental mechanisms that are incorporated in this approach, outline the impact of each of these mechanisms on the simulation results and present a reassessment of the Fe-Cu thermodynamics to be consistent also with experimental data on the composition-dependence of the magnetic properties.

## 2. Conventional size class-based simulation of precipitation

The numerical simulations carried out in this paper are performed with the software package MatCalc [30,31], version 5.62.1001, where all models described subsequently have been implemented in recent years. We start with a brief review of the nucleation and growth models that are commonly used together in the size class-based numerical Kampmann-Wagner approach [32]. We will denote these in the following as the ‘conventional’ approach to precipitation modeling. Some of the corresponding features have been summarized, e.g., in the work of Perez et al. [18], Robson [33] and Radis et al. [34].

### 2.1 Diffusion-controlled nucleation and growth models

Nucleation is a stochastic process driven by microscopic thermal and compositional fluctuations. It is commonly described within the framework of classical nucleation theory (CNT) [35,36] with

$$J = N_0 Z S^* \exp\left(\frac{-G^*}{k_b T}\right) \exp\left(\frac{-\ddagger}{t}\right), \quad (1)$$

where  $J$  represents the nucleation rate, describing the number of nuclei of the new phase created per unit volume and time,  $N_0$  is the density of potential nucleation sites,  $k_b$  is the Boltzmann constant,  $T$  is temperature and  $t$  is time.  $Z$  denotes the Zeldovich factor, which takes into account the destabilization of the critical nucleus by thermal excitation,  $S^*$  is the atomic attachment rate, which incorporates the

kinetics of diffusive transport of atoms to the critical nucleus and  $\dagger$  is the incubation time. The critical Gibbs energy for spherical nucleus formation  $G^*$  is

$$G^* = \frac{16f}{3} \frac{\chi^3}{\Delta G_{vol}^2}, \quad (2)$$

where  $\chi$  is the effective interfacial energy and  $\Delta G_{vol}$  is the volume free energy change on nucleus formation.

The growth of supercritical nuclei, which follows the nucleation process, is commonly described in a deterministic manner and it is controlled by the long-range diffusion of atoms towards the precipitates. The corresponding growth rates can be evaluated either from local-equilibrium based techniques [37,38] or using evolution equations for radius and composition of the precipitates as derived from the thermodynamic extremal principle [39,40]. Both approaches deliver a  $t^{1/2}$  dependency for the radius evolution. The latter approach is denoted as the SFFK model [30,31] and it is used in the present work. After depletion of the matrix from precipitate-forming elements, growth stops and coarsening starts, with smaller particles dissolving in favor of larger ones. The precipitate mean size evolution during coarsening generally follows a  $t^{1/3}$  dependency [28,29]. In the present approach, LSW-type coarsening controlled by long-range diffusion and atomic attachment and detachment is inherently incorporated in the numerical Kampmann-Wagner model implemented in MatCalc.

The three distinctive regions of precipitate evolution, nucleation, growth and coarsening, cannot always be clearly separated. Especially for low interface energies and high supersaturations, an overlap of even the nucleation and coarsening regimes can occur. A corresponding analysis has been reported by Robson [33].

## 2.2 Thermodynamic modeling

The present thermokinetic simulations in MatCalc utilize CALPHAD-type [41] Gibbs energies stored in the thermodynamic database “mc\_fe.tdb” [42]. From these data, chemical potentials, precipitation driving forces as well as interfacial energies are evaluated. In previous versions of this database, a linear dependence of the Curie temperature from chemical composition has been assumed as suggested by several researchers, such as, e.g., Turchanin et al. [43] or Shubhank and Kang [44]. However, experimental data from Sumiyama et al. [45] obtained on thin films of variable Fe/Cu ratio show an approximately parabolic dependency (see Fig. 1), which is fully considered in the present work. The new parameterization predicts a weaker dependence of the Curie temperature from the Cu content of the bcc Fe-Cu phase in accordance with experiment. The new data leads to significantly lower values of

the calculated interfacial energies particularly in the temperature region of the ferromagnetic to paramagnetic transition. Details on the new assessment are elaborated in Appendix A. The comparison of predicted planar sharp interfacial energies of the bcc and fcc Cu-precipitate/matrix interfaces are shown in Fig. 2. The interface energy calculation for 9R-Cu phase is based on the bcc thermodynamic data and, thus, identical to the values for the bcc precipitate. The approach for calculation of this quantity is described in the following section.

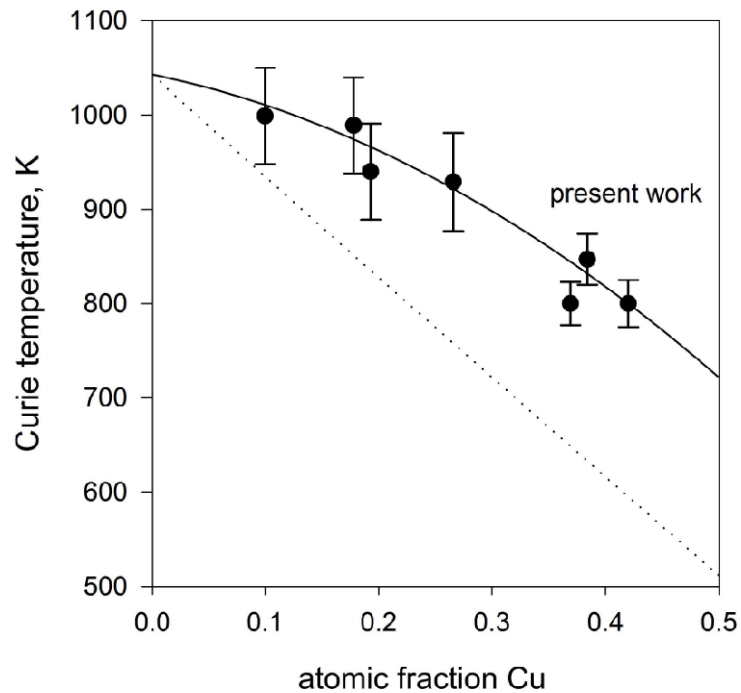


Figure 1 – Composition-dependent Curie temperature with previous approach (linear) and from present work (parabolic) in accordance with the experimental data of Sumiyama et al. [45].

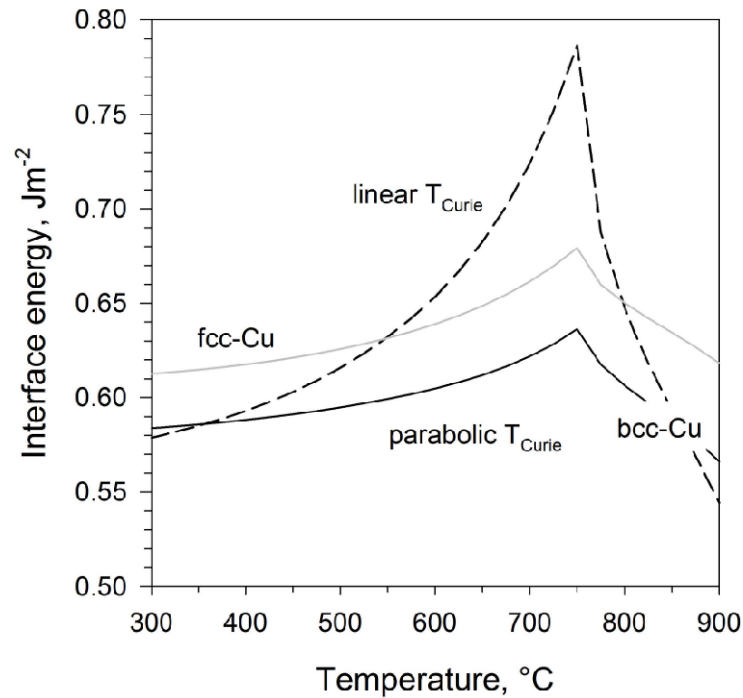


Figure 2 – Calculated planar sharp interface energy of bcc and fcc Cu precipitates in bcc Fe as a function of temperature. The predicted prominent peak at the Curie temperature is significantly weaker on basis of the present thermodynamic reassessment.

### 2.3 Interfacial energy modeling

The mean specific interfacial free energy,  $\gamma$ , is a most vital physical parameter for a predictive and quantitative modeling of nucleation. It appears in cubed form in the critical nucleation energy  $G^*$  (Eq. 2), which itself is in the exponent of the nucleation rate expression, (Eq. 1). As a consequence, even minimal changes in  $\gamma$  can lead to huge variations in  $J$ . Since the interfacial energy is not accessible to direct experimental measurement, this quantity is commonly used as a fitting parameter to adjust precipitation kinetics simulations to experimental data. Unfortunately, the values obtained by this procedure are heavily depending on the modeling approach itself that is used in the analysis and the reported interfacial energies for Cu-precipitates in  $\alpha$ -Fe, therefore, span ranges from 0.15 – 0.5 J/m<sup>2</sup> [10,15,27,46] for coherent interfaces, and 0.4 – 1.2 J/m<sup>2</sup> [27,46] for incoherent interfaces for even comparable precipitation boundary conditions.

Ardell [47] has developed a method for deriving interfacial energy values from independent measurement of diffusion coefficients and the evolution of supersaturation during coarsening experiments. Although delivering values with reasonable consistency in Ni-base alloys [48], for the present case of Cu-precipitation in Fe, his method is applicable to the later stages of precipitation, only, where the particles in the Fe-Cu system have already become incoherent to the surrounding matrix.

This technique is, therefore, not applicable here, since the prediction of nucleation rates in the coherent Fe-Cu system, representing the early stage precipitation system, is the key issue here.

As an alternative to experimental determination of interfacial energies from coarsening experiments, or evaluation of this quantity from fitting numerical simulation to early-stage precipitation experiments, Sonderegger and Kozeschnik [49] developed an analytical approach that predicts interfacial energies from knowledge of the thermodynamic properties of the alloy system (i.e., the enthalpy of solution) and a structural factor that accounts for the long-range effective broken bonds across the precipitate/matrix interface. In the extension of the classical nearest-neighbor broken-bond model to  $n$ -nearest neighbor interactions with  $n > 100$ , their model delivers energy values for planar sharp interfaces with good accuracy in even complex multi-component systems, see, e.g. [50,51]. It is further denoted as the generalized broken-bond (GBB) model and it describes the interfacial energy,  $\chi$ , as

$$\chi = \Gamma(r) \cdot S(T/T_c) \cdot \frac{n_s z_{s,eff}}{N_A z_{l,eff}} \cdot \Delta H_{sol}, \quad (3)$$

where  $n_s$  is the number of atoms per unit interfacial area,  $z_{s,eff}$  is the effective number of broken bonds across the interface,  $N_A$  is Avogadro's number and  $z_{l,eff}$  is the effective coordination number. These quantities have been evaluated in ref. [49].  $\Delta H_{sol}$  is the enthalpy of solution, which is obtained from the thermodynamic properties of the system as a function of temperature  $T$  and chemical composition of precipitate and matrix. The function  $\Gamma(r)$  takes into account the effect of curvature of the phase boundary introduced by the finite size of the nucleus. In previous simulations, we have utilized the methodology developed in ref. [52] on a routinely basis, which is why we consider this mechanism as integral part of the conventional approach to precipitation modeling. The size effect factor relating the planar to the spherical case, as applied in the present example, lies between 0.75 and 0.9, depending on the critical nucleation radius as a function of undercooling. The general shape of the size effect function is shown in Figure 3, with the typical critical radii observed in the present work marked as gray region.

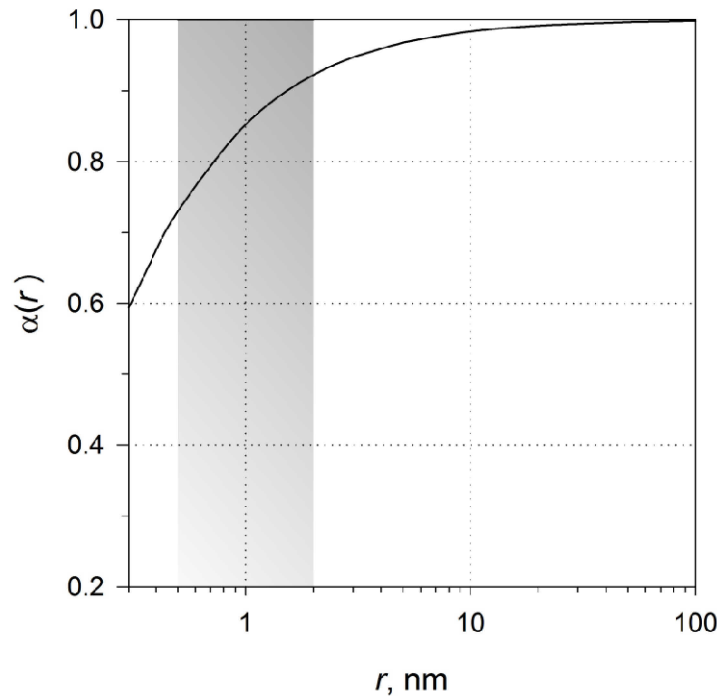


Figure 3 – Shape of the function  $\alpha(r)$  accounting for the interface curvature effects according to ref. [52].

With the planar sharp interfacial energy from the GBB approach and the size effect function  $\alpha(r)$ , one obtains a good estimate of the interfacial energy already in many systems of technical relevance. For the present case of Cu-precipitation in the Fe-Cu system, we elaborate later that it is essential to additionally account for the effect of diffuse interfaces in the approximate form of an interface energy factor  $S(T/T_c)$ , where  $T_c$  is the regular solution critical temperature. This is not part of the conventional modeling approach and, therefore, elucidated later in section 3.2.

#### **2.4 Composition of the critical nucleus**

The chemical composition of the first Cu precipitates directly after nucleation is, even though being thoroughly investigated, still controversial. While atom probe tomography (APT) [21,53-55], extended X-ray absorption spectroscopy (XAS) [56] and calculation of the minimum nucleation energy (see below) suggest that the nucleation event occurs via an Fe-rich nucleus, the results of neutron scattering (SANS) [57], Monte Carlo (MC) [13], first-principles studies [15] or positron annihilation spectroscopy (PAS) [58] are at odds, predicting almost pure-Cu nuclei. Due to detection limitations in experiments, the earliest stages of nucleation are, however, not unambiguously observable, and we still have to rely on substantial speculation. Yuge et al. [16] calculate a most likely critical cluster size of 12 atoms, with a corresponding radius of less than 0.35nm. The detection limits for APT and XAS are, at

its best, at experimental precipitate radii of  $\sim 0.5\text{nm}$ , PAS at  $\sim 0.6\text{nm}$  and TEM and SANS above  $\sim 1.0\text{nm}$  [56]. Most experimental techniques observe the smallest particle radii already at closely above  $0.5\text{nm}$ . A discussion of discrepancies and possible explanations for the various contradicting observations has been compiled by Fine et al. [57].

In a continuums-mechanical analysis of the chemical composition of coherent Cu-precipitates in Fe-Cu based on minimization of the critical nucleation barrier, Kozeschnik [59] suggested an estimate of the nucleus composition of nanometer-sized Cu precipitates in dependence of the overall alloy composition and temperature. These two parameters basically define the amount of supersaturation present during nucleation. The approach, purely based on thermodynamic arguments, accounts for the composition-dependence of the interfacial energy and the chemical driving force. The composition of the nucleus, yielding the lowest critical energy for nucleus formation,  $G^*$ , (Eq. 2), is hence denoted as the “most likely” nucleus composition. Accordingly, by using Boltzmann statistics, the probability for a nucleation event can be expressed as

$$P \approx \exp\left(-\frac{G^*}{k_B T}\right), \quad (4)$$

where  $k_B$  is the Boltzmann constant and  $T$  is the temperature in K. The normalized nucleation probability, as obtained for the present precipitation case, is shown in Figure 4. At low temperatures, the most likely nucleus contains Fe with  $X_{\text{Fe},300} \sim 0.37$  at  $300^\circ\text{C}$ , decreasing gradually to  $X_{\text{Fe},650} \sim 0.06$  at  $650^\circ\text{C}$ .

The predictions of this approach for the Cu content of the critical nucleus are in good qualitative as well as quantitative agreement with the computational analysis of Nagano and Enomoto [60] as well as experimental information obtained with atom probe tomography [53-55,61]. Since the minimum nucleation barrier approach can nowadays be applied on a routinely basis, e.g., inside the software package MatCalc, we consider this in our treatment also as part of the “conventional” precipitation simulation technique.

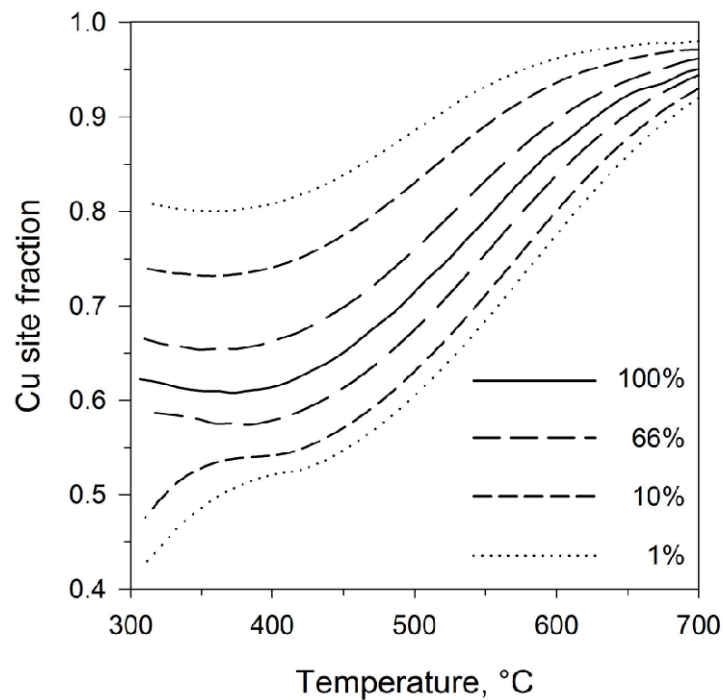
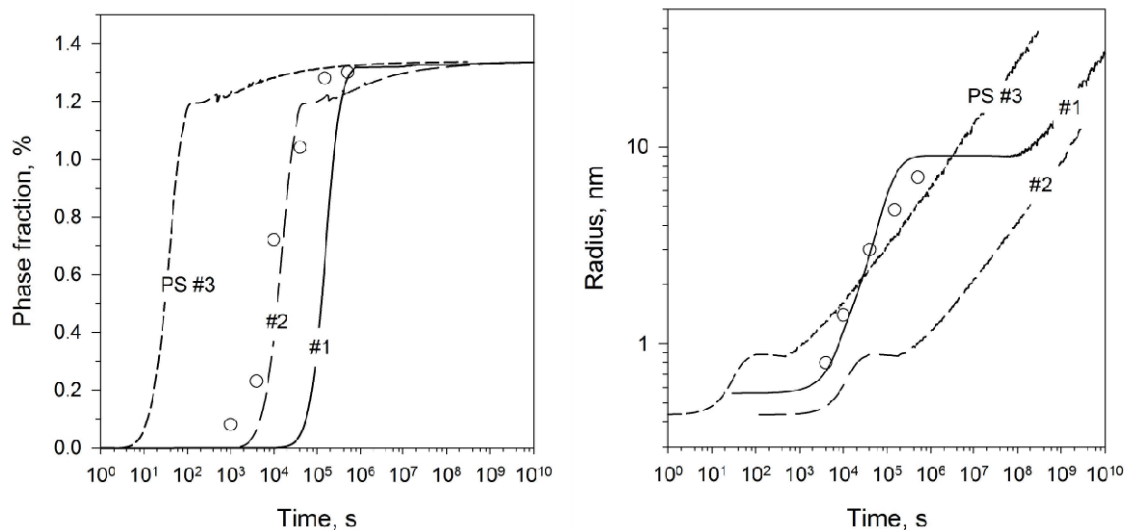


Figure 4 – Normalized nucleation probability as a function of  $T$  and  $X_{\text{Cu}}$  calculated from the minimum  $G^{\ddagger}$  concept [59].

### 2.5 Limitations of the conventional approach

The limitations and problems that are inherent to the conventional precipitation kinetics approach in the Fe-Cu system are discussed next. We present simulation results for the “precipitation parameter triplet” phase fraction,  $f$ , mean radius,  $r$ , and number density,  $N$ , observing that the major difficulty is the lack of a consistent set of simulation input parameters that represents the experimental data for all three precipitation parameters of the triplet simultaneously.



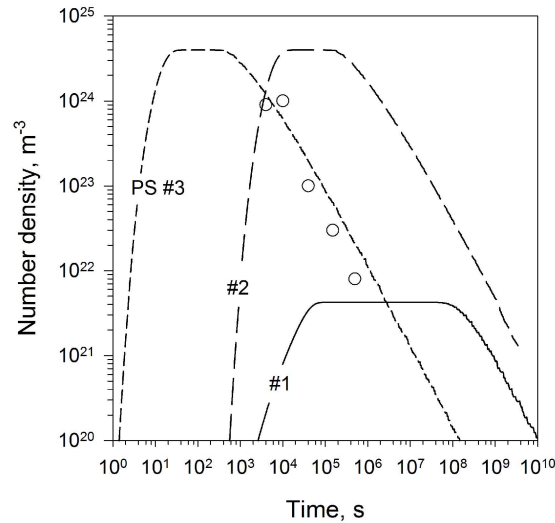


Figure 5 – Parameter studies for phase fraction, mean radius and number density in binary Fe-Cu, comparing to experimental data of Goodman et al. [62]. The applied parameter values are summarized in Table 1.

Figure 5 summarizes the evolution of the precipitation parameters for the experimental conditions used in the study of Goodman et al. [62]. In *parameter study 1*, denoted as “PS1” and shown in bold lines, we successfully reproduce the mean radius evolution of the precipitation system with an increase of the experimentally measured Cu-diffusion coefficient [63] ( $D_{\text{Cu}} = 1.47 \cdot 10^{-22} \text{ m}^2\text{s}^{-1}$  at  $500^\circ\text{C}$ ) by a factor of 20. All other input parameters are left on their default values given by the models reported in the previous sections. With this, we emphasize that we do not rely on any fitting parameter to get experiment and simulation in accordance, but we use all parameters ‘as-predicted’ by the corresponding models. With this variation in input parameter for the diffusion coefficient, the radius evolution is reproduced with good accuracy. However, when inspecting the evolution of the other two parameters of the triplet, we observe a huge discrepancy in the predicted particle density (approx. 3 orders of magnitude) as well as the sluggish increase in phase fraction, which occurs more than one order of magnitude too late compared to experiment.

In *parameter study 2*, we reduce the interfacial energy to 0.78 of its calculated value (GBB value for planar sharp interface plus size effect) and reduce the matrix diffusion enhancement to a factor of 4. A lower interfacial energy triggers a higher nucleus density, see Eq. 2, and, hence, more but smaller nuclei. With PS2, the phase fraction is reproduced nicely, together with the maximum value of the number density as obtained experimentally. However, precipitate growth stops before reaching a radius of  $r \sim 1\text{nm}$  and before establishing the equilibrium phase fraction for the present conditions. Although the phase fraction evolution is reproduced reasonably accurate, the evolution of the mean

radius is entirely incorrect, as well as the evolution of the number density of Cu precipitates. Both of these effects are due to the early stagnation of growth as a consequence of the matrix being depleted from Cu. Since the supersaturation has decreased to a low level, the only remaining driving force for evolution of the precipitation system is the Gibbs-Thomson effect leading to Ostwald ripening. With the low driving forces associated with this effect, both parameters, radius and number density, evolve with incorrect kinetics.

*Parameter study 3* is targeted at a variation of two input parameters: The diffusion coefficient is taken higher by a factor of 1000 and the interfacial energy is reduced as before in PS2. Even though these changes can hardly be justified on a physical basis, this variation seems to be the only possibility to reproduce the decreasing slope of the number density evolution during coarsening at a correct rate and within the “conventional” picture that coarsening occurs under control of monomer desorption/adsorption to the precipitate/matrix interfaces as the conceptual basis of the LSW mechanism [28,29]. However, with the decreasing slope of the number density being reproduced correctly, the phase fraction evolution occurs orders of magnitude too early and the radius evolution shows an incorrect slope. Table 1 summarizes the variation of parameters used in Figure 5.

Table 1 – Parameter study sets for ‘conventional’ Cu precipitation simulation in Fe-1.4 at.-%Cu.

	$D$ $\text{m}^2\text{s}^{-1}$	$\chi$ $\text{mJm}^{-2}$
Calculated at 500°C	$1.47 \cdot 10^{-22}$	570
PS1	$20 \cdot D$	$1 \cdot \chi$
PS2	$4 \cdot D$	$0.78 \cdot \chi$
PS3	$1000 \cdot D$	$0.78 \cdot \chi$

### 3. Effects beyond conventional precipitation modeling

In the previous section, we have demonstrated that the Kampmann-Wagner-based simulation approach utilizing conventional nucleation and growth models leads to an inconsistent reproduction of the precipitation parameter triple. Even the attempt of using the diffusion coefficients and/or interfacial energies as fitting parameters does not deliver agreement between simulation and experimental data simultaneously for all three parameters. In this section, we show that the evolution of the precipitation parameter triplet can be described consistently and with a single set of input

parameter, when taking into account effects, which go beyond conventional precipitation modeling.

These are:

- (i) The structural transformation of Cu-precipitates from bcc to 9R to fcc
- (ii) Interfacial free energy effects due to diffuse interfaces
- (iii) Particle coalescence and abnormal cluster mobility

The implementation of mechanisms (i) to (iii) into our advanced simulation approach and their effect on the Cu precipitation kinetics in  $\alpha$ -Fe is discussed next.

### ***3.1 Transformation sequence of Cu precipitates***

The crystal structure of early coherent Cu precipitates is constrained by the bcc structure of the  $\alpha$ -Fe matrix, forcing the particles to also adopt the embedding bcc structure. During growth, the bcc-Cu precipitates run through one or two structural transformations (twinned 9R, and untwinned 3R) until they ultimately transform to their equilibrium fcc structure [5,6,64] with an incoherent interphase boundary. The transformation from bcc to 9R occurs because the interfacial strain energy increases with particle size during growth. Once a critical radius is reached, a martensitic transformation is triggered and the 9R structure forms. The semi-coherent 9R offers better accommodation of atomic planes across the interface compared to the coherent bcc structure [6] within the rigid bcc matrix.

At even larger radii, the volumetric misfit of the still coherent particles becomes an increasingly dominant term in the particle free energy and a transformation to fcc occurs on further growth. The critical transformation radii used in our work are 2-3 nm and 6-10 nm for the bcc/9R and 9R/fcc transformation, respectively. These values are taken in accordance with experimental information on the transformation ranges [5,6,64]. Precipitates accommodating a single twin are representative for the smallest 9R structure. Upon growth, the number of twins increases and larger 9R precipitates show a distinguished twinned structure. The 9R to fcc transformation is clearly observed experimentally by the disappearance of these twins. The chemical composition of the transforming precipitates is assumed to be identical to that of the parent phase. Coherent bcc and semi-coherent 9R configurations are reported to grow spherically, whereas the fcc particles exhibit rod-like shapes [25]. The influence of shape change on the growth kinetics of precipitates is taken into consideration in the present work as proposed by Kozeschnik et al. [65] with a shape factor of 3 – 5 for the fcc phase.

The actual transformation between the different structures is implemented such that the number density of precipitates from the parent phase is gradually decreased in favor of the product phase starting at the lower transformation radius threshold and the reaction being completed at the higher transformation radius limit. The upper and lower threshold values thus define the ratio of transformed and untransformed precipitates of given size by a linear mixture rule solely determined by the radius of the individual size class of the discrete precipitate distribution. We consider an in-situ transformation from one to the other phase modification, which is why we assume that the chemical composition of transforming precipitates remains unchanged in the transformation process. In Figure 6, the typically observed transformation sequence during Cu-precipitate growth and coarsening is shown for an isothermal heat treatment at 500°C. The transformations are easily observed in terms of the phase fraction evolution.

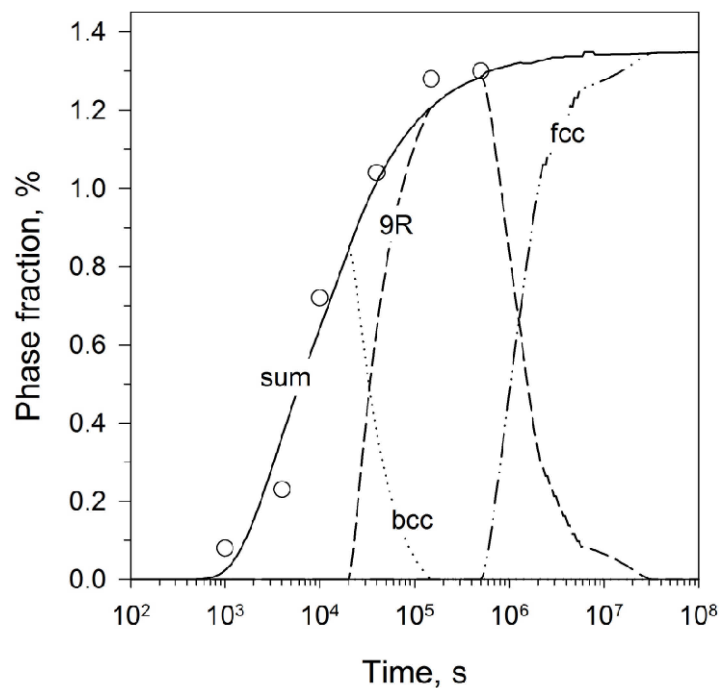


Figure 6 – Evolution of phase fractions during Cu-precipitate growth showing the structural transformations from bcc to fcc.

### ***3.2 Diffuse interface contribution***

The interfacial energy in the GBB approach [49] has originally been derived for coherent sharp planar phase boundaries. In precipitation modeling, this situation rarely applies since (i) the nuclei of new phases are commonly small and can contain as few as only ten atoms or less [15]. As already outlined in the description of the conventional precipitation simulation approach, the curvature effects caused

by the small size of the precipitates can be accounted for, e.g., by the model proposed in ref. [52]. In addition, (ii) thermal activation at elevated temperature leads to mixing of atoms across the interface, making the sharp interface increasingly diffuse. This process generates entropy, which finally decreases the interfacial free energy and must be taken into account properly.

Sonderegger and Kozeschnik [66] have recently developed a corresponding model on basis of the equilibrium chemical profile across the interface as a function of temperature and chemical composition. Unfortunately, and in contrast to the curvature-effect, the general solution of the diffuse interface problem involves minimization of the free energy that can only be performed in an iterative way. Consequently, it renders a direct implementation of the general solution procedure in computationally intensive algorithms unfavorable. Sonderegger and Kozeschnik achieved a closed analytical expression for the energy contribution of diffuse interfaces only in the limit of two interfacial atomic layers and under adaptation of the regular solution thermodynamic model. With the regular solution critical temperature,  $T_c$ , representing the characteristic quantity in this approach and being unique to each precipitation system, this latter approach is used here due to its simplicity and computational efficiency, however, with the slight drawback that  $T_c$  represents an input quantity that inherits some approximation in terms of thermodynamic models and interface thickness. Fig. 7 displays the shape of the diffuse interface energy function,  $\beta$ , as a function of temperature relative to  $T_c$ .

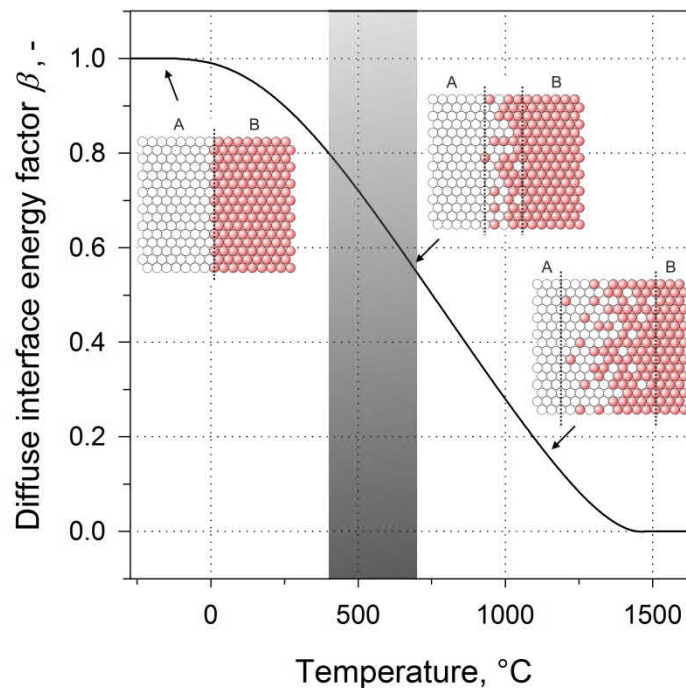


Figure 7 – The diffuse interface energy factor calculated for a regular solution critical temperature of 1750K (1477°C). The temperature region studied in the present report is marked in gray.

In regular solution thermodynamic systems,  $T_c$  is directly related to the (composition-independent) interaction energy between the Fe and Cu atoms. In the present case, this relation does not fully apply since the ferro-magnetic transition on the Fe-rich side introduces some asymmetry below the Curie temperature into the metastable (bcc) Fe-Cu phase diagram. In the attempt to get a reasonable estimate for  $T_c$ , we carry out a stepped equilibrium calculation to follow the phase boundary of the Fe-Cu miscibility gap as a function of chemical composition (Fig. 8).  $T_c$  can then be read from the maximum temperature of the phase boundary with a value of 1840K. A different approach was used in ref. [67], where an approximation for  $T_c$  was given as  $T_c \approx 0.4 \cdot \Omega/k_B \approx 1723\text{K}$ , with  $\Omega$  being the condition of equal solution enthalpies of Cu in Fe and vice versa. Keeping in mind that the closed expression in  $T_c$  represents only an approximation, we finally adopt a value of  $T_c = 1750\text{K}$  in our simulations, as it delivers best agreement and consistency to experimental data over a large range of temperatures and compositions and it is sufficiently close to the estimated value of 1840K. This value introduces a significant diffuse interface energy reduction with  $S(T/T_c) = 0.8$  to 0.5 at temperatures from approximately 400 to 700°C, respectively.

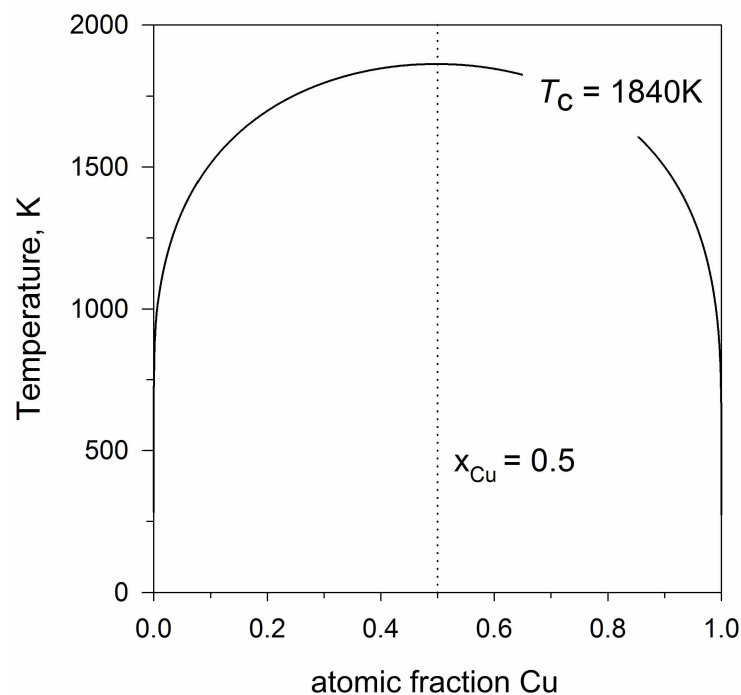


Figure 8 – Estimation of the regular solution critical temperature,  $T_c$ , in metastable bcc Fe-Cu from evaluation of the miscibility gap.

When inspecting the diffuse interface energy change with  $S(T/T_c)$  over the temperature range of the present work, one clearly recognizes the importance of this contribution to the evaluation of the interfacial energy (see gray area in Fig. 7). The first important aspect here is certainly the absolute value of the reduction, which is substantial. The second aspect is the temperature dependence of this effect, which is also significant over the temperature range of interest. Without this dependence, the TTP diagram calculation elaborated later would widely fail in reproducing the experimentally observed shape.

### ***3.3 Coalescence and abnormal cluster mobility***

In several metallic alloys, such as, for instance, the Fe-Cu system, attractive and repulsive interactions between vacancies (Va) and the elements of the alloy are of immediate importance for the kinetics of phase decomposition processes. These interactions were analyzed by Soisson and Fu [67], observing that the vacancy-solute interactions are of repulsive nature in the case of Fe-Va, and attractive for Cu-Va. Barashev and Arokiam [68] deduce that it is the strong binding energies up to the second nearest neighbor that lead to stable Cu-Va dipoles, which do not easily dissociate during diffusion.

Numerous authors investigated the mobility of Cu clusters in an Fe matrix [11,14,67,69] compared to Cu monomers and found that the cluster mobility is enhanced by several orders of magnitude compared to single atoms. Warczok et al. [69] observed enhanced cluster mobility in binary Fe-Cu using a rigid lattice Metropolis Monte Carlo algorithm with real-time coupling, where the system evolution was driven by a single vacancy. The simulations showed that the vacancy preferably migrates to the matrix/precipitate interface, leading to a substantial net movement of the cluster [67]. Jourdan et al. [11,14] evaluated this acceleration to be of two orders of magnitude compared to monomers. The high mobility of clusters and their Brownian motion-like migration through the sample finally leads to cluster collisions and particle coalescence. This effect was also confirmed in the work of Castin et al. [8], who showed that the coarsening behavior in bcc Fe-Cu can only be reproduced when taking the coalescence mechanism into account.

In our simulations, we account for the impact of particle coalescence with the continuums Ansatz developed by Warczok et al. [69]. Accordingly, each cluster is assigned a certain size-dependent diffusivity,  $D_l$ , with [70,71]

$$D_l \sim D_1 \cdot l^n, \quad (5)$$

with  $l$  representing the particular precipitate size class in the simulation,  $D_1$  the mobility of the monomer and  $n$  the Binder-Stauffer exponent. As a consequence of continuous particle collisions, it is

assumed that the total number density of precipitates,  $N$ , decreases proportional to the cross-sectional area of the precipitates described by the mean radius,  $\bar{r}^2$ . The rate of the particle density,  $\dot{N}_i^c$ , for each size class can then be written as

$$\dot{N}_i^c = kN\bar{r}^2 D_i, \quad (6)$$

with  $k$  representing a calibration factor for the strength of the coalescence effect.

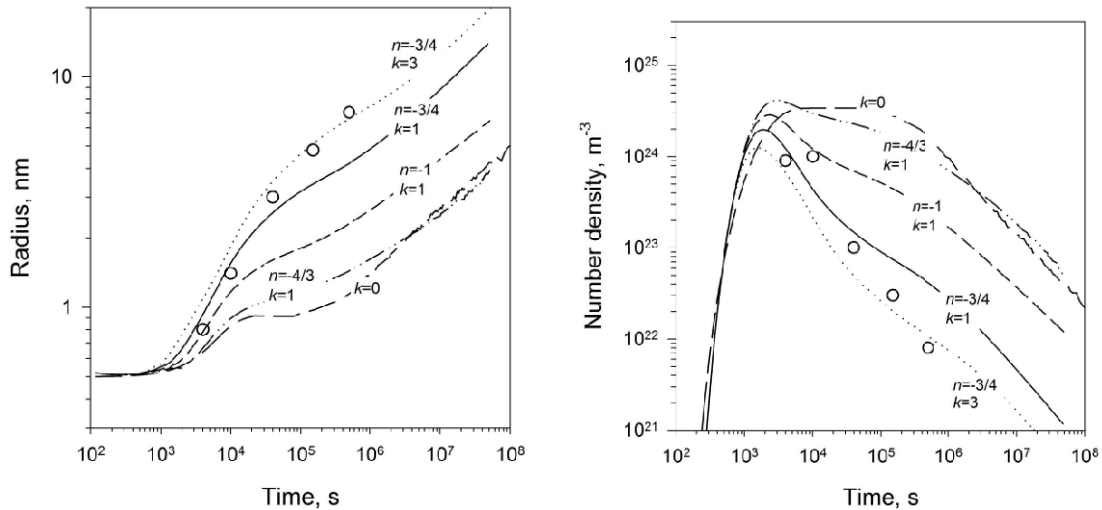


Figure 9 – Evolution of radius and number density with different coalescence factors ( $k$ ) and Binder-Stauffer coefficients ( $n$ ).

A direct consequence of particle coalescence in our simulations is the significantly earlier onset and higher effective growth rate for precipitation compared to the case without coalescence. This is elaborated in Figure 9 for different values of  $n$  and  $k$ . At the same time, the typical plateau in the number density evolution before the onset of coarsening, which is characteristic for Kampmann-Wagner type precipitation models, disappears.

In their original work, Binder and Stauffer [70,71] evaluated the kinetics of liquid droplets formation from supersaturated vapor and suggest that the cluster migration rate scales with  $I^{4/3}$ , and evolves towards  $I^1$  for growing particles. In our studies, we apply a Binder-Stauffer coefficient of  $n=-3/4$  to reproduce the experimental data consistently. As a consequence of  $n$  being a negative value, typically between  $-4/3 < n < -3/4$ , the cluster migration rate decreases steadily with increasing cluster size (Fig. 10). Thus, the effect of coalescence also decreases gradually with increasing mean radius of the Cu-precipitates.

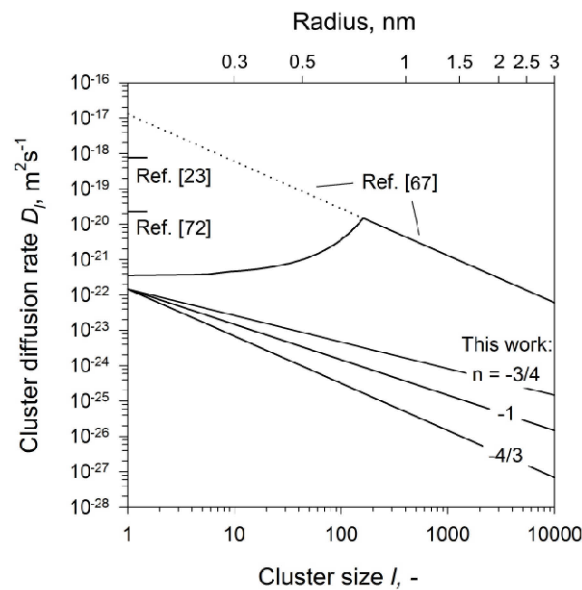


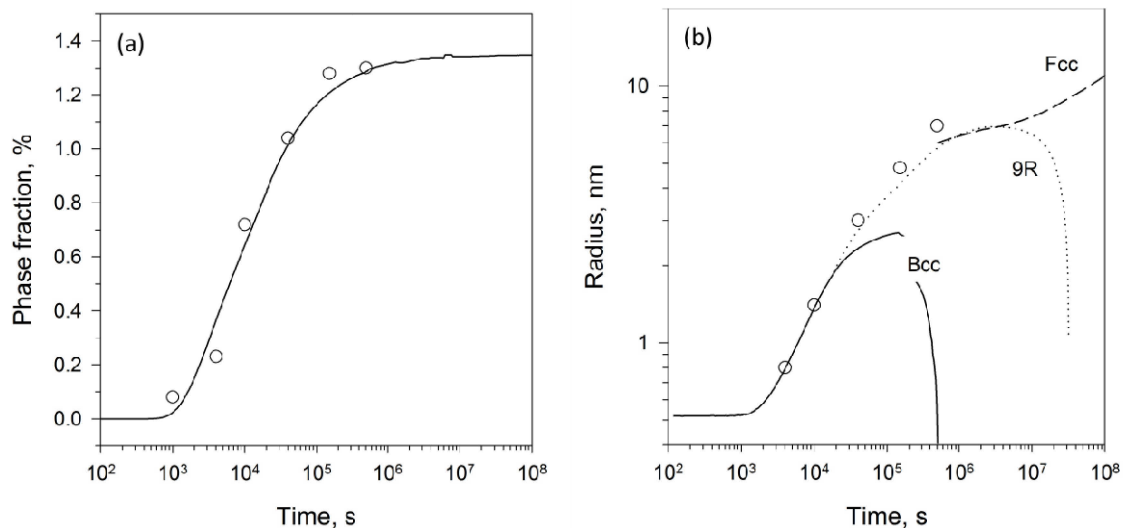
Figure 10 – Cluster and monomer diffusion rates as used in literature together with the classical Binder-Stauffer expression and variation in  $n$ .

Soisson and Fu [67] developed a modified Binder-Stauffer expression for the cluster diffusion rate from ab-initio bond energies, including vacancy concentration and migration energy on the interface. They remark, however, that, for small clusters, the diffusion rate might be overestimated and they use atomistic kinetic Monte Carlo results to evaluate the diffusion rates up to the intersection point with the Binder-Stauffer curve. Other researchers [23,72] assume a 100 – 1000 times higher monomer diffusion rate to compensate for the absence of cluster migration in their simulation approach. A comparison of the applied diffusion rates is given in Figure 10.

In the present work, we utilize combinations of  $n$  and  $k$  as summarized in the Appendix B. In the absence of any direct experimental information on coalescence rates, we calibrate both parameters such that the experimentally observed number density and radius evolution are best reproduced. The trend observed in the Monte Carlo simulations, namely, an increased cluster mobility for smaller precipitates and a decreasing mobility enhancement for larger sizes, is reflected in the lower negative exponent used for the small bcc/9R precipitates and the higher values for the larger fcc modification. Using mobility enhancement functions similar to the one suggested in ref. [67] and indicated in Figure 10, i.e., increasing absolute values for the cluster mobility at small sizes and then following the modified Binder-Stauffer function, did not deliver satisfying results in combination with the coalescence model [69] used in the present study.

### 3.4 The precipitation parameter triplet at 500°C

After consideration of all effects described earlier in the conventional modeling approach as well as the effects of coalescence, diffuse interfaces and structural transformation from bcc to fcc, a satisfying reproduction of the experimental data of Goodman et al. [62] is achieved. The simulated evolution of radius, number density, phase fraction, and nucleus composition is shown in Figure 11. The parameter set entering the simulation is summarized in the Appendix B. At a temperature of 500°C, nucleation starts after about 100 seconds with clusters of approximately 45 atoms and a corresponding radius of 0.5 nm. The composition is calculated according to the maximum  $G^*$  concept [59] with 70% Cu, and evolves as a consequence of growth towards pure Cu. The progress of this evolution is strongly dependent on the inner particle diffusion rate. This quantity, however, is hardly accessible by experimental means, especially for coherent bcc-Cu structure. In Figure 11d we show two assumptions for inner particle diffusion rates, one equal to the surrounding bcc matrix, the other reduced by a factor 100, respectively. With this manipulation, the pure Cu configuration is predicted at radii between 1 to 4 nm. The impact of this parameter is indiscernible in phase fraction, radius and number density. As soon as the critical radius for transformation is reached, the crystal structure is transformed into the semi-coherent 9R, first, and ultimately into the incoherent fcc structure. The corresponding threshold values are also listed in the appendix.



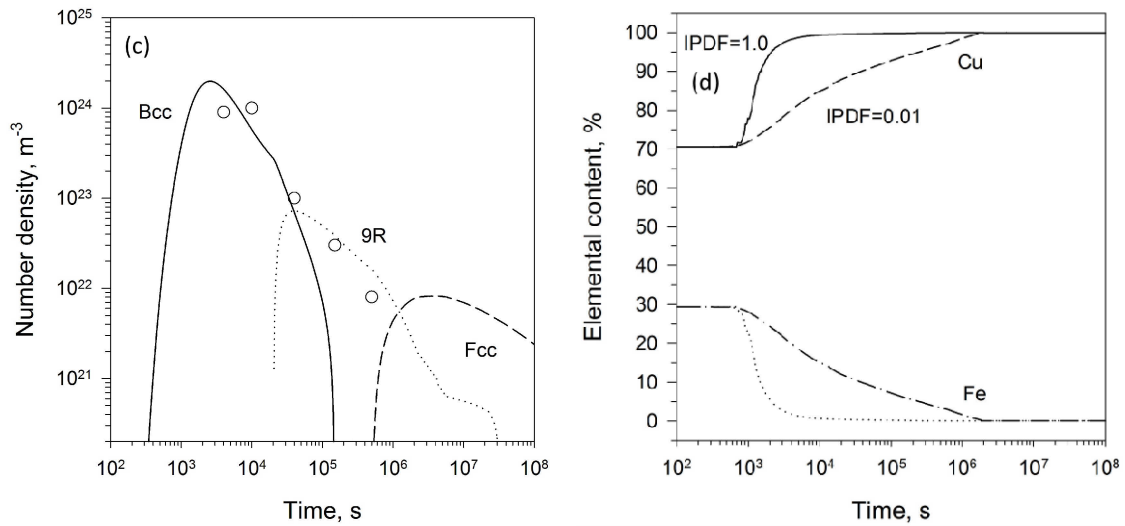


Figure 11 – Evolution of (a) phase fraction, (b) radius, (c) number density and (d) nucleus composition of coherent bcc-Cu with inner particle diffusion factor (IPDF) variation in Fe-1.4at.-%Cu and experimental data after Goodman [62].

#### 4. Temperature dependence of Cu precipitation

After evaluation and calibration of Fe-Cu kinetics simulations at a temperature of 500 °C, we attempt the simulation of Cu precipitation in Fe in the form of an isothermal time-temperature-precipitation (TTP) diagram. To the best knowledge of the authors, only a single experimental evaluation is available in literature that covers a wider temperature range extending outside the typical tempering temperatures of technological interest of 500-600 °C using a binary Fe-1.2at.-%Cu alloy. The following TTP plot (Fig. 12) is compared to the diagram reported by Perez et al. [73] using the same simulation input parameter set as before and considering the effects elucidated in section 3. At every temperature in intervals of 10 K, a kinetic simulation is performed and the maximum phase fraction is used as threshold to calculate the times for 10%, 50% and 90% precipitated phase fraction.

The experimental data that we compare our simulations to have been obtained from thermo-electric power measurements [73]. To emphasize the inherent variation in results between different experiments even for very similar experimental conditions, the 10% and 90% precipitation times of Goodman et al. [62], obtained by field-ion microscopy and TEM, are also included in the diagram. To account for experimental uncertainties, we show two possible parameterizations leading to similar results. In case A, we increase the diffusion kinetics previously applied in the calculations of section 3 by an additional factor of 2. In case B, the diffusion coefficient is used as given in the database [63], but the dislocation density is set to a value of  $4 \cdot 10^{13} \text{ m}^{-2}$  and  $T_c$  is slightly decreased to 1700 K. All other parameters are utilized as previously described and with the values summarized in the appendix.

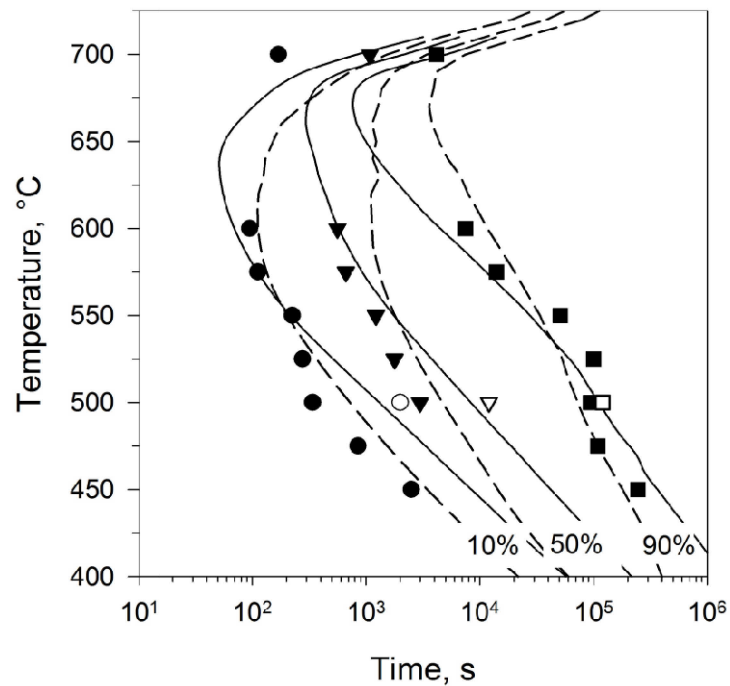


Figure 12 – Isothermal TTP diagram with experimental data of Perez et al. [73] and Goodman et al. [62], shown in filled and empty symbols, respectively. Solid lines show case A with additional diffusion enhancement by a factor 2; dashed lines show case B with default diffusion values and an increased equilibrium dislocation density of  $4 \cdot 10^{13} \text{ m}^{-2}$ .

Both cases reproduce the reported data of literature within the inherent experimental spread. Case A shifts all precipitation curves to earlier times, independent of temperature, as a consequence of the enhanced diffusion kinetics. In case B, the kinetics is also accelerated, however the operative mechanism (dislocation pipe diffusion) is different and has a higher impact at low temperatures. Details on the model for dislocation pipe diffusion are given in ref. [74]. The assessment of pipe diffusion coefficients is reported in ref. [75]. Fig. 12 shows that the parameterization of case B reproduces the experimental data better at temperatures below 550 °C, whereas case A appears to deliver better agreement at higher temperatures. A unique decision, which approach represents the experimental conditions in ref. [73] closer is unfortunately not possible based on the information provided in this reference.

## 5. Consistency with other experiments

Steel grades containing more than 0.5 wt.-% Cu are of significant technical interest due to their particle strengthening potential. As a consequence, they have been investigated numerous times and a variety of experimental results for the evolution of precipitates are available. With our present simulation

approach, we attempt to reproduce these data as shown in Table 2. The measured radii come from literature of the last five decades, measured with different methods, at different times and different compositions and temperatures. We observe good accuracy in the simulated and experimental radius data over the entire range of temperatures and experimental conditions.

Table 2 – Simulated and experimentally determined radii for various conditions.

Ref.	$T, ^\circ\text{C}$	Cu-cont,wt.-%	$t, \text{s}$	$r_{\text{exp}}, \text{nm}$	$r_{\text{sim}}, \text{nm}$	Method
Mathon 1997 [1]	500	1.52	511200	$6.3 \pm 0.3$	5.7	SANS
Osamura 1994 [4]	550	1.6	1800	3	2.5	SANS
Osamura 1994 [4]	500	1.3	40000	3.4	2.9	SANS
Lozano 2006 [7]	405	0.5	$3.60\text{E}+07$	$3 \pm 0.6$	3.1	3DAP+EDX+HRTEM
Lozano 2006 [7]	365	0.5	$3.60\text{E}+07$	$1.8 \pm 0.6$	2.1	3DAP+EDX+HRTEM
Speich 1965 [25]	830	2.3	360000	147*	111-135*	TEM
Speich 1965 [25]	730	2.3	360000	37*	40-55*	TEM
Gagliano 2004 [21]	500	1.3	6000	$1.4 \pm 0.4$	1.2	APT, TEM
Gagliano 2004 [21]	550	1.3	7200	$3.2 \pm 1.6$	3.7	TEM
Kampmann 1985 [46]	500	1.57	1000	0.53	0.55	SANS
Kampmann 1985 [46]	500	1.57	700000	7.4	7.4	SANS
Isheim 2007 [53]	500	1.93	12000	1.3	1.9	APT
Isheim 2006 [54]	490	1.37	6000	$1.25 \pm 0.15$	1	APT
Prakash 2008 [55]	500	2.09	900	$1.2 \pm 0.1$	0.6	APT
Prakash 2008 [55]	500	2.09	3686400	$6.5 \pm 0.7$	7.7	APT

\* In the work of Speich and Oriani [25], elongated Cu precipitates with radii up to 150 nm and lengths of more than one  $\mu\text{m}$  are observed. Only the diameter of the rod-like precipitates are reported in the publication, no information is provided on the length. When comparing our results with these data, we assume an average length to thickness ratio between 3 and 5.

## 6. Conclusions

The present analysis introduces an original and comprehensive model for the simulation of precipitation kinetics in binary Fe-Cu, which successfully and consistently reproduces experimental data available on the precipitation triplet of phase fraction, mean radius and number density. Most important in this context is the mandatory consideration of physical mechanisms that go beyond conventional precipitation kinetics simulation. We demonstrate that the experimental observations can only be consistently described when additionally taking into account the effects of diffuse interfaces, particle coalescence and structural transformation of precipitates.

With the new approach, we successfully reproduce the evolution of phase fraction, mean radius and number density in good accuracy at typical temperatures where technical heat treatments are commonly carried out (500-550 °C) and where detailed microstructure information is available. With the GBB treatment of diffuse interfaces, we also reproduce the temperature-dependence of the observed precipitation kinetics for the available time-temperature-precipitation data in the temperature range from 450 to 700 °C. We demonstrate that this is only possible if the composition dependence of the Curie temperature is correctly taken into account to obtain accurate values of the specific interfacial energy particularly in the vicinity of the ferromagnetic to paramagnetic transition region.

### **Acknowledgements**

G.S. gratefully acknowledges the fruitful discussions with Yao Shan and Peter Lang. Financial support by the Austrian Federal Government (in particular from Bundesministerium für Verkehr, Innovation und Technologie and Bundesministerium für Wissenschaft, Forschung und Wirtschaft) represented by Österreichische Forschungsförderungsgesellschaft mbH and the Styrian and the Tyrolean Provincial Government, represented by Steirische Wirtschaftsförderungsgesellschaft mbH and Standortagentur Tirol, within the framework of the COMET Funding Programme is gratefully acknowledged.

### **Appendix A**

The impact of the present reassessment of thermodynamic parameters of the magnetic contribution to the interface energy is shown in Fig. 1. The previous CALPHAD modeling approaches for the Curie temperature assumed a linear composition dependence. To correctly represent this quantity in accordance with experiments of Sumiyama et al. [45], an excess interaction energy of 800 J/mol is assumed in the present work. Table A.1 summarizes the reassessed thermodynamic parameters as utilized in our thermokinetic calculations. The unary Gibbs energies are taken from Dinsdale, CALPHAD 15 (1991) 317-425.

Table A.1: Thermodynamic parameters of the present reassessment of the Fe-Cu system.

#### **Bcc\_a2**

Sublattice model: (Cu,Fe)(Va)

Interaction parameters:

$${}^0L_{Cu,Fe}^{bcc} = +56000 - 13.9T$$

$${}^0T_{Curie;Cu,Fe}^{bcc} = +800$$

### Fcc\_a1

Sublattice model: (Cu,Fe)(Va)

Interaction parameters:

$${}^0L_{Cu,Fe}^{fcc} = +48500 - 8.0T$$

$${}^1L_{Cu,Fe}^{fcc} = -2500 + 2.0T$$

$${}^2L_{Cu,Fe}^{fcc} = +2500 - 2.0T$$

### Liquid

Sublattice model: (Cu,Fe)(Va)

Interaction parameters:

$${}^0L_{Cu,Fe}^{liq} = +74500 - 143.5T + 15.82T \cdot \ln T$$

$${}^1L_{Cu,Fe}^{liq} = +8500 - 6.0T$$

$${}^2L_{Cu,Fe}^{liq} = +3000$$

$${}^3L_{Cu,Fe}^{liq} = -233.62$$

### Appendix B

The following parameter set (Table B.1) was developed and calibrated on basis of the experimental data of Goodman et al. [62]. Details concerning the parameter studies are elaborated in section 3.

Table B.1 – Evaluated parameter set for simulation of Cu precipitation in Fe-1.4at.-%Cu using MatCalc version 5.62.1001.

		bcc	9R	fcc
Transformation radius nm	min	-	2	6
	max	-	3	10
Regular solution Temp., K	$T_c$	1750	-	-
Nucleation model	-	Max. nucl. rate	Direct particle transformation	Direct particle transformation
Nucleation site	-	Bulk	bcc-Cu	9R-Cu
BS-exponent	$n$	-3/4	-3/4	-1
Coalescence factor	$k$	1	3	6
		Precipitation domain		

Matrix diffusion enhancement	-	8 (1)
Grainsize	$\mu\text{m}$	100
Dislocation density	$\text{m}^{-2}$	$1 \cdot 10^{12}$ ( $4 \cdot 10^{13}$ )

## References

1. M.H. Mathon, A. Barbu, F. Dunstetter, F. Maury, N. Lorenzelli, C.H. de Novion, "Experimental study and modelling of copper precipitation under electron irradiation in dilute FeCu binary alloys", *J. Nucl. Mater.*, 245 (1997) 224-237.
2. J.D. Farren, A.H. Hunter, J.N. Dupont, D.N. Seidman, C.V. Robinho, E. Kozeschnik, "Microstructural evolution and mechanical properties of fusion welds in an Iron-Copper-Based multicomponent steel", *Metall. Mater. Trans. A*, 43 (2012) 4155-4170.
3. U.K. Viswanathan, P.K.K. Nayar, R. Krishnan, "Kinetics of precipitation in 17-4 PH stainless steel", *Mater. Sci. Tech.*, 5 (1989) 346-349.
4. K. Osamura, H. Okuda, K. Asano, M. Furusaka, K. Kishida, F. Kurosawa, R. Uemori, "SANS Study of Phase Decomposition in Fe-Cu Alloy with Ni and Mn Addition", *ISIJ International*, 34 (1994) 346-354.
5. P.J. Othen, M.L. Jenkins, G.D.W. Smith, "High-resolution electron microscopy studies of the structure of Cu precipitates in alpha-Fe", *Phil. Mag. Lett.*, 70 (1994) 1-24.
6. P.J. Othen, M.L. Jenkins, G.D.W. Smith, W.J. Phythian, "Transmission electron microscope investigations of the structure of copper precipitates in thermally-aged Fe-Cu and Fe-Cu-Ni", *Phil. Mag. Lett.*, 64 (1991) 383-391.
7. S. Lozano-Perez, G. Sha, J.M. Titchmarsh, M.L. Jenkins, S. Hirosawa, A. Cerezo, G.D.W. Smith, "Comparison of the number densities of nanosized Cu-rich precipitates in ferritic alloys measured using EELS and EDX mapping, HREM and 3DAP", *J. Mater. Sci.*, 41 (2006) 2559-2565.
8. N. Castin, M.I. Pascuet, L. Malerba, "Modeling the first stages of Cu precipitation in alpha-Fe using a hybrid atomistic kinetic Monte Carlo approach", *Journ. Chem. Phys.*, 135 (2011) 1-9.
9. S. Schmauder, P. Binkele, "Atomistic computer simulation of the formation of Cu-precipitates in steels", *Comp. Mater. Sci.*, 24 (2002) 42-53.
10. D. Molnar, R. Mukherjee, A. Choudhury, A. Mora, P. Binkele, M. Selzer, B. Nestler, S. Schmauder, "Multiscale simulations on the coarsening of Cu-rich precipitates in alpha-Fe using

- kinetic Monte Carlo, molecular dynamics and phase-field modeling", *Acta Mater.*, 60 (2012) 6961-6971.
11. T. Jourdan, J.-L. Bocquet, F. Soisson, "Modeling homogeneous precipitation with an event-based Monte Carlo method: Application to the case of Fe-Cu", *Acta Mater.*, 58 (2010) 3295-3302.
  12. H. Ren, H. Wang, Z. Liu, "Cu precipitation dynamics in an Fe-1.18%Cu alloy", *Adv. Mater. Res.*, 509 (2012) 22-27.
  13. F. Soisson, A. Barbu, G. Martin, "Monte Carlo simulation of copper precipitation in dilute iron-copper alloys during thermal ageing and under electron irradiation", *Acta Mater.*, 44 (1996) 3789-3800.
  14. T. Jourdan, F. Soisson, E. Clouet, A. Barbu, "Influence of cluster mobility on Cu precipitation in alpha-Fe: A cluster dynamics modeling", *Acta Mater.*, 58 (2010) 3400-3405.
  15. A. Seko, S. R. Nishitani, I. Tanaka, H. Adachi, E. F. Fujita, "First-principle calculation on free energy of precipitate nucleation", *CALPHAD*, 28 (2004) 173-176.
  16. K. Yuge, A. Seko, I. Tanaka, S. R. Nishitani, "First-principles study of the effect of lattice vibrations on Cu nucleation free energy in Fe-Cu alloys", *Phys. Rev. B*, 72 (2005) 1-7.
  17. D. Reith, M. Stoehr, R. Podloucky, R., T.C. Kerscher, S. Muller, "First-principles modeling of temperature- and concentration-dependent solubility in the phase-separating alloy  $\text{Fe}_x\text{Cu}_{1-x}$ ", *Phys. Rev. B*, 86 (2012) 020201.
  18. M. Perez, M. Dumont, D. Acevedo-Reyes, "Implementation of classical nucleation and growth theories for precipitation", *Acta Mater.*, 56 (2008) 2119-2132.
  19. I. Holzer, E. Kozeschnik, "Computer simulation of the yield strength evolution in Cu-precipitation strengthened ferritic steel", *Mater. Sci. Eng. A*, 527 (2010) 3546-3551.
  20. J.B. Yang, M. Enomoto, C. Zhang, "Modeling Cu precipitation in tempered martensitic steels", *Mater. Sci. Eng. A*, 422 (2006) 232-240.
  21. M.S. Gagliano, M.E. Fine, "Characterization of the Nucleation and Growth Behaviour of Copper Precipitates in Low-Carbon Steels", *Metall. Mater. Trans. A*, 35 (2004) 2323-2329.
  22. J. Yang, M. Enomoto, "Numerical Simulation of Copper Precipitation during Aging in Deformed Fe-Cu Alloys", *ISIJ International*, 45 (2005) 1335-1344.
  23. F. Christien, A. Barbu, "Modelling of copper precipitation in iron during thermal aging and irradiation", *J. Nucl. Mater.*, 324 (2004) 90-96.
  24. A.V. Barashev, S.I. Golubov, D.J. Bacon, P.E.J. Flewitt, T.A. Lewis, "Copper precipitation in Fe-Cu alloys under electron and neutron irradiation", *Acta Mater.*, 52 (2004) 877-886.

25. G.R. Speich, R.A. Oriani, "The Rate of Coarsening of Copper Precipitate in an Alpha-Iron Matrix", *Trans. Metall. Soc. AIME*, 233 (1965) 623-631.
26. S.I. Golubov, Yu.N. Osetsky, A. Serra, A.V. Barashev, "The evolution of copper precipitates in binary Fe-Cu alloys during ageing and irradiation", *J. Nucl. Mater.*, 226 (1995) 252-255.
27. R. Monzen, K. Takada, K. Matsuda, "Coarsening kinetics of Cu particles in an Fe-1.5 % Cu alloy", *Z. Metallkd.*, 94 (2003) 1241-1246.
28. I.M. Lifshitz, V.V. Slyozov, "The kinetics of precipitation from supersaturated solid solutions", *J. Phys. Chem. Solids*, 19 (1961) 35-50.
29. C. Wagner, "Theorie der Alterung von Niederschlägen durch Umlösen (Ostwald-Reifung)", *Z. Elektrochem.*, 65 (1961) 581-591.
30. J. Svoboda, F.D. Fischer, P. Fratzl, E. Kozeschnik, "Modelling of kinetics in multi-component multi-phase systems with spherical precipitates I – theory", *Mater. Sci. Eng. A*, 385 (2004) 166-174.
31. E. Kozeschnik, J. Svoboda, P. Fratzl, F.D. Fischer, "Modelling of kinetics in multi-component multi-phase systems with spherical precipitates II – numerical solution and application", *Mater. Sci. Eng. A*, 385 (2004) 157-165.
32. R. Kampmann, R. Wagner, "Kinetics of Precipitation in Metastable Binary Alloys - Theory and Application to Cu-1.9at%Ti and Ni-14at%Al", in: *Proceedings of the 2nd Acta-Scripta Metallurgica Conference*, Sonnenberg, 1984, pp. 91-103.
33. J.D. Robson, "Modelling the overlap of nucleation, growth and coarsening during precipitation", *Acta Mater.*, 52 (2004) 4669-4676.
34. R. Radis, M. Schaffer, M. Albu, G. Kothleitner, P. Pölt, E. Kozeschnik, "Multimodel size distributions of gamma' precipitates during continuous cooling of UDIMET 720 Li", *Acta Mater.*, 57 (2009) 5739-5747.
35. K.C. Russell, "Nucleation in solids: the induction and steady state effects", *Adv. Colloid Interfac.*, 13 (1980) 205-318.
36. E. Kozeschnik, "Modeling Solid-State Precipitation", first ed., Momentum Press, New York, 2013.
37. C.M. Zener, "Theory of Growth of Spherical Precipitates from Solid Solution", *J. Appl. Phys.*, 20 (1949) 950-953.
38. J. Agren, G.P. Vassilev, "Computer simulations of cementite dissolution in austenite", *Mater. Sci. Eng.*, 64 (1984) 95-103.
39. L. Onsager, "Reciprocal relations in irreversible processes: I", *Phys. Rev.*, 37 (1931) 405-426.

40. J. Svoboda, I. Turek, "On diffusion-controlled evolution of closed solid-state thermodynamic systems at constant temperature and pressure", *Phil. Mag. B*, 64 (1991) 749-759.
41. H.L. Lukas, S.G. Fries, B. Sundman, "Computational thermodynamics: the Calphad method", Vol. 131, Cambridge University Press (2007).
42. E. Povoden-Karadeniz, Thermodynamic database mc\_fe.tdb, Vienna University of Technology, version 2.050 (2015).
43. M.A. Turchanin, P.G. Agraval, I.V. Nikolaenko, "Thermodynamics of Alloys and Phase Equilibria in the Copper-Iron System", *J. Phase Equilib.*, 24 (2003) 307-319.
44. K. Shubhank, Y.B. Kang, "Critical evaluation and thermodynamic optimization of Fe-Cu, Cu-C, Fe-C binary systems and Fe-Cu-C ternary system", *CALPHAD*, 45 (2014) 127-137.
45. K. Sumiyama, T. Yoshitake, Y. Nakamura, "Magnetic Properties of Metastable bcc and fcc Fe-Cu Alloys Produced by Vapor Quenching", *J. Phys. Soc. Jpn.*, 53 (1984) 3160-3165.
46. R. Kampmann, R. Wagner, "Phase transformations in Fe-Cu-Alloys – SANS experiments and theory", in: *Proceedings of the IFF-ILL Workshop*, Jülich, 1985, pp. 73-77.
47. A.J. Ardell, "Interfacial Free Energies and Solute Diffusivities from Data on Ostwald Ripening", *Interface Sci.*, 3 (1995) 119-125.
48. X. Li, N. Saunders, A.P. Miodownik, "The Coarsening Kinetics of  $\gamma'$  Particles in Nickel-Based Alloys", *Met. Mater. Trans.*, 33 (2002) 3367-3373.
49. B. Sonderegger, E. Kozeschnik, "Generalized Nearest-Neighbor Broken-Bond Analysis of Randomly Oriented Coherent Interfaces in Multicomponent Fcc and Bcc Structures", *Metall. Mater. Trans. A*, 40 (2009) 499-510.
50. R. Radis, E. Kozeschnik, "Kinetics of AlN precipitation in microalloyed steel", *Model. Simul. Mater. Sci. Eng.*, 18 (2010) 055003.
51. E. Povoden-Karadeniz, E. Kozeschnik, "Simulation of Precipitation Kinetics and Precipitation Strengthening of B2-precipitates in Martensitic PH 13-8 Mo Steel", *ISIJ International*, 52 (2012) 610-615.
52. B. Sonderegger, E. Kozeschnik, "Size dependence of the interfacial energy in the generalized nearest-neighbor broken-bond approach", *Scripta Mater.*, 60 (2009) 635-638.
53. D. Isheim, M.E. Fine, D.N. Seidman, "Precipitate Size Distributions and Compositions of Cu-rich Precipitates in an Fe(Cu) Alloy Studied by Local-Electrode Atom-Probe (LEAP) Tomography", *Microsc. Microanal.*, 13 (2007) 1624-1625.

54. D. Isheim, M.S. Gagliano, M.E. Fine, D.N. Seidman, "Interfacial segregation at Cu-rich precipitates in a high-strength low-carbon steel studied on a sub-nanometer scale", *Acta Mater.*, 54 (2006) 841-849.
55. R. Prakash Kolli, D.N. Seidman, "The temporal evolution of the decomposition of a concentrated multicomponent Fe-Cu-based steel", *Acta Mater.*, 56 (2008) 2073-2088.
56. G. Kuri, C. Degueldre, J. Bertsch, J. Rothe, "Local atomic structure in iron copper binary alloys: An extended X-ray absorption fine structure study", *J. Nucl. Mater.*, 362 (2007) 274-282.
57. M.E. Fine, J.Z. Liu, M.D. Asta, "An unsolved mystery: The composition of bcc Cu alloy precipitates in bcc Fe and steels", *Mat. Sci. Eng. A*, 463 (2007) 271-274.
58. P. Asoka-Kumar, B.D. Wirth, P.A. Sterne, R.H. Howell, "Composition and magnetic character of nanometre-size Cu precipitates in reactor pressure vessel steels: implications for nuclear power plant lifetime extension", *Phil. Mag. Lett.*, 82 (2002) 609-615.
59. E. Kozeschnik, "Thermodynamic prediction of the equilibrium chemical composition of critical nuclei: Bcc Cu precipitation in  $\alpha$ -Fe", *Scripta Mater.*, 59 (2008) 1018-1021.
60. T. Nagano, M. Enomoto, Simulation of the growth of copper critical nucleus in dilute bcc Fe-Cu alloys, *Scripta Mater.* 55 (2006) 223-226.
61. S. Primig, G. Stechauner, E. Kozeschnik, "Early Stages of Cu Precipitation in 15-5 PH Maraging Steel Revisited – Part I: Experimental Analysis", *Steel Res. Int.*, 2016, in print.
62. S.R. Goodman, S.S. Brenner, J.R. Low, Jr., "An FIM-Atom Probe Study of the Precipitation of Copper from Iron-1.4 At. Pct Copper. Part I: Field-Ion Microscopy", *Metall. Trans.*, 4 (1973) 2363-2369.
63. E. Povoden-Karadeniz, Diffusion database mc\_fe.ddb, version 2.005, 2014.
64. Y.U. Heo, Y.K. Kim, J.S. Kim, J.K. Kim, "Phase transformation of Cu precipitates from bcc to fcc in Fe-3Si-2Cu alloy", *Acta Mater.*, 61 (2013) 519-528.
65. E. Kozeschnik, J. Svoboda, F.D. Fischer, "Shape factors in modeling of precipitation", *Mater. Sci. Eng. A*, 441 (2006) 68-72.
66. B. Sonderegger, E. Kozeschnik, "Interfacial Energy of Diffuse Phase Boundaries in the Generalized Broken-Bond Approach", *Metall. Mater. Trans. A*, 41 (2010) 3262-3269.
67. F. Soisson, C.C. Fu, "Cu-precipitation kinetics in alpha-Fe from atomistic simulations: Vacancy-trapping effects and Cu-cluster mobility", *Phys. Rev. B*, 76 (2007) 1-12.
68. A.V. Barashev, A.C. Arokiam, "Monte Carlo modelling of Cu atom diffusion in alpha-Fe via the vacancy mechanism", *Phil. Mag. Lett.*, 86 (2006) 321-332.

69. P. Warczok, J. Zenisek, E. Kozeschnik, "Atomistic and continuums modeling of cluster migration and coagulation in precipitation reactions", *Comp. Mater. Sci.*, 60 (2012) 59-65.
70. K. Binder, D. Stauffer, "Statistical theory of nucleation, condensation and coagulation", *Adv. Phys.*, 25 (1976) 343-396.
71. K. Binder, "Theory for the dynamics of clusters: II. Critical diffusion in binary systems and the kinetics of phase separation", *Phys. Rev. B*, 15 (1977) 4425-4447.
72. S.I. Golubov, A. Serra, Yu.N. Osetsky, A.V. Barashev, "On the validity of the cluster model to describe the evolution of Cu precipitates in Fe-Cu alloys", *J. Nucl. Mater.*, 277 (2000) 113-115.
73. M. Perez, F. Perrard, V. Massardier, X. Kleber, V. Schmitt, A. Deschamps, "Low Temperature Solubility Limit of Copper in Iron", *Mater. Sci. Forum*, 500-501 (2005) 631-638.
74. R. Radis, E. Kozeschnik, "Numerical simulation of NbC precipitation in microalloyed steel", *Model. Sim. Mater. Sci. Eng.*, 20 (2012) 055010 (15 p.).
75. G. Stechauner, E. Kozeschnik, "Assessment of substitutional self-diffusion along short-circuit paths in Al, Fe and Ni", *CALPHAD*, 47 (2014) 92-99.

# Paper five

Early Stages of Cu Precipitation in 15-5 PH Maraging Steel Revisited  
- Part II: Thermokinetic Simulation

Georg Stechauner, Sophie Primig and Ernst Kozeschnik

Steel Research International

2016, in print.

# Early Stages of Cu Precipitation in 15-5 PH Maraging Steel Revisited – Part II: Thermokinetic Simulation

Georg Stechauner\*, Sophie Primig, Ernst Kozeschnik

G. Stechauner\*

Materials Center Leoben Forschung GmbH, Roseggerstraße 12, 8700 Leoben, Austria

georg.stechauner@tuwien.ac.at

Dr. S. Primig

Christian Doppler Laboratory Early Stages of Precipitation, Department of Physical Metallurgy and Materials Testing, Montanuniversität Leoben, Franz-Josef Straße 18, 8700 Leoben, Austria;

School of Materials Science & Engineering, UNSW Australia, UNSW Sydney NSW 2052 Australia

Prof. Dr. E. Kozeschnik

Christian Doppler Laboratory Early Stages of Precipitation, Institute of Materials Science and Technology, Vienna University of Technology, Getreidemarkt 9, 1060 Vienna, Austria

## Keywords

Maraging steel, aging, precipitation, thermo-kinetic modeling, DSC simulation

## Abstract

In this part II of our investigation of Cu-precipitation in 15-5 PH steel, we complement the experimental analysis of part I with thermokinetic modeling and simulation to aid in the interpretation of processes and mechanisms involved in the two precipitation reactions between around 300 and 500°C. The kinetic simulations are founded on extended classical nucleation theory, a mean-field model for precipitate growth, a predictive model for interface energy calculation and CALPHAD-based Gibbs-energy and mobility databases. Our modeling supports the interpretation that the first peak in the continuous DSC signal is the result of nucleation of Fe-rich Cu clusters, which leads to a partial Cu-depletion of the matrix and produces the first observed DSC signal. The second DSC peak has its origin in the Cu-enrichment of precipitate clusters above approximately 500°C and the associated enthalpy change. A quantitative reproduction of both exothermic reactions is performed within the framework of the thermokinetic simulation.

## 1. Introduction

Thermokinetic simulation and modeling in metals and metal processing is a valuable tool in development of high-end materials and it has shown its practical merits increasingly in the last decades. Recent advances in the simulation and modeling community allow both, quantitative and qualitative reproduction of precipitation processes.<sup>[1,2]</sup> It has been shown recently, for various 6xxx Al-alloys, that thermokinetic simulation can substantially aid in interpretation of complex and

overlapping peaks in differential scanning calorimetry (DSC) analysis based on the simulated evolution of the essential state parameters radius, number density and phase fraction of contributing precipitate reactions and the matrix chemical composition.<sup>[3,4]</sup>

The 15-5 PH steel investigated in the present work is a maraging steel with low carbon content and Cu as major precipitate-forming element. The experimental analysis with continuous heating DSC, dilatometry, hardness testing and atom probe tomography has been topic of part I of this paper.<sup>[5]</sup> The relevant literature on PH steels is outlined there and, for this reason, not duplicated in this second part. In contrast to the isothermal heat treatments that were performed in refs.<sup>[6,7]</sup> the continuous heating ramp provides additional information on the precipitation mechanisms at lower temperature and allows for a differentiation in the sequence of occurring mechanisms within a single simulation run. The first reaction, which is observed at temperatures around 300°C, has been previously explained on basis of an assumed formation of Cu-clusters, see refs.<sup>[8,9]</sup> These authors claim that, due to the estimated precipitate radii of 0.35-0.5 nm, any experimental confirmation of the existence of these clusters is inherently difficult. These studies also delivered that, in a subsequent DSC run, the first peak can be removed by prolonged annealing above 300°C.<sup>[10]</sup> Since all clusters have already formed in the first run, there is no driving force left for further reactions in a re-run. At around 500°C, a second, more pronounced exothermic reaction has been observed, which was explained by mere growth of the existing clusters.<sup>[9,11]</sup>

In the present work, we study the early stages of precipitation responsible for the two exothermic DSC reactions by thermokinetic simulation. To support the findings obtained in part I,<sup>[5]</sup> and to aid in interpretation of the experimental results, we apply computational simulation of the full-process heat treatments depicting the DSC experiments from solution annealing over quenching to annealing with a constant heating rate. The results comprise of an analysis of thermodynamic properties, such as Gibbs energy of phases, driving force for precipitation, as well as molar enthalpy of phases and thermokinetic properties, such as phase fraction, radius or number density of the precipitate phase. The calculations are performed with the thermokinetic simulation software MatCalc,<sup>[12]</sup> utilizing a simulation input parameter set recently developed in ref.<sup>[13]</sup>

## 2. Simulation

The experimental analysis consists of DSC heating experiments, atom probe tomography, as well as mechanical testing, and it is discussed in detail in part I of this work.<sup>[5]</sup> Only parts of it are briefly

recapitulated in this section as far as they are related to the DSC measurements relevant for our thermokinetic analysis.

The chemical composition of the testing material and the elements considered in the simulation are shown in **Table 1**. It is well-known <sup>[14]</sup> that the as-quenched condition of 15-5 PH steel contains NbC and complex  $M_7C_3$  precipitates with sizes of approximately 50 and 250 nm, respectively. Due to their comparably low volume fraction, no conceivable impact on the DSC signal is expected to arise from these particles. Consequently, we use a simplified chemical composition as given in Table 1 for the merit of computational efficiency and ease of interpretation of results.

**Table 1** - Chemical composition of 15-5 PH steel composition (in wt.-%).

	C	Si	Mn	Cr	Ni	Cu	Nb	Fe
Experimental	0.04	0.3	0.6	14.9	5.1	3.3	0.3	bal.
Simulation	-	0.3	0.6	14.9	5.1	3.3	-	bal.
Simulation at.%	-	0.6	0.6	15.8	4.8	2.9	-	bal.

The simulations are performed with the thermokinetic software package MatCalc (version 5.62 release 1.001). The relevant input quantities for the precipitation kinetics simulation are either given by experiment or are derived and calculated from independent thermodynamic <sup>[15]</sup> and diffusion <sup>[16]</sup> databases. Nucleation of precipitates is described within the framework of extended multi-component classical nucleation theory <sup>[17,18]</sup> and a mean-field model for precipitate growth. <sup>[19,20]</sup> The simulation methodology has been described several times, see, e.g., <sup>[21,22]</sup> and our reference work <sup>[13]</sup> describing the parameterization of the Cu-precipitation kinetics simulation.

Based on this approach, the total Gibbs energy of the system is expressed in terms of the sum of energy contributions from the matrix, the precipitates and the interfaces. Applying the thermodynamic extremal principal, that a system will always evolve along the kinetic pathway, where the production of entropy is maximum, <sup>[23]</sup> Svoboda et al. <sup>[19,20]</sup> defined three processes to dissipate the excess Gibbs energy during kinetic evolution. These are the migration of the precipitate/matrix interface, as well as diffusion inside and outside the precipitates. After some algebra, a linear system of equations is obtained for the rates of radius and composition of each precipitate. Time integration of kinetic parameters is performed with standard techniques and it delivers the evolution of the entire thermodynamic system.

A key parameter, when dealing with nucleation, is the interface energy between matrix and precipitate. Since this quantity is hardly accessible on an experimental basis, in the present work, we

utilize a composition- and temperature-dependent approach introduced by Sonderegger and Kozeschnik,<sup>[24]</sup> originally developed for sharp and planar interfaces and rooted in an elaborated counting of broken-bond energies across the interfaces. In addition, we fully account for the interface curvature effect  $\gamma(r)$  of small precipitates<sup>[25]</sup> as well as the effect of dilute interfaces at elevated temperatures  $S(T/T_c)$ , which introduces entropic contributions in the interfacial energy coming from atomic mixing across the interface.<sup>[26]</sup> The equation for the analytical solution to the interface energy is shown in **Equation 1**

$$\chi = \gamma(r) \cdot S(T/T_c) \cdot \frac{n_s z_{s,eff}}{N_A z_{L,eff}} \cdot \Delta H_{sol}, \quad (1)$$

where  $n_s$  is the number of atoms per unit interfacial area,  $z_{s,eff}$  is the effective number of broken bonds across the interface,  $N_A$  is Avogadro's number,  $z_{L,eff}$  is the effective coordination number and  $\Delta H_{sol}$  is the enthalpy of solution, which is obtained from the thermodynamic properties of the system.

To describe precipitation kinetics of Cu in Fe consistently, additional mechanisms that go beyond the conventional simulation approach are considered here, for instance, the effect of cluster diffusion acceleration as reported by Soisson et al.<sup>[27]</sup> This mechanism is realized in our simulations with the particle coalescence Ansatz of Warczok et al.<sup>[28]</sup> The Monte-Carlo simulations performed by Soisson and co-workers<sup>[27]</sup> showed that vacancies preferably migrate to the matrix/precipitate interface, increasing the cluster mobility up to two orders of magnitude, thus leading to this prominent effect of particle coalescence. Another important precipitation mechanism in the Fe-Cu system is the transformation sequence from coherent bcc to semi-coherent 9R to incoherent fcc crystal structure as reported by Othen et al.<sup>[29]</sup> These authors observe the size of the smallest particles in transmission electron microscopy with radii of approximately 4 nm. These particles already show the characteristic martensitic-twinned structure. Even smaller Cu-particles were observed by atom probe tomography in part I of this manuscript as well as elsewhere<sup>[30]</sup> and are assumed to be of coherent bcc crystal structure. In our simulation, we apply a radius-dependent transformation, where all particles transform within a specific threshold radius between 2.5-3.5 nm for bcc-9R, and 6-10 nm for 9R-fcc transformation, respectively.

Substantial effort has been made in the last decades to characterize the initial chemical composition of Cu clusters of being either almost pure Cu or rather Fe-rich.<sup>[31]</sup> In our simulations, we utilize a thermodynamic model for prediction of the “most likely” nucleus composition<sup>[32]</sup> based on the composition-dependent evaluation of the minimum nucleation energy barrier to be able to forecast the chemical composition of the very early Cu precipitates as shown in **Figure 1**. By applying

Boltzmann statistics, the energy barrier can be converted into a nucleation probability, which is maximum for a minimal nucleation energy.

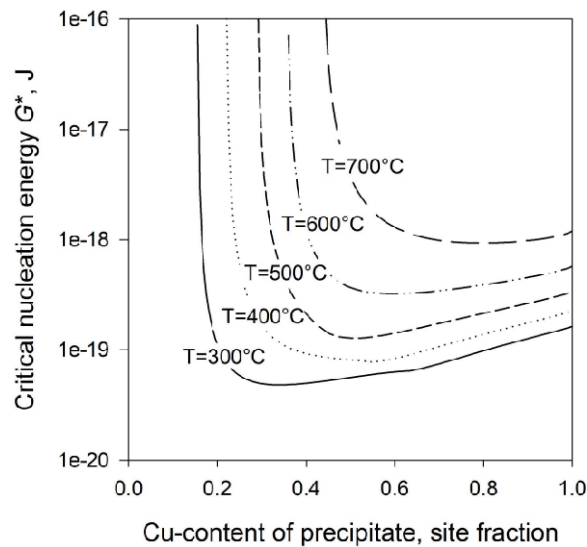


**Figure 1** - Calculated nucleation energies as a function of Cu-content from 300 to 700°C.

The heat treatment used in the simulation reproduces the experimental DSC cycle applied in part I, consisting of solution annealing at 1050°C for 30 min and a quench to room temperature leading to a fully martensitic microstructure. The martensite start temperature shows a weak dependency from the quenching rate <sup>[5]</sup> and a representative value of 150°C is used in the present work. In the actual DSC run, the specimens are heated from room temperature to 600°C with a heating rate of 15 K/min. We apply the Sherstnev–Lang–Kozeschnik – ABC model <sup>[33]</sup> to simulate the tempering of fresh martensite and the associated decrease in dislocation density.

Based on the present approach and with knowledge of the total system Gibbs energy, MatCalc monitors all processes, such as, nucleation, growth, coarsening, dissolution and transformation of all precipitates, on basis of the relevant state parameters and stores these with respect to time. From this information, the thermo-chemical properties of the system, matrix and precipitates, are evaluated and are used to calculate the heat flow, respectively the DSC curve. This state parameter-based approach was recently elaborated in detail by Lang et al. <sup>[34]</sup>

### 3. Results and Discussion

The precipitation kinetics simulation is performed in accordance with the real DSC cycle described in section 2. The results are summarized in **Figure 2**. Figure 2a to 2d show the evolution of the

thermokinetic state parameters, phase fraction, radius, and number density together with the DSC signal.

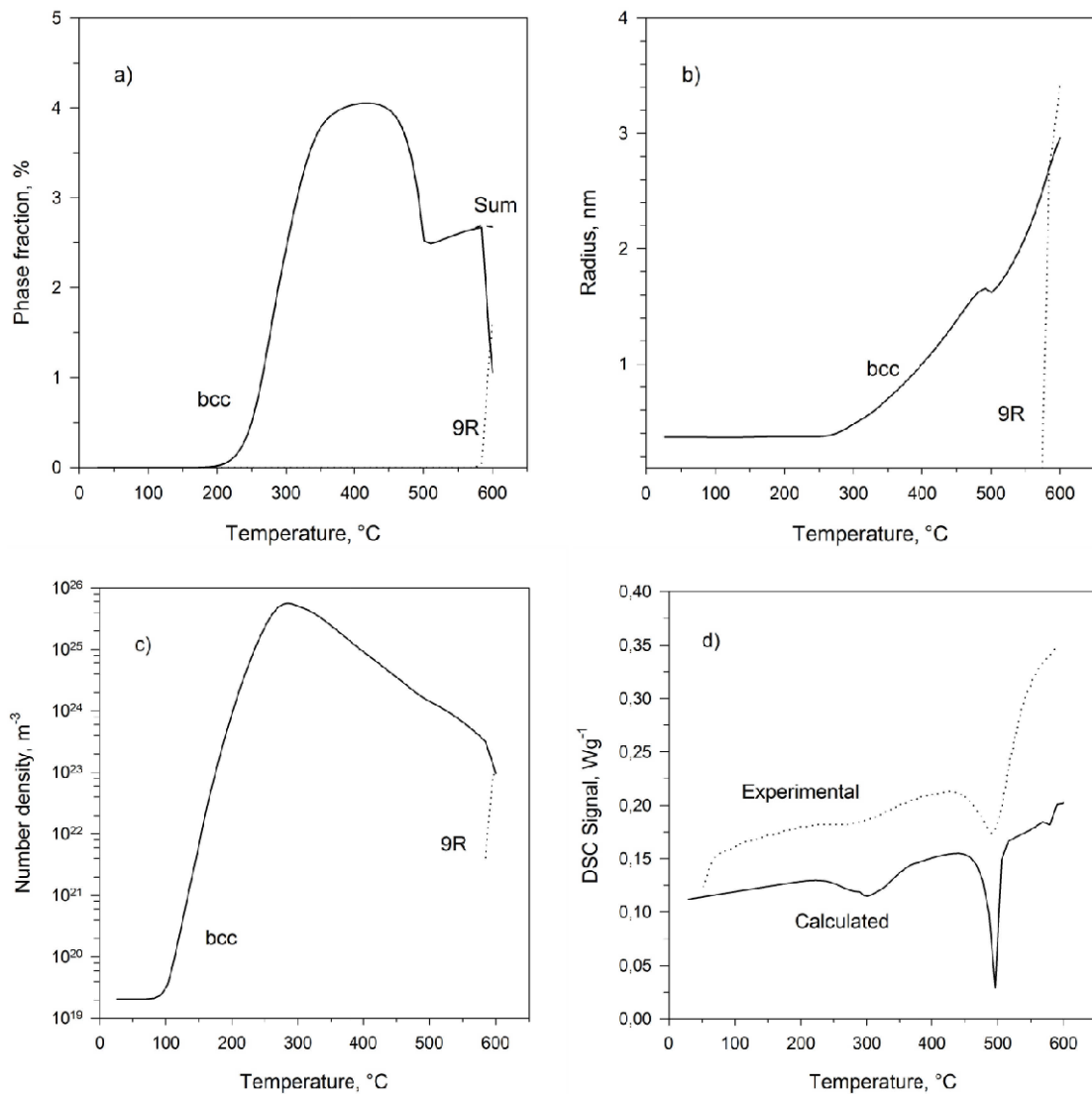


**Figure 2.** Thermokinetic parameter triplet of coherent bcc, semi-coherent 9R and total sum of phases for a) phase fraction, b) radius and c) number density. Calculated and experimental DSC curves are shown in d).

The simulation indicates that a certain amount of bcc-Cu nucleation already occurs during quenching from austenitization after passing the martensitic transformation start temperature of 150 °C. The calculated number density of these initial clusters is comparatively small with  $10^{19} \text{ m}^{-3}$  compared to the value of  $10^{25} \text{ m}^{-3}$  in the precipitation maximum. No notable effect on the Cu precipitate phase fraction is therefore observed.

To simulate the DSC signal, we use the first derivative of the system enthalpy with respect to temperature, which is numerically evaluated within our simulation framework, and multiply it by the

heating rate. Since no baseline correction is applied, a vertical shift between the experimental and calculated data is observed. The corresponding curve is displayed in Figure 2d.

### 3.1 Peak 1

In part I of this work,<sup>[5]</sup> the first exothermic DSC peak has been attributed to the nucleation and growth processes of Cu-rich clusters forming in the supersaturated Fe-rich matrix. Experimentally, a slight increase in the segregation parameter between 150 and 300°C has been observed,<sup>[5]</sup> which would indicate some initial phase separation process taking place in this temperature range. However, no clear and distinct interpretation could be derived purely from the experimental results, since the expected and modeled cluster sizes are too close to the detection limit of the atom probe tomography (APT) device. In this context, the thermokinetic simulation provides important additional information.

The phase fraction and number density plots in Figure 2 suggest that no significant amount of precipitation is present below 200°C and, therefore, the majority of Cu atoms is homogeneously distributed in the matrix. With increasing temperature, between 200-400°C, the simulation predicts massive nucleation of Fe-rich Cu clusters. This early precipitation/clustering process is accompanied by a decrease of the amount of free Cu atoms in the matrix and it represents the source for the heat flow signal in the first exothermic reaction.

**Figure 3** displays the calculated molar enthalpies of matrix, precipitate and the entire system as well as their derivatives with respect to time. The latter are directly related to the heat flow. The system enthalpy is given by the phase fraction-weighted sum of enthalpies of matrix and precipitate. These quantities are shown in Figure 3a. In the absence of precipitation below approximately 200°C, the system enthalpy is practically identical to the enthalpy of the matrix. With the onset of cluster formation, the matrix enthalpy is reduced. Partially, this effect is compensated by the appearance of Cu-clusters with higher enthalpy values, such that the net enthalpy value falls somewhere in between the individual phase enthalpies of matrix and Cu-precipitate. The occurrence of the second exothermic peak is discussed later in section 3.2.

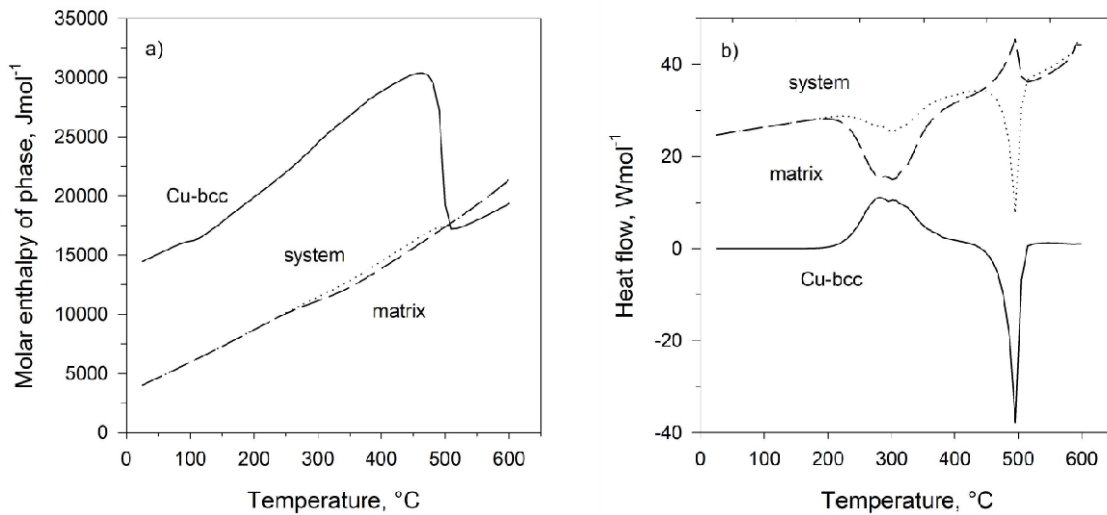


**Figure 3** - a) Molar enthalpy of precipitate phase, ferrite matrix, and the total system, and b) the heat flow of phase, with respect to the actual phase fractions.

An important quantity providing additional information to the present analysis is the chemical composition evolution of the Cu precipitates. For a prediction of the initial composition of the bcc-Cu nuclei, the minimum  $G^*$  concept is applied as developed in ref.<sup>[32]</sup> Accordingly, the chemical composition of the precipitate is determined in such a way that the nucleation barrier  $G^*$  adopts a minimum value. It is further assumed that the probability for observing particles with this composition is maximum because they exhibit the highest nucleation rates. In the temperature range of the DSC experiment, where nucleation of Cu-precipitates begins, the minimum  $G^*$  concept delivers compositions with an Fe content being slightly higher or equal to the Cu content. The predicted composition evolution for Fe and Cu is depicted in **Figure 4**.

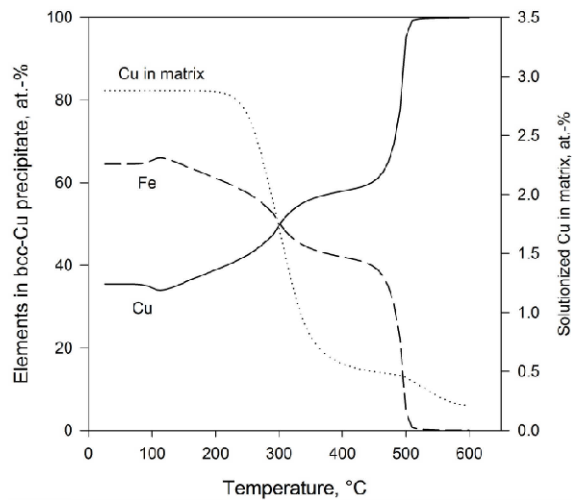


**Figure 4** - Chemical composition of the Cu nucleus as calculated from the minimum  $G^*$  concept and its evolution to almost pure Cu at higher temperatures. The dotted curve shows the matrix Cu content.

The prediction that the early bcc-Cu precipitates are heavily enriched in Fe has significant impact on the evolution of the cluster phase fraction. Figure 4 also displays the evolution of the free Cu content in the matrix. Starting at 3 at.-%, the Cu content quickly decreases to values around 0.5 at.-%, thus indicating that the majority of Cu atoms will be bound inside the clusters. Since the early precipitates contain approximately the same number of Fe and Cu atoms, the total phase fraction of Cu-precipitates can reach a maximum of around 4% (Figure 2a). In later stages of the precipitation reaction, the Fe content in the precipitates drastically reduces and the phase fraction of precipitates simultaneously decreases again.

### 3.2 Peak 2

In the higher temperature region of the DSC heating cycle, ranging from approximately 400–600°C, a pronounced exothermic reaction peak is observed at around 500°C (Figure 2d). In literature, this peak is persistently attributed to the growth of pre-existing clusters.<sup>[9,11]</sup> In contrast, in part I of this work,<sup>[5]</sup> we propose that the evolution of precipitates from Fe-rich Cu clusters into thermodynamically favorable almost pure Cu precipitates provides the main source for this signal. This interpretation is supported by the results of the thermokinetic simulations.

A first strong indication in support of this explanation is the fact that the majority of free Cu atoms becomes bound in the clusters already in the first reaction at around 300°C. Thereby, the free Cu content decreases from 3 at.-% to close to 0.5 at.-% (Figure 4). The remaining free Cu atoms could hardly cause a sufficiently strong DSC signal, much stronger than the first one, simply by growth of the

existing clusters. Instead, the thermokinetic simulation offers another explanation for the occurrence of the second peak. Figure 4 shows that the Fe-rich Cu-precipitates formed at lower temperature undergo a transition into almost pure Cu particles at around 500°C. This corresponds well with the temperature where the second exothermic DSC peak is observed. In the course of this process, the enthalpy of the bcc-Cu precipitates drastically changes to significantly lower values (Figure 3). Although the phase fraction of precipitates is only around 3%, this significant enthalpy change is nevertheless sufficient to produce a sharp peak in the integral signal observed for the entire system.

In the analysis of the chemical composition evolution of the Cu-precipitates, the composition of the nucleus is determined on basis of the minimum  $G^*$  concept. Once the precipitates have nucleated, they are grouped into  $n$  size classes and their further evolution is described on basis of the SFFK model,<sup>[19,20]</sup> which delivers the rates of radius and chemical composition evolution for each precipitate as a function of temperature, chemical potentials as well as atomic diffusivities. Within an individual size class, all precipitates, characterized by their number density, share the same properties in terms of radius and chemical composition. Whereas the diffusion coefficient of Cu in the matrix is the main parameter determining the growth rate of Cu particles, the diffusivity of Cu inside the precipitate is the essential parameter controlling the change of chemical composition of the precipitates. Unfortunately, the diffusivity of Cu in bcc Fe-Cu alloys is unknown, which is why we estimate this quantity on basis of the diffusion coefficient of Cu in bcc-Fe. The exact value of the Cu-diffusivity in the precipitates can then be expressed in terms of the “inner particle diffusion coefficient factor” (IPDCF), relating the diffusivity inside the precipitate to the diffusivity of elements in the matrix.

In **Figure 5**, a variation of the IPDCF in a range from 0.01 to 10 is presented. Apparently, the value of the IPDCF impacts the peak temperature of the second reaction. Lower diffusivity values shift the peak to higher temperatures, whereas higher values allow the transition from Fe-rich to Fe-poor precipitates to occur earlier at lower temperature. The best correlation between experiment and simulation is obtained with an IPDCF of 0.3. This value is close to the expected value in the order of the diffusion coefficient of Cu in the bcc Fe-matrix. Variation of the IPDCF does not severely impact the shape and height of the exothermal peak.

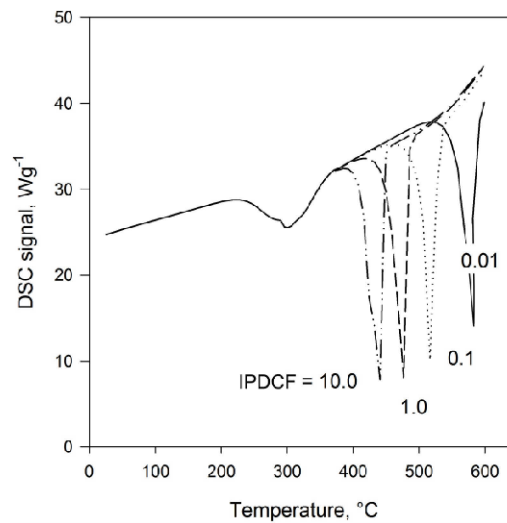


**Figure 5** - Simulation of DSC signal with a variation of the inner particle diffusion coefficient factor.

In our analysis, we use a size dependent transformation condition, where bcc-Cu particles exceeding a critical radius of 2.5 nm are assumed to transform into 9R-Cu structure. Figure 2b indicates that this condition is not met until 580°C is reached in the DSC experiment. This temperature is well above the 500°C of the second exothermic peak. We, therefore, conclude that the structural transformation is not responsible for the second exothermic transformation peak. No transformation into fcc-Cu structure is observed here, as the lower radius threshold for transformation of 6 nm is not reached in our simulations.

### **3.3 Impact of quenching rate**

An important and supplementary question raised in part I of our work is related to the possible influence of the quenching rate from austenitization to room temperature before DSC testing on the appearance of the first reaction peak. Since the diffusion kinetics of substitutional elements is governed by the vacancy exchange mechanism, an excess of thermal vacancies frozen in during fast quenching (“quenched-in vacancies”) would potentially impact the diffusion rates at low temperature. Interestingly, corresponding experiments <sup>[5]</sup> showed practically no influence of the quenching rate on the phase decomposition kinetics.

In the kinetic simulations performed in this context, the vacancy annihilation dynamics are simulated on basis of the FSAK model, <sup>[35]</sup> which has previously been successfully applied to predictions of the excess vacancy evolution during and after quenching of various Al-base alloys. <sup>[4,34,36]</sup> While a certain density of structural vacancies is always present in crystalline materials according to thermal

equilibrium, and this density is reflected in the corresponding diffusion coefficients, the FSAK-model predicts the generation and annihilation of vacancies under non-equilibrium conditions, such as rapid cooling, as a function of dislocation density and grain size.

In **Figure 6**, the calculated equilibrium and excess vacancy density for 1 and 100 K/s quenching rates with subsequent DSC heating is shown. The discontinuity at 150°C is a consequence of the assumed martensitic transformation occurring at this temperature. This threshold is chosen in accordance with experimental evidence and keeping in mind that the simulations in MatCalc are performed with respect to a single representative volume element. The temperature, where the austenite precipitation domain is switched to martensite, corresponds to 50% transformed austenite volume fraction.

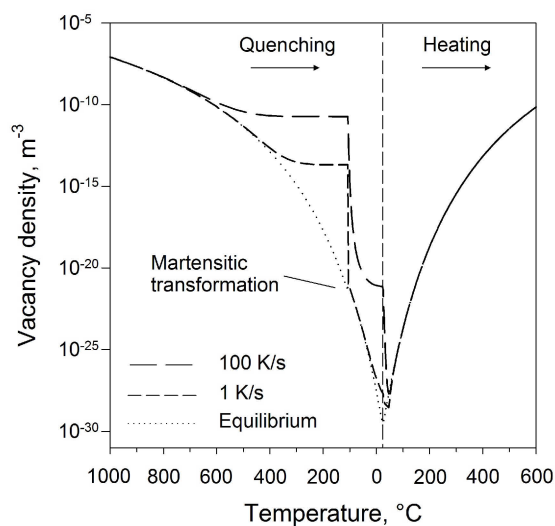


**Figure 6** - Calculated evolution of equilibrium and excess vacancy densities for quenching at 1 and 100 K/s.

While the equilibrium vacancy concentration curves are inherently identical for both quenching rates, the kinetic simulation still predicts significant differences in vacancy evolution for fast and slow cooling. Rapid cooling from austenitization at 100 K/s leads to a retarded annihilation and longer average lifetime of excess vacancies as compared to cooling at 1 K/s. At the higher quenching rate, more excess vacancies remain frozen-in, and are still present at room temperature, thus facilitating a more pronounced acceleration of diffusion kinetics. However, the total number density of Cu-clusters formed for both quenching conditions is calculated to be rather small, i.e.,  $3.6 \cdot 10^{21} \text{ m}^{-3}$  at 1 K/s and  $8.6 \cdot 10^{19} \text{ m}^{-3}$  at 100 K/s, when reaching room temperature. These values correspond to phase fraction values of approximately  $7 \cdot 10^{-5}$  and  $5 \cdot 10^{-7} \%$ . We thus expect no conceivable impact on the DSC signal and practically the full clustering/precipitation potential for the

subsequent DSC experiment in both cases. Moreover, upon reheating in the DSC cycle, annihilation of excess vacancies and leveling out of the diffusion acceleration take place for both cases below 100°C. Since all these processes occur well before the first experimentally observed exothermic DSC reaction, the observations of part I of this work<sup>[5]</sup> are supported and no conceivable influence of the DSC signal on the quenching rate is thus confirmed.

### 3.4 Thermal stability of clusters

Finally, in part I of this work,<sup>[5]</sup> the influence of pre-annealing at 300°C for 12 and 24h on the subsequent DSC run has been investigated. The aim of this experiment has been the identification of the cluster stability responsible for the second peak. A similar study was performed by Sano and Maehara<sup>[10]</sup> with pre-annealing temperatures of 430 and 550°C for 6 and 30 minutes, respectively. The work of Sano and Maehara<sup>[10]</sup> is qualitatively reproduced in **Figure 7**, displaying the calculated DSC signal for the three conditions investigated there. An arbitrary y-axis offset is used in the plot for the sake of clarity.

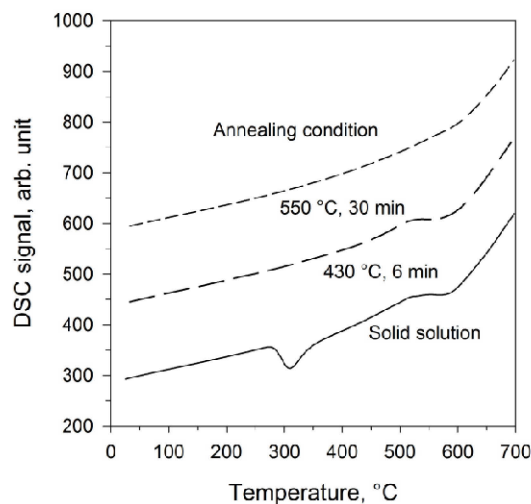


**Figure 7** - Simulated DSC signals for different annealing conditions as performed in ref. [10]

Performing a simulated DSC run from the solutionized (quenched) state produces the same two exothermic reactions as reported in sections 3.1 and 3.2 of the present work (see curve labeled with “Solid solution”). We assume that the evolution of the thermokinetic parameter triplet of phase fraction, radius and number density is qualitatively comparable to the evolution of parameters depicted in Figure 2, with a slight shift of peaks to higher temperatures due to a lower nominal Cu content in ref.<sup>[10]</sup>

The simulation of pre-annealing at 430°C for 6 minutes indicates that the formation of Fe-rich clusters is completed at approximately 280°C, compare Figure 2, and the occurrence of the first DSC peak in the subsequent DSC run is effectively suppressed (Figure 7). Interestingly, the stability of the Fe-rich clusters is rather high even at the pre-annealing temperature of 430°C. In the simulation, the transformation of clusters into Cu-rich precipitates does not occur before several hours of pre-annealing. Thus, its impact on the second DSC peak is practically insignificant, both in the experimental analysis as well as in the thermokinetic simulation.

As a third starting condition, Sano and Maehara <sup>[10]</sup> pre-annealed the samples at 550°C for 30 minutes. Our simulations confirm nucleation and growth of Cu precipitates at 280°C, identical to the previous situation. The clusters transform into the stable Cu-rich precipitates at approximately 500°C. This process is shown in detail in Figure 4 for the example of the steel grade investigated in part I. Pre-annealing at 550°C, thus, produces fully transformed Cu precipitates in a matrix with no further nucleation potential. Consequently, no exothermic reactions are observed at all in the subsequent DSC run.

#### **4. Conclusions**

On the basis of thermo-kinetic simulations, the underlying mechanisms governing Cu-clustering and precipitation in the course of calorimetric analyses with DSC in a PH 15-5 steel are studied on basis of thermokinetic simulations. The results obtained in part I of the present work, and substantiated in the simulations of part II, are:

- In a DSC run with constant heating rate from the solutionized state, two exothermic reactions are identified at approximately 300 and 500°C.
- In the range of the first peak, nucleation and growth of Fe-rich Cu clusters / precipitates occurs.
- The transformation of these precipitates into almost pure Cu configuration takes place in the temperature range where the second DSC peak is observed.
- The quenching rate prior to the actual DSC run has practically no influence on the experimentally observed and calculated precipitation kinetics. All quenched-in excess vacancies are annihilated well before the first peak.
- Pre-annealing at temperatures between the two reaction peaks leads to a removal of the first exothermic signal in a subsequent DSC run. Pre-annealing above the temperature of the

second peak leads to a removal of both peaks. This is observed in both, experiment and computational analysis.

### Acknowledgements

Financial support by the Austrian Federal Government (in particular from Bundesministerium für Verkehr, Innovation und Technologie and Bundesministerium für Wissenschaft, Forschung und Wirtschaft) represented by Österreichische Forschungsförderungsgesellschaft mbH and the Styrian and the Tyrolean Provincial Government, represented by Steirische Wirtschaftsförderungsgesellschaft mbH and Standortagentur Tirol, within the framework of the COMET Funding Programme is gratefully acknowledged.

### References

1. R. Radis and E. Kozeschnik, "Kinetics of AlN precipitation in microalloyed steel", *Model. Simul. Mater. Sci. Eng.*, 18 (2010) 055003 (16pp).
2. R. Schnitzer, R. Radis, M. Nöhrer, M. Schober, R. Hochfellner, S. Zinner, E. Povoden-Karadeniz, E. Kozeschnik, H. Leitner, "Reverted austenite in PH 13-8 Mo maraging steels", *Mater. Chem. Phys.*, 122 (2010) 138-145.
3. A. Falahati, E. Povoden-Karadeniz, P. Lang, P. Warczok, E. Kozeschnik, "Thermo-kinetic computer simulation of differential scanning calorimetry curves of AlMgSi alloys: Dedicated to Professor Dr. H.-P. Degischer on the occasion of his 65th birthday", *Int. J. Mater. Res.*, 101 (2010) 1089-1096.
4. P. Lang, E. Povoden-Karadeniz, A. Falahati, E. Kozeschnik, "Simulation of the effect of composition on the precipitation in 6xxx Al alloys during continuous-heating DSC", *J. Alloy. Compd.*, 612 (2014) 443-449.
5. S. Primig, G. Stechauner, E. Kozeschnik, "Early Stages of Cu Precipitation in 15-5 PH Maraging Steel Revisited – Part I: Experimental Analysis ", *Steel Res. Int.*, 2016, in print.
6. M. Perez, M. Dumont, D. Acevedo-Reyes, "Implementation of classical nucleation and growth theories for precipitation", *Acta Mater.*, 56 (2008) 2119–2132.
7. I. Holzer, E. Kozeschnik, "Computer simulation of the yield strength evolution in Cu-precipitation strengthened ferritic steel", *Mater. Sci. Eng. A*, 527 (2010) 3546–3551.
8. H.R. Habibi-Bajguirani, "Mechanism of austenitic transformation in the martensitic stainless steel of type PH 15-5", *J. Phys. IV*, 4 (1994) 123-126.

9. S. Primig, H. Leitner, "Transformation from continuous-to-isothermal aging applied on a maraging steel.", *Mater. Sci. Eng. A*, 527 (2010) 4399-4405.
10. N. Sano, Y. Maehara, "Initial stage of copper precipitation in Cu-added ultra-low carbon steel", *J. Japan Inst. Met.*, 60 (1996) 261-268.
11. N. Maruyama, M. Sugiyama, T. Hara, H. Tamehiro, "Precipitation and phase transformation of copper particles in low alloy ferritic and martensitic steels", *Mater. T. JIM*, 40 (1999) 268-277.
12. <http://www.matcalc.at>
13. G. Stechauner, E. Kozeschnik, "Thermo-kinetic modeling of Cu precipitation in  $\alpha$ -Fe", *Acta Mater.*, 100 (2015) 135-146.
14. H.R. Habibi-Bajguirani, "The effect of ageing upon the microstructure and mechanical properties of type 15-5 PH stainless steel", *Mater. Sci. Eng. A*, 338 (2002) 142-159.
15. E. Povoden-Karadeniz, *Thermodynamic database*, MatCalc version v2.008.
16. E. Povoden-Karadeniz, *Diffusion database*, MatCalc version v2.005.
17. K.C. Russell, "Nucleation in solids: the induction and steady state effects", *Adv. Colloid Interfac.*, 13 (1980) 205-318.
18. E. Kozeschnik, *Modeling solid-state precipitation*, first edition, Momentum Press, New York, 2013, pp. 37-104.
19. J. Svoboda, F.D. Fischer, P. Fratzl, E. Kozeschnik, "Modelling of Kinetics in Multi-Component Multi-Phase System with Spherical Precipitates I. - Theory", *Mater. Sci. Eng. A*, 385 (2004) 166-174.
20. E. Kozeschnik, J. Svoboda, P. Fratzl, F.D. Fischer, "Modelling of Kinetics in Multi-Component Multi-Phase Systems with Spherical Precipitates II. - Numerical Solution and Application", *Mater. Sci. Eng. A*, 385 (2004) 157-165.
21. R. Radis, M. Schaffer, M. Albu, G. Kothleitner, P. Pölt, E. Kozeschnik, " Multimodal size distributions of  $\gamma'$  precipitates during continuous cooling of UDIMET 720 Li", *Acta Mater.*, 57 (2009) 5739-5747.
22. E. Povoden-Karadeniz, E. Kozeschnik, "Simulation of precipitation kinetics and precipitation strengthening of B2-precipitates in martensitic PH 13–8 Mo steel.", *ISIJ Int.*, 52 (2012) 610-615.
23. L. Onsager, "Reciprocal relations in irreversible processes. I", *Phys. Rev.*, 37 (1931) 405.
24. B. Sonderegger, E. Kozeschnik, "Generalized Nearest-Neighbor Broken-Bond Analysis of Randomly Oriented Coherent Interfaces in Multicomponent Fcc and Bcc Structures", *Metall. Mater. Trans. A*, 40 (2009) 499-510.

25. B. Sonderegger, E. Kozeschnik, "Size dependence of the interfacial energy in the generalized nearest-neighbor broken-bond approach", *Scripta Mater.*, 60 (2009) 635-638.
26. B. Sonderegger, E. Kozeschnik, "Interfacial Energy of Diffuse Phase Boundaries in the Generalized Broken-Bond Approach", *Metall. Mater. Trans. A*, 41 (2010) 3262-3269.
27. F. Soisson, C.C. Fu, "Cu-precipitation kinetics in alpha-Fe from atomistic simulations: Vacancy-trapping effects and Cu-cluster mobility", *Phys. Rev. B*, 76 (2007) 1-12.
28. P. Warczok, J. Zenisek, E. Kozeschnik, "Atomistic and continuums modeling of cluster migration and coagulation in precipitation reactions", *Comp. Mater. Sci.*, 60 (2012) 59-65.
29. Othen, M.L. Jenkins, G.D.W. Smith, "High-resolution electron microscopy studies of the structure of Cu precipitates in alpha-Fe", *Phil. Mag. Lett.*, 70 (1994) 1-24.
30. R.A. Karnesky, D. Isheim, D.N. Seidman, "Direct measurement of two-dimensional and three-dimensional interprecipitate distance distributions from atom-probe tomographic reconstructions", *Appl. Phys. Lett.*, 91 (2007) 013111.
31. M.E. Fine, J.Z. Liu, M.D. Asta, "An unsolved mystery: The composition of bcc Cu alloy precipitates in bcc Fe and steels", *Mat. Sci. Eng. A*, 463 (2007) 271-274.
32. E. Kozeschnik, "Thermodynamic prediction of the equilibrium chemical composition of critical nuclei: Bcc Cu precipitation in  $\alpha$ -Fe", *Scripta Mater.*, 59 (2008) 1018-1021.
33. P. Sherstnev, P. Lang, E. Kozeschnik, "Treatment of simultaneous deformation and solid-state precipitation in thermo-kinetic calculations", in: *Proceeding of 6th ECCOMAS*, Vienna, Austria, 2012.
34. P. Lang, T. Wojcik, E. Povoden-Karadeniz, A. Falahati, E. Kozeschnik, "Thermo-kinetic prediction of metastable and stable phase precipitation in Al-Zn-Mg series aluminium alloys during non-isothermal DSC analysis.", *J. Alloy Compd.*, 609 (2014) 129-136.
35. F.D. Fischer, J. Svoboda, F. Appel, E. Kozeschnik, "Modeling of excess vacancy annihilation at different types of sinks", *Acta Mater.*, 59 (2011) 3464-3472.
36. A. Falahati, P. Lang, E. Kozeschnik, "Precipitation in Al-alloy 6016—the role of excess vacancies", *Mater. Sci. Forum*, 706-709 (2012) 317-322.